Final Report

Date of Report: *July 31, 2010*

Contract Number: *DTPH56-07-T-000009*

Prepared for: *James Merritt, DOT-PHMSA*

Project Title: In-Situ Hydrogen Analysis in Weldments: Novel NDE for Weld Inspection

Prepared by: Colorado School of Mines and National Institute of Standards and Technology

Contact Information: *David Olson, dolson@mines.edu, Brajendra Mishra, bmishra@mines.edu, Kamalu Koenig, kkoenig@mines.edu*

For project period ending: *July 31, 2010*

ABSTRACT

Linepipe steels are becoming more susceptible to hydrogen damage as the strength of the steel increases. The oil and gas industry are demanding higher strength steels (yield strength of 70 ksi or greater) to be able to operate at higher pressures with larger diameters and smaller wall thickness. Only a few parts per million of hydrogen present in the high strength steel could result in hydrogen damage. A hydrogen tolerance limit has not been determined for the higher strength linepipe steels. The effect of service life makes it even more difficult to predict a single hydrogen content tolerance limit for high strength linepipe steels. It is essential to have a nondestructive means to monitor hydrogen content in high strength linepipe steels and weldments over the life of the linepipe to prevent significant damage or failure.

A nondestructive hydrogen content sensor for field measurements must be able to operate through the linepipe structural coating, which means non-contact and nondestructive technology must be utilized. Low frequency impedance measurements provide an effective non-contact method to determine hydrogen content through a linepipe coating. Low frequency impedance measurements have been correlated to hydrogen content in steel weldments both in the laboratory and in the field. The development of a real-time, nondestructive, non-contact, in-field hydrogen sensor utilizing low frequency impedance is described. Theoretical explanations of LFIM include free electron theory, quantum mechanics, RKKY theory, and a corollary to QED.

TABLE OF CONTENTS

LIST OF FIGURES

LIST OF TABLES

CHAPTER 1 INTRODUCTION

The goal of this project is to develop a nondestructive sensor to assess the hydrogen content in coated linepipe steel weldments. Chapter 2 reviews the role of hydrogen in steel and its effect on electromagnetic and mechanical properties. A survey of studies aimed at monitoring the hydrogen distribution in welds is covered. The fundamental electromagnetic principles behind low frequency impedance measurements are discussed in Chapter 3. Ferromagnetic material property assessment through harmonic analysis of induced voltage and hysteresis parameters is presented here. Chapter 4 presents a brief examination of common hydrogen content determination methods. Chapter 5 outlines the design criteria of a low frequency impedance sensor for coated thick-walled linepipe weldments. The prior research effort here at CSM is presented in Chapter 6. Hydrogen content assessment of a coated steel linepipe in the field is given in Chapter 8. A theoretical treatise on the physics describing the underlying phenomena utilized by low frequency impedance is presented in Chapter 9. A summary of results is given in Chapter 10. Experimental and theoretical conclusions are presented in Chapter 11.

CHAPTER 2 LITERATURE REVIEW OF HYDROGEN IN LINEPIPE STEEL

2.1. Hydrogen Ingress and Transport

The most common source of hydrogen in steel for temperatures below 200 ˚C is the liberation of atomic hydrogen by the iron-water reaction whenever steel surfaces contact aqueous environments [1]. Hydrogen can be introduced into steel during electroplating, pickling or heat treating during steelmaking, during welding fabrication, and during corrosion reactions and cathodic protection of steel linepipes transporting sour crude and other petroleum products [2, 3]. Cathodic steel surfaces during corrosion processes or cathodic protection practices for linepipe steels produce adsorbed hydrogen where it is available to be absorbed into the steel matrix.

2.1.1. Solubility and Trapping of Hydrogen

The solubility of hydrogen in steel is known to increase with increasing H_2 gas pressure at constant temperature. Sieverts' law,

$$x \propto \sqrt{p}\,, \tag{2.1}$$

is obeyed for low concentrations of diatomic molecules dissociating into atomic species such as hydrogen absorption into steel [4]:

$$\frac{1}{2}H_2(g) \rightarrow H_{abs}(ppm)\,. \tag{2.2}$$

Figure 2.1 shows the solubility of hydrogen in iron for different hydrogen gas pressures. Note the increased hydrogen solubility of fcc γ-iron over bcc α and δ-iron depicted in Figure 2.1.

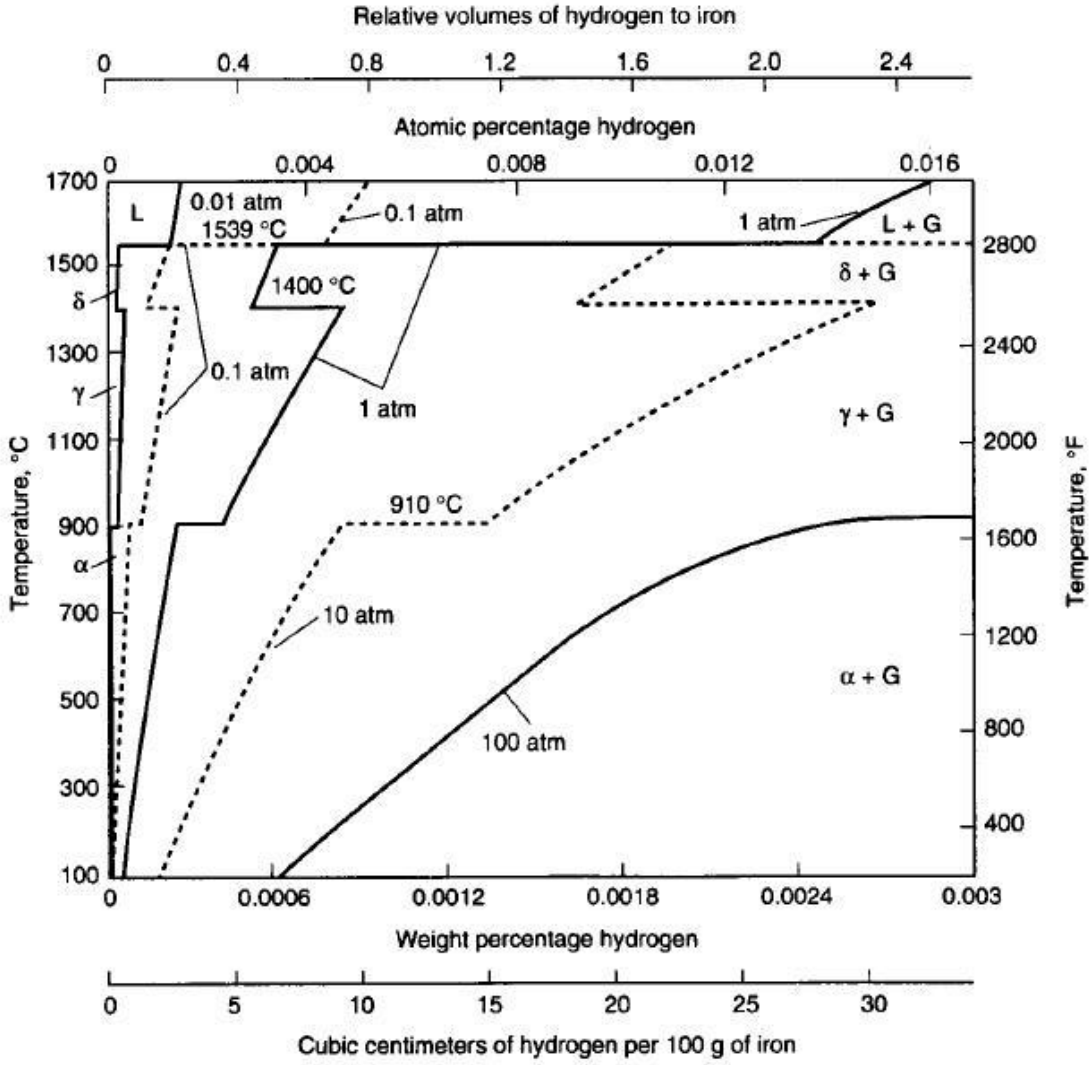

Figure 2.1. Equilibrium diagram for the iron-hydrogen system [1].

The sign of the enthalpy change of solution for metal-hydrogen systems determines the form of hydrogen in solution. Stable metal hydrides form in exothermic systems whereas endothermic systems result in a metal-hydrogen solid solution. The elements to the left of manganese on the periodic table have negative heats of mixing with hydrogen. The elements to the right of manganese on the periodic table have positive heats of mixing. Soluble interstitial hydrogen occupies the tetrahedral site in bcc iron and the octahedral site in fcc iron [5, 6]. Tetrahedral site occupancy of hydrogen in bcc iron is energetically favorable at temperatures below 600 ˚C [7]. Short-range interactions

between hydrogen and different microstructural features such as inclusions, defects, grain boundaries present in steel is defined by the binding energy.

The binding energy is the free energy difference between the interstitial site and the trap site, depicted in Figure 2.2. The traditional benchmark value to classify trap type is 60 $kJ \cdot mol^{-1}$ [8]. According to Pressouyre, hydrogen trapping energies range from 0.1 to 1.0 eV (9.6 to 96.5 $kJ \cdot mol^{-1}$) [9]. Binding energies below this value are classified as reversible while binding above this value are classified as irreversible. Hydrogen interactions with trapping sites effectively increase hydrogen solubility at low temperatures, as illustrate by Figure 2.3 [10].

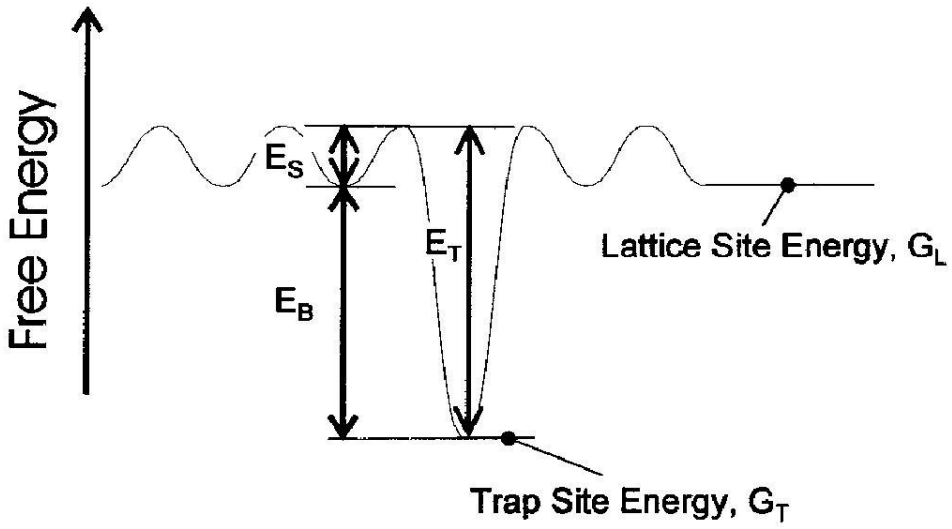

Figure 2.2. Schematic depiction of binding energy [8].

Shirley and Hall have calculated the interaction energies of interstitial hydrogen with interstitial and substitutional impurities in α-iron to determine the hydrogen trapping effectiveness of the impurities. Elastic interactions were attractive for impurities that expanded the lattice. Substitutional impurities created an electronic interaction of the same magnitude as the elastic one and were attractive for substitutional valences less than iron. These calculations were based on hydrogen occupying the tetrahedral site in bcc iron and assuming octahedral occupancy of the impurity atoms carbon and nitrogen [11].

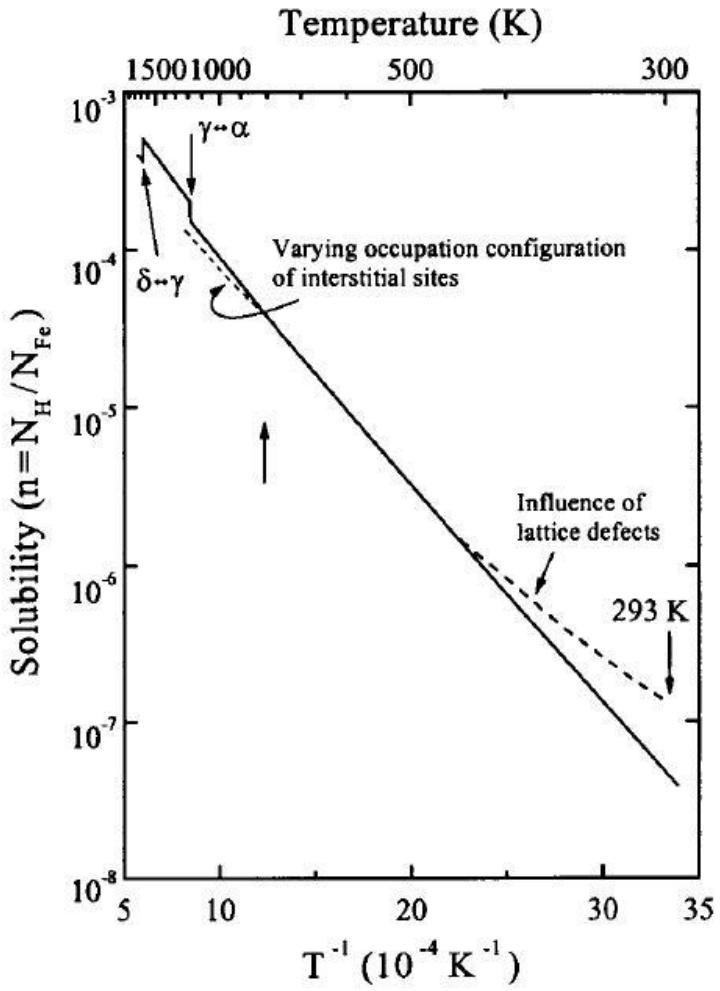

Figure 2.3. Solubility of hydrogen in iron under ambient pressure [10].

Oriani performed a thermodynamic analysis of the anomalous behavior of hydrogen solubility and diffusivity in which he assumed steady state equilibrium between trapped and interstitial lattice sites [12]. He derived an expression for apparent diffusivity,

$$D_a = D_L \frac{dc_L}{dc_T}, \tag{2.3}$$

where D_L is the lattice diffusivity in a defect free bcc iron matrix and c_L and c_T are the concentrations of hydrogen in the lattice interstitial sites and the trapped sites, respectively. Maroef et al. used this expression for apparent diffusivity from Equation 2.3:

$$D_a = \frac{D_L}{1 + c_T^0 \exp(E_B / RT)}, \tag{2.4}$$

where c_T^0 is the concentration of available trap sites in the matrix and E_B is the trap binding energy, which is negative based on the convention outlined in Figure 2.2 [8]. Table 2.1 lists values of the diffusion coefficient for hydrogen in steels for different temperature ranges.

The effect of microstructure on hydrogen trapping in steel is well documented [8, 13, 14]. Retained austenite has been shown to be a strong reversible volume hydrogen trap, much stronger than reversible dislocation traps but weaker than irreversible TiC precipitate traps [15]. Chan identified and compared the trapping sites in pure iron, ferritic-pearlitic and martensitic steels. Table 2.2 lists the ranking of hydrogen occlusivity for a variety of microstructures. Increased carbon content resulted in higher hydrogen trapping for the same Fe-Mn alloys (M4 with (0.40 wt. pct. C) and M8 with (0.76 wt. pct. C) for all microstructures except for martensite with enhanced trapping ability based on high dislocation densities (up to 10^{11} to 10^{12} cm^{-2}). Martensite has the lowest solubility and a high apparent diffusivity for hydrogen, though tempering drastically reduces this effect as seen in Figure 2.4.

Table 2.1. Diffusion coefficient values for hydrogen in microalloyed and low carbon structural steels [16, 17].

Temperature (K)	**Diffusion coefficient ($mm^2 \cdot s^{-1}$)**		
	Minimum	**Maximum**	**Average**
293-473	$8.7615 \times 10^{-9}(T\text{-}273)^{2.2285}$	$0.076\ e^{-9562/RT}$	$0.07465e^{-11072/RT}$
473-1013	$8.996 \times 10^{-9}(T\text{-}273)^{2.2480}$	$8.11 \times 10^{-6}(T\text{-}273)^{1.528}$	$0.11e^{-12437/RT}$
1013-1723	$0.6736e^{-45086/RT}$	$1.0691e^{-41624/RT}$	$0.8753e^{-46396/RT}$
1723-1823	$28.7905e^{-93534/RT}$	$0.437e^{-17273/RT}$	$1.2104e^{-37785/RT}$

1823-2273	$0.246e^{-15450/RT}$	$0.437e^{-17273/RT}$	$1.1578e^{-37007/RT}$
** R = 8.315 J·K·mol^{-1}*			

Table 2.2. Hydrogen content of different microstructures of two Fe-Mn-C alloys M4 (0.40 wt. pct. C) and M8 (0.76 wt. pct. C) compared to commercial AISI 4130 steel for two different charging times (in hours) [13].

Microstructure	**HYDROGEN CONTENT (c.c./100 g)**					
	M4		**M8**		**AISI 4130**	
	8	16	8	16	8	16
Ferrite/Pearlite	1.84	1.17	2.83	4.80	1.21	2.02
Upper Bainite	1.99	2.44	4.36	5.48	2.89	3.29
Lower Bainite	2.56	2.39	5.31	7.41	3.17	4.10
Martensite	9.71	11.02	6.25	8.50	7.14	9.43
Tempered Martensite	3.00	2.71	3.62	5.27	5.65	5.72

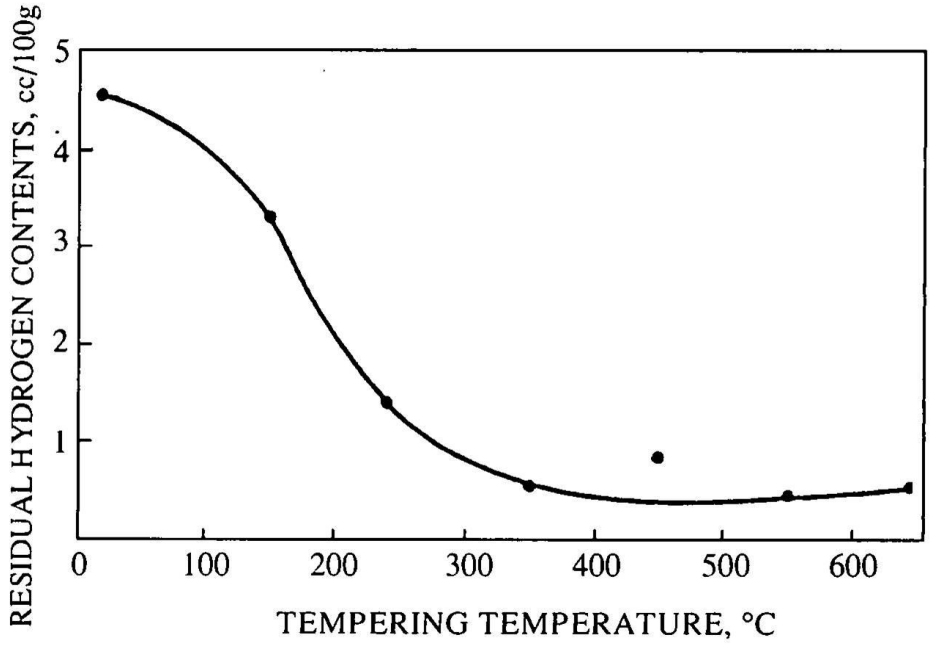

Figure 2.4. Tempering effect on residual hydrogen content in tempered martensitic structure [13].

Park et. al compared the hydrogen trapping efficiency of different secondary phases in primarily ferrite API grade X65 linepipe steel. Trapping efficiency, inversely measured by the apparent diffusivity, increased in order from pearlite, bainite, to acicular ferrite second phases [14].

2.1.2. Hydrogen Permeation Studies

The most common hydrogen permeation measurement method utilizes the Devanathan-Stachurski permeation cell. In pure iron at 300K and partial pressure of hydrogen gas of one atm, hydrogen solubility is limited to 0.01 to 0.1 ppm with enhanced diffusivity of about 8 x 10^{-9} $m^2 \cdot s^{-1}$. This sensitive electrochemical technique employed for hydrogen permeation measurements can detect hydrogen fluxes at these low level concentrations [18]. Hydrogen permeability is defined as:

$$\Phi = \Phi_0 \exp(\frac{-E_p}{RT}), \tag{2.5}$$

and is essentially the product of diffusivity and solubility,

$$\Phi_0 = D_0 S_0, \tag{2.6}$$

where

$$E_p = E_s + E_m \tag{2.7}$$

is the activation energy for permeation based on the energy of solution (E_s) and the energy of migration (E_m) [18]. Values of hydrogen permeability in iron are listed in Table 2.3. Diffusivity and energy of migration values for hydrogen in iron are listed in Table 2.4.

Table 2.3. Permeability pre-exponentials (Φ_0) and activation energies (E_p) of hydrogen in iron [18].

Reference	Temperature (K)	Φ_0 $\left(x10^{17} \frac{H_{atom}}{cm \cdot \sec \cdot atm^{0.5}} \right)$	$E_p \left(\frac{cal}{mol} \right)$
[19]	633-833	1.6 ± 0.3	8450 ± 100
[20]	273-333	2.6	8500 ± 600
[21]	281-346	$1.9^{+12.2}_{-1.65}$	8380 ± 610
[22]	322-779	$2.53^{+7.97}_{-1.62}$	8520 ± 670
[23]	340-770	1.0	8200

Table 2.4. Lattice diffusion coefficients (D_0) and activation energies for migration (E_m) for hydrogen in iron [18].

Reference	Temperature (K)	$D_0 \left(x10^{-3} \frac{cm^2}{\sec} \right)$	$E_m \left(\frac{cal}{mol} \right)$
[22]	322-799	$1.6^{+0.94}_{-0.59}$	1690 ± 30
[23]	327-770	2.33	1600

Dey et al. surveyed X65 linepipe steel for sub-surface hydrogen concentration under freely corroding conditions; hydrogen was generated in the cathodic reaction. Almost all hydrogen permeation studies simulate cathodic hydrogen charging as a result of cathodic protection. Dey et al. chose to evaluate freely corroding conditions, introducing chemical reactions that consume or generate hydrogen while creating diffusion barrier corrosion products that alter the hydrogen ab/adsorption reaction, resulting in maximum peaks of sub-surface hydrogen, as shown in Figure 2.5.

Table 2.5 lists the values of hydrogen permeability for different steel microstructures.

Table 2.5. Hydrogen permeation rates through different steel microstructures [3].

Steel (wt. pct. C)	Heat Treatment	Microstructure	Permeation

			rate (cm^3/h)
0.06	Normalized	Primarily Ferrite	0.44
0.59	850 °C, normalized	Ferrite plus lamellar pearlite	0.22
0.59	850 °C, water quench	Martensite	0.14

Ichitani and Kanno [24] correlated high sensitivity hydrogen microprint technique (HMT) results with permeation measurements to study the diffusion paths of hydrogen in low carbon and hypoeutectoid steels. HMT utilizes hydrogen reduction reaction of silver bromide to visually detect hydrogen exit sites by the reduced silver particles remaining.

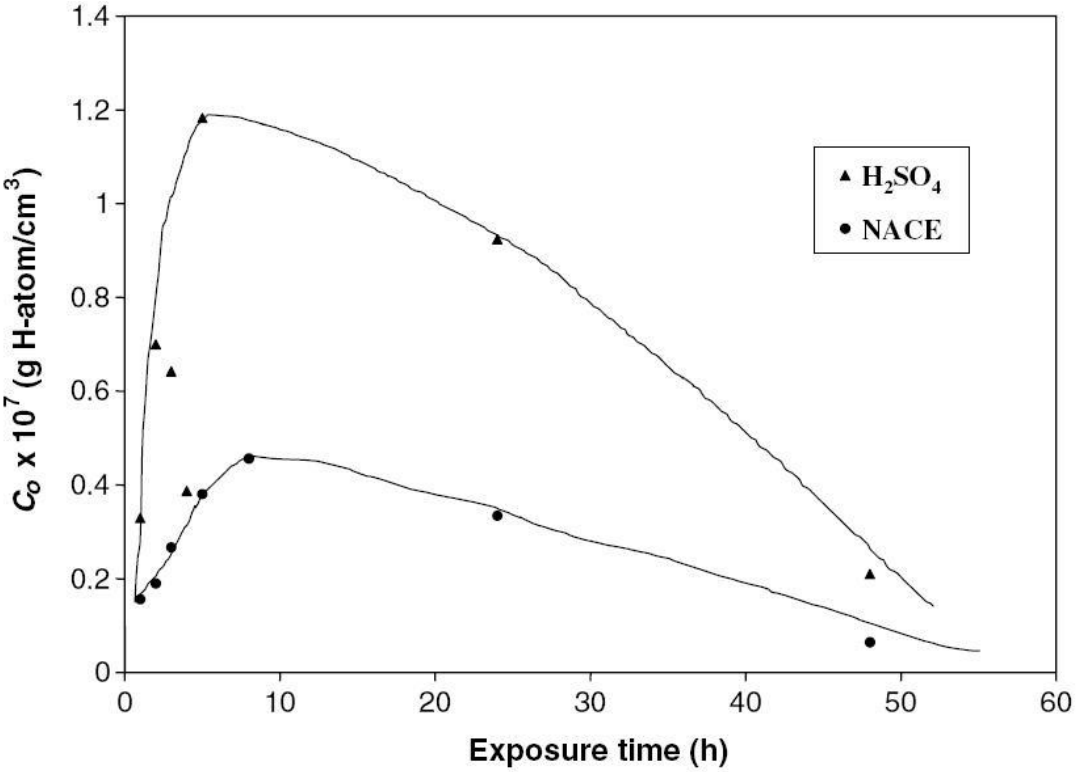

Figure 2.5. Sub-surface hydrogen concentration variation with exposure period [2].

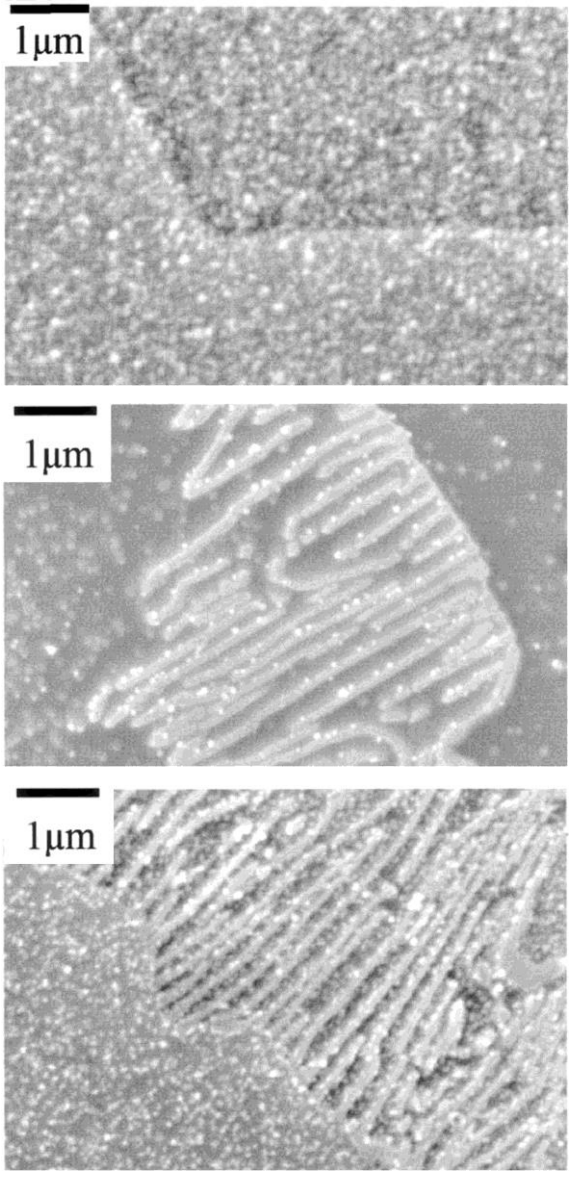

Figure 2.6. High sensitive HMT results for: (a) twenty minute charging condition of extremely low carbon steel (b) five and (c) twenty minute charging of hypo-eutectoid steel [24].

The main diffusion path in extremely low carbon steel (0.002 wt. pct. C) was observed to be through the lattice in ferrite grains after steady state charging of forty minutes. The uniform distribution of silver particles on the ferrite grains of the low carbon steel, seen in Figure 2.6a, is a proof that the ferrite grain boundaries do not act as an accelerated diffusion path. The initial un-steady state charging of the hypoeutectoid steel resulted in silver particles primarily along the ferrite-cementite interfaces in the pearlite with few particles on the proeutectoid ferrite grains, shown in Figure 2.6b. These results, obtained after charging for five minutes, confirmed the findings of Luu and Wu with conventional HMT that the preferential diffusion pathway in pearlitic steels was along the cementite/ferrite interface [25]. The uniform distribution of silver particles in the proeutectoid ferrite grains and the ferrite in pearlite, shown in Figure 2.6c of the steady state charging results for the hypoeutectoid steel, demonstrate the preferred steady-state diffusion path in hypoeutectoid steels is within the ferrite grain. Low carbon ferritic steel was observed to have a slightly higher permeation rate and nearly twice the diffusivity of hypoeutectoid steel [24].

2.1.3. Magnetocorrosion

Abrupt changes in the magnetic field in hydrogen-charged ferromagnetic materials cause a redistribution of hydrogen atoms; hydrogen atoms will diffuse to more energetically favorable sites in the magnetic domain structure. Sánchez et al. showed that an applied magnetic field enhanced hydrogen pickup of electrolytically charged linepipe steels of various grades [26]. Jackson derived the thermodynamic equations governing the enhanced hydrogen pickup in the presence of an applied magnetic field known as magnetocorrosion [27].

The effect of magnetization introduces an internal work term given by:

$$dw_{\text{int}} = \Delta MB + dw_{ms} + dw_{ss}, \tag{2.8}$$

where ΔMB is the contribution of the changed electron spin configuration, dw_{ms} is the magnetostriction strain internal work term and dw_{ss} is the term for solute-strain due to hydrogen interstitial atoms in the lattice. Helmholtz free energy:

$$dA = dG + dw_{\text{int}}, \tag{2.9}$$

is Gibbs free energy plus the internal work given by Eqn. 2.8. Sanchez and Jackson assume freely corroding conditions in a magnetically charged working linepipe, yielding:

$$dA = -nF\varepsilon + \Delta G^0 - RT \ln \frac{[H^+]}{[H]} + \Delta MB + dw_{ms} + dw_{ss} \tag{2.10}$$

for the Helmholtz free energy. The solubility of hydrogen at equilibrium ($dA = 0$) is:

$$[H] = [H_{B=0}] \exp\left[\frac{-\Delta MB}{RT}\right] \exp\left[\frac{-dw_{ms}}{RT}\right] \exp\left[\frac{-dw_{ss}}{RT}\right], \tag{2.11}$$

where

$$[H_{B=0}] = \exp\left[\frac{-nF\varepsilon}{RT}\right] \exp[2.3pH] \exp\left[\frac{-\Delta G^0}{RT}\right] \tag{2.12}$$

is the hydrogen concentration in the unmagnetized steel [26, 27].

2.2. Hydrogen-Induced Lattice Strain

In bcc iron, the tetragonally symmetric tetrahedral sites (½, ¼, 0) are expected to have strain fields of the form [7]

$$\in_{ij} = \begin{pmatrix} \in_{11} & 0 & 0 \\ 0 & \in_{22} & 0 \\ 0 & 0 & \in_{22} \end{pmatrix}. \tag{2.13}$$

Interstitial site occupancy produces a displacement strain field which is a component of the long-range displacement fields of the periodic lattice.

Tetelman et al. reported x-ray diffraction results of cathodically charged vacuum-melted pure iron similar to the peaks produced for 5 pct. tensile strained pure iron [28]. Hume-Rothery states that this evidence of hydrogen plastically deforming iron casts doubt on the interstitial occupancy of soluble hydrogen in iron, as there was no change in the lattice parameter of iron due to hydrogen charging [29]. Glowacka reported increased dislocation density following pronounced grain refinement in the ferritic phase and increased stacking fault density in the austenitic phase of a cathodically charged duplex stainless steel [30].

According to Peisl, dissolved hydrogen expands the lattice of the host metal in all known metal-hydrogen systems. This lattice strain due to interstitial hydrogen is a result

of typical relative volume expansions (for H/M = 1) on the order of 20 pct [31]. The additional volume for one interstitial, Δv, can be determined by a size factor, λ, as:

$$\Delta v = 3\lambda , \tag{2.14}$$

where

$$\lambda = \Delta a \cdot a^{-1} \cdot \Delta c^{-1}, \tag{2.15}$$

where a is the lattice parameter and c is the interstitial concentration (H/M). For a cubic crystal of with randomly distributed interstitial atoms resulting in relatively small volume changes, $\frac{\Delta v}{v}$, measurement of changes in one dimension:

$$\frac{\Delta a}{a} = \frac{c}{3}(\frac{\Delta v}{\Omega}), \tag{2.16}$$

is sufficient to approximate volume changes. The mean metal atomic volume is given by Ω [31]. Fukai reported one hundred forty-two and three hundred sixteen percent increases in the lattice parameter for hydrogen occupying the tetrahedral and octahedral interstitial sites in bcc metal lattices [4].

2.3. Hydrogen-Induced Change in Electronic Properties of Steel

Electronic property behaviors are modified with hydrogen alloying of metal systems. Electronic calculations have shown that the hydrogen ion *1s*-like orbitals become strongly hybridized with the surrounding metal atom *d*-orbitals to create bonding states. Gavriljuk has concluded that the density of conduction electrons increases around the octahedral hydrogen interstitial sites in fcc iron, substantiated by Figure 2.7. It is the flexibility of the metal atom lattice electronic states that account for the interstitial transiency of hydrogen atoms [4].

2.3.1. Electron Effective Mass

The additional lattice strain introduced by interstitial occupancy modifies the electronic band structure of the host metal producing a different interaction to the nearly-free conduction electron wave function. Adjustments in the Fermi energy level result in a change in the effective mass of the electron. The effective mass can be described as:

$$m_e = \hbar^2 (\frac{d^2 E}{dk^2})^{-1}, \tag{2.17}$$

where k is the wave vector. The effective mass, m_e, describes the shape of the s, p, and d bands that are in contact with the Fermi energy level. The shape of the bands at the contact position offers a sensitive indication of changes in alloy composition, phase content, and lattice strain.

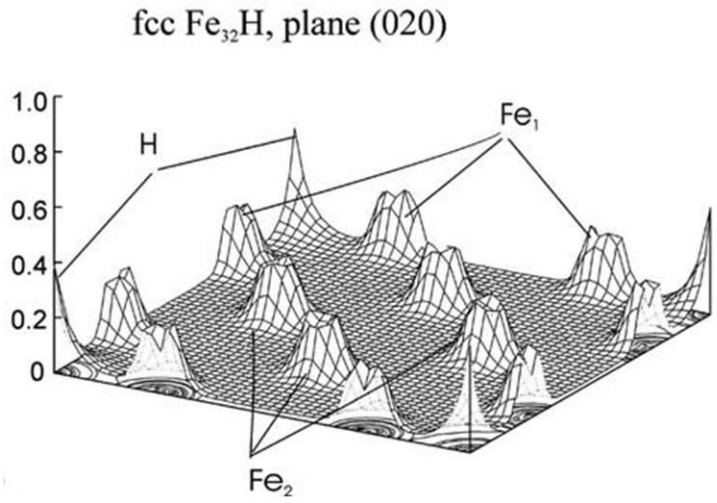

Figure 2.7. DFT calculation of electron densities in γ-iron at 0K with 3.03 at. pct. octahedral interstitial hydrogen [32].

To understand the role of the effective mass of the electron in interpreting the electronic interactions with the lattice consider a free electron wave function in a lattice. Figure 2.8 is an illustration of the free electron wave function, described by the dashed line, with local electron interactions of the potentials associated with the lattice atoms.

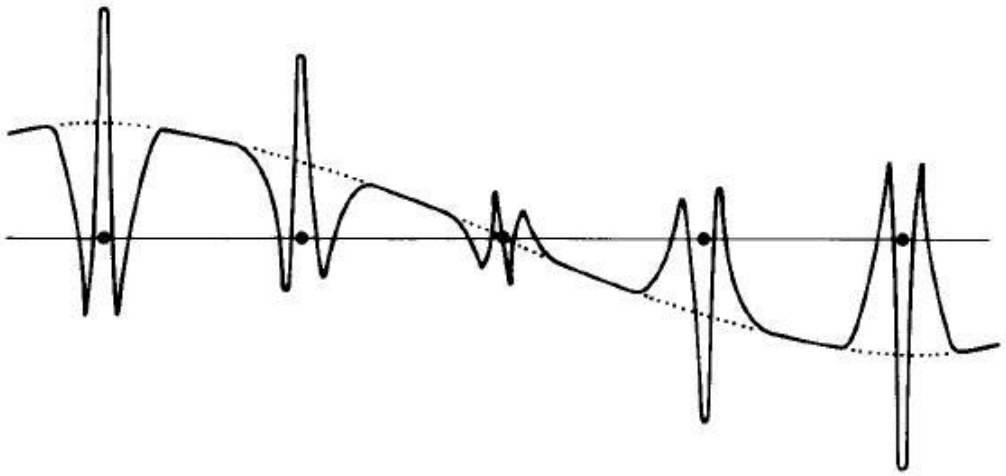

Figure 2.8. The (augmented plane wave) wave function produced by a combination of atomic states with a free electron wave function between the ion cores [33].

If a lattice atom is a solute atom or is situated in a strain field, the localized potential will be altered and will offer a different interaction to the nearly-free conduction electron wave function. In the free electron model, the potential is zero, thus the energy of the electron is expressed as:

$$E = \frac{\hbar^2 k^2}{2m}, \tag{2.18}$$

where m is the electron mass. There is a nonzero potential energy experienced by the conduction electron in the vicinity of the lattice atom. Incorporating the localized lattice potential energy into the free electron mass results in the effective mass of the electron, m_e, in the following expression for the total energy:

$$E = \frac{\hbar^2 k^2}{2m_e}. \tag{2.19}$$

This formulation allows for the free electron to be used to derive the electron properties of an alloy. The effective mass is a valuable parameter in the electronic property assessment of microstructure and alloy stability.

Switendick compared two measurements of density of electronic states, *N(E)*, the electronic specific heat at low temperatures and magnetic susceptibility. Hydrogen

additions to palladium lowered the magnetic susceptibility and caused a decrease in the electronic specific heat by greater than a factor of twelve [34].

Gavriljuk concluded from *ab initio* calculations that carbon, nitrogen, and hydrogen interstitials have different effects on electronic structures in steels. Carbon causes a decrease in *N(E)* at the Fermi energy level in fcc iron while hydrogen and nitrogen result in an increase as presented in Figure 2.9 [32].

The proton model of the metal-hydrogen bond depicts the hydrogen atom losing its electron to the host metal electronic states. A well experimentally supported system for the proton model is PdH_x. The strongly paramagnetic pure palladium has its *d*-band holes filled by alloying hydrogen, resulting in the weakly diamagnetic PdH_x. The screened proton model developed by Friedel and others describes the electrostatic Coulombic potential of a proton resulting from donation of the hydrogen electron to the unfilled states at the Fermi energy surface being screened as these metal states relax. Exothermic hydride formation results from the electrostatic interaction between the screening cloud and the proton [35].

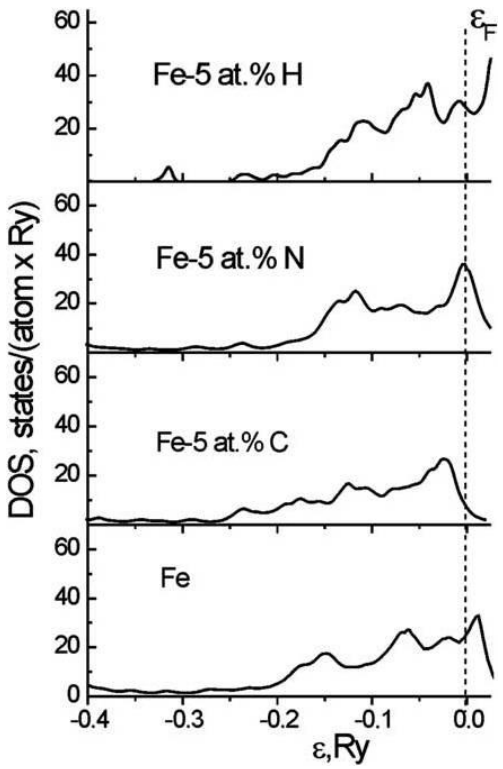

Figure 2.9. Effect of hydrogen, nitrogen, and carbon (all 5 at. pct.) on the density of electronic states in γ-iron at 0K [32].

2.3.2. Resistivity Changes

Electrical resistivity changes due to interstitial hydrogen are well-documented [36, 37, 38]. Watanabe observed a linear dependence of electrical resistivity to hydrogen and deuterium concentration in niobium and α-palladium for temperatures over 120 °C, seen in Figure 2.10. These experimental results confirmed the isotope independence of the two electron-impurity scattering mechanisms that caused resistivity changes with hydrogen concentration: scattering off the lattice distortion and scattering off the impurity potential [37]. Resistivity recovery, shown in Figure 2.11, is the decrease in resistivity of hydrogen-charged metal upon annealing. Two experiments on pure iron have demonstrated similar results [36, 38].

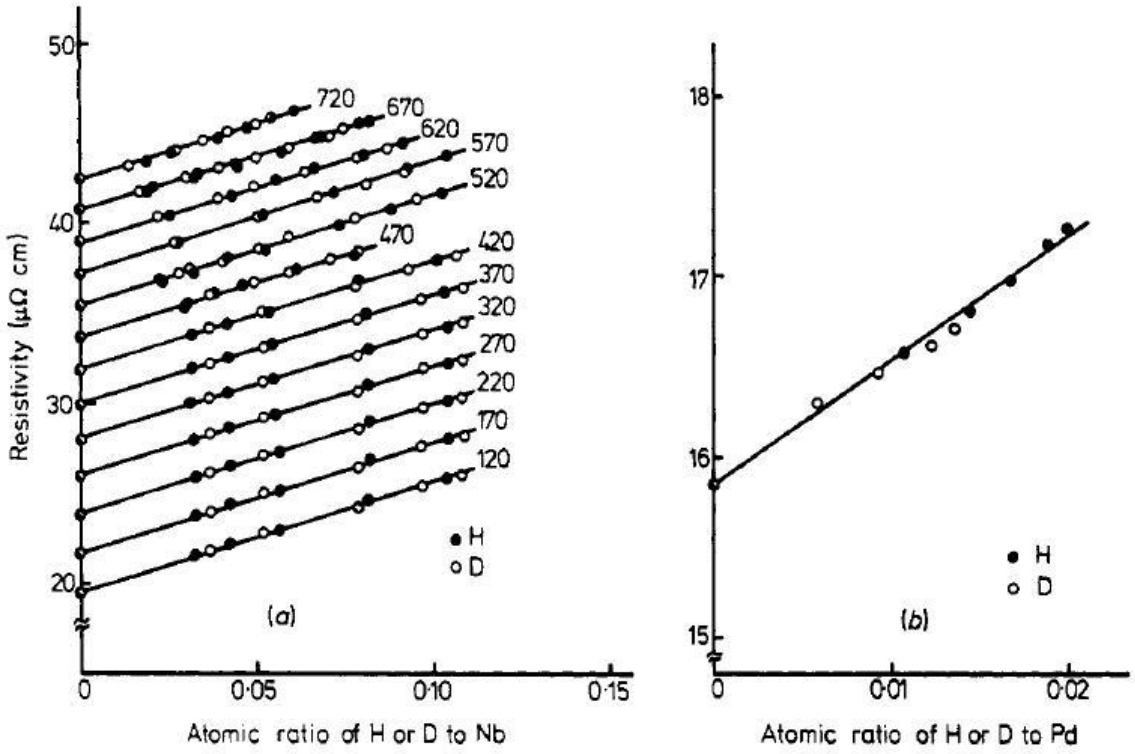

(a) **(b)**

Figure 2.10. Concentration dependence of the resistivity due to hydrogen and deuterium in (a) niobium at various temperatures and (b) palladium at 170 °C [37].

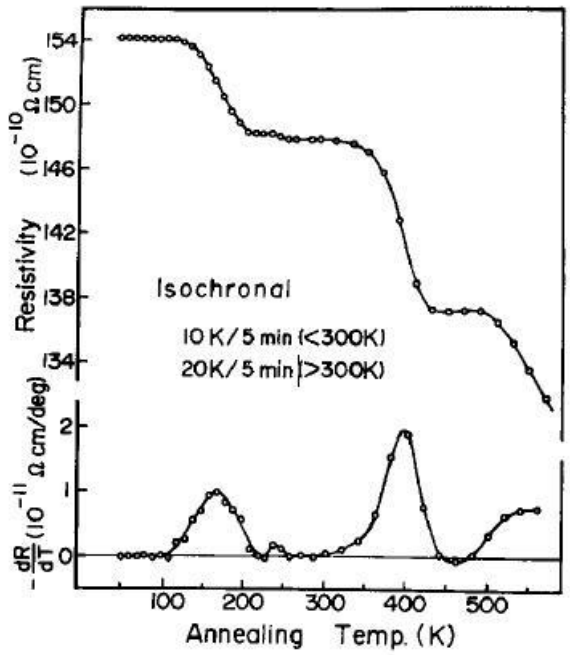

Figure 2.11**.** Resistivity recovery of pure iron during isochronal annealing up to 560K [38].

2.4. Hydrogen Distribution in Welds

Hydrogen pickup during welding procedures can be due to high-humidity atmosphere, moisture on stick electrodes, moisture or grease on the welding surface, or shielding gas impurities [3].

This section presents theoretical models developed and experimental data gathered for hydrogen distribution in welds based on the IIW/AWS diffusible hydrogen determination standards by Gedeon and Eagar, Mundra et al., and Andersson. Gedeon and Eagar have proposed a complete description alternative to the one-step Sieverts' law description of hydrogen absorption at low temperatures to assess hydrogen absorption during welding. Welding arc dissociation of diatomic hydrogen gas is followed by the absorption of both diatomic and monatomic hydrogen on the weld pool surface with maximum temperature of 2500 ˚C, limited by the evaporative cooling of iron vapors. The correction of the one-step hydrogen absorption process is made with consideration of the effects on hydrogen absorption of weld pool surface temperature and solute rejection during weld solidification. Gedeon and Eagar utilize the analysis of Terasaki to convert diffusible hydrogen detected to the value of initially absorbed hydrogen [39, 40]. Davis

used a combination of laser ablation and mass spectrometry to create the semi-quantitative hydrogen distribution profile [41].

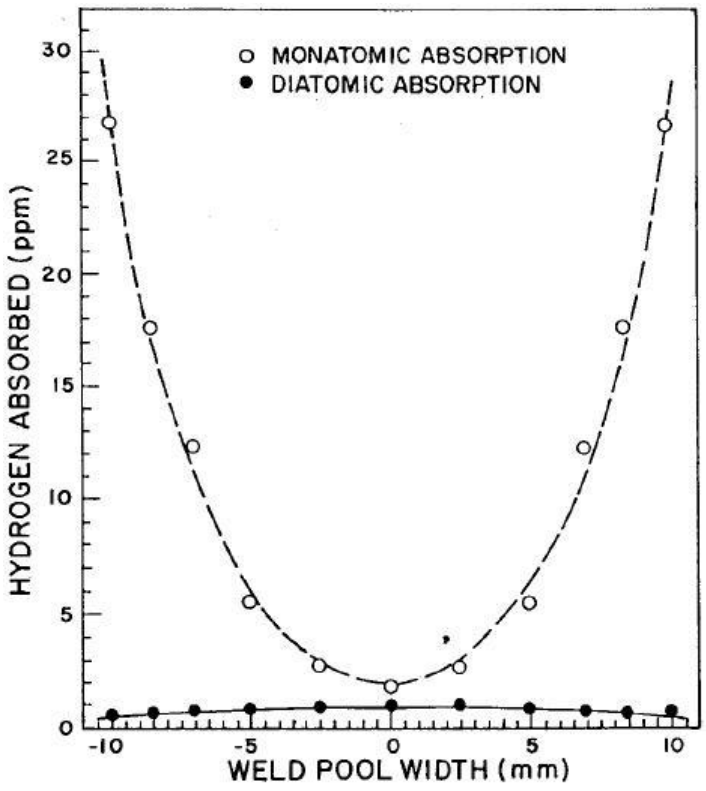

Figure 2.12. Theoretical hydrogen absorption due to monatomic and diatomic hydrogen as a function of weld pool location [39].

The absorption of monatomic hydrogen, found to decrease with weld pool surface temperature, results in higher monatomic absorption towards the edge of the weld bead, as illustrated by Figure 2.12. Liquid iron solubility of monatomic hydrogen can be described as chemical while diatomic hydrogen may be described as physical. This partitioned absorption is temporary as the absorbed hydrogen is thoroughly mixed due to convective flow. Desorption might take place at hotter spots in the weld pool, though most is absorbed at the advancing solidification front of the trailing edge of the weld. This theory predicts greater hydrogen absorbed for gas-metal-arc welds made in the electrode positive rather than the electrode negative scheme [39].

Once hydrogen is absorbed and transported through the weld pool by diffusion and convection, it diffuses into the interior of the solid metal. Mundra et al. predicted the hydrogen concentration in a GMA weld AWS A4.3-93 specimen of low alloy steel [13]. The presence of monatomic and ionic hydrogen species in the welding arc plasma result in hydrogen concentrations greater than predicted by Sieverts' law.

The surface concentration of diatomic hydrogen (in ppm),

$$(C_H)_d = (p_{H_2})_{T_d}^{1/2} \exp(\frac{-\Delta G_1^0}{RT_s}), \tag{2.20}$$

is defined for

$$\frac{1}{2} H_2(g) = H, \tag{2.21}$$

where $(p_{H_2})_{T_d}$ is the partial pressure of diatomic hydrogen at the disassociation temperature, T_d, and ΔG_1^0 is the standard free energy and T_s is the weld pool surface temperature. The surface concentration of monatomic hydrogen (in ppm),

$$(C_H)_m = (p_H)_{T_d} \exp(\frac{-\Delta G_2^0}{RT_s}), \tag{2.22}$$

is defined for

$$H(g) = H, \tag{2.23}$$

where $(p_H)_{T_d}$ is the partial pressure of monatomic hydrogen at T_d. p_H and p_{H_2} are related by

$$p_H = (p_{H_2})^{1/2} \exp(\frac{-\Delta G_3^0}{RT_d}), \tag{2.24}$$

for

$$\frac{1}{2} H_2(g) = H(g). \tag{2.25}$$

Figure 2.13 shows the convection effect within the molten weld pool and the influx of monatomic hydrogen with the plasma (spots 47 and 50) [13]. The theoretical values calculated by Mundra et al. for the amount of hydrogen deposited in the weld metal are close to the experimentally determined ones, listed in Table 2.6.

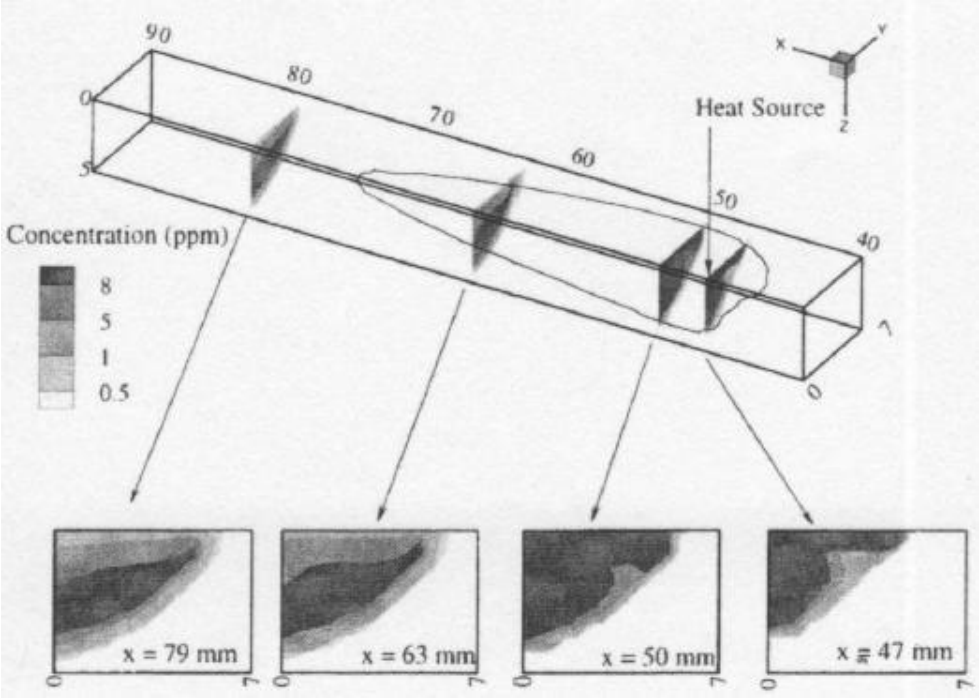

Figure 2.13. Calculated hydrogen concentration at different planes in x-direction for a weld travel speed of 12.7 mm·s^{-1} [13].

Table 2.6. Comparison of experimental results for hydrogen content of three specimens [Adapted from 13]

Weld Travel Speed (mm s^{-1})	Hydrogen Concentration (mL/100 g)			
	1st 40 mm specimen		2nd 40 mm specimen	
	Experimental	Calculated	Experimental	Calculated
5.2	6.67	8.33	8.75	10.00
12.7	16.25	14.58	19.17	18.33
23.2	18.33	18.75	28.33	22.92

Andersson developed an analytical model, examining the effects of stress, thermotransport, trapping, and plastic strain, for hydrogen distribution in a bead-on-plate weld. Hydrogen diffusion in the presence of reversible and irreversible traps was numerically determined for hydrogen behavior anomalous to Fick's second law during the cooling of the weld below 200 °C. Andersson concluded that the IIW diffusible

hydrogen determination procedure copper block welding fixture resulted in hydrostatic stresses and residual plastic straining (maximum effect in the base metal) with little influence on hydrogen distribution, shown in Figure 2.15, determined through finite element calculations. The high hydrogen content near the fusion line presented in Figure 2.14 is verified by a laser beam mass spectroscopy measurement shown in Figure 2.15.

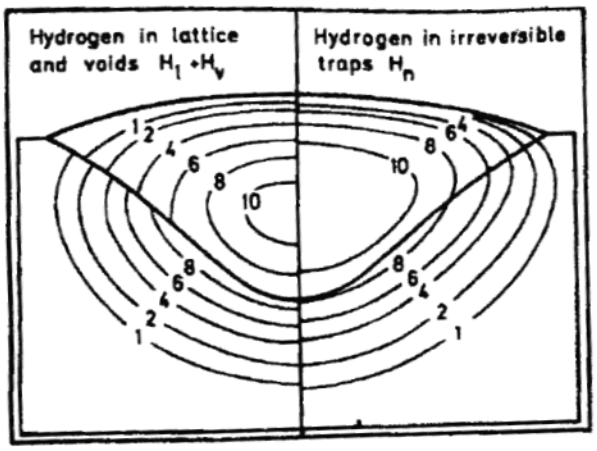

Figure 2.14. Calculated distribution after 350 s of (left) hydrogen in voids and lattice and (right) residual hydrogen. Concentration contours in ppm [42].

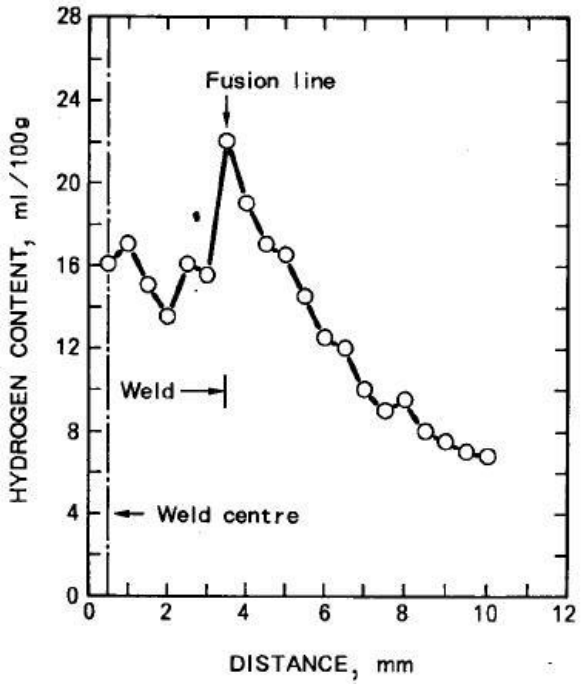

Figure 2.15. Microscopic distribution of hydrogen in a weld measured by laser beam mass spectroscopy [43, 44].

2.5. Hydrogen Charging of Steel

The two forms of hydrogen charging in steel are gaseous and electrochemical cathodic charging. A critical step in gaseous hydrogen charging of steel is the removal of the oxide layer as surface oxides have been shown to decrease hydrogen permeation by three to four orders of magnitude below that in ferritic steel [6, 45]. It is common practice to activate bulk specimens for hydrogen charging by coating the surface with a layer of palladium [5]. The diffusion coefficient of hydrogen at 294K in well-annealed palladium is approximately $7x10^{-6}$ $cm^2 \cdot s^{-1}$ [46]. Native oxides must be removed from the surface of the specimen prior to coating with palladium. Typical charging temperatures (523 to 673K) and gaseous hydrogen pressures (6.9 to 13.8 MPa) ensure charging in the FeH α-phase, as seen from Figure 2.16.

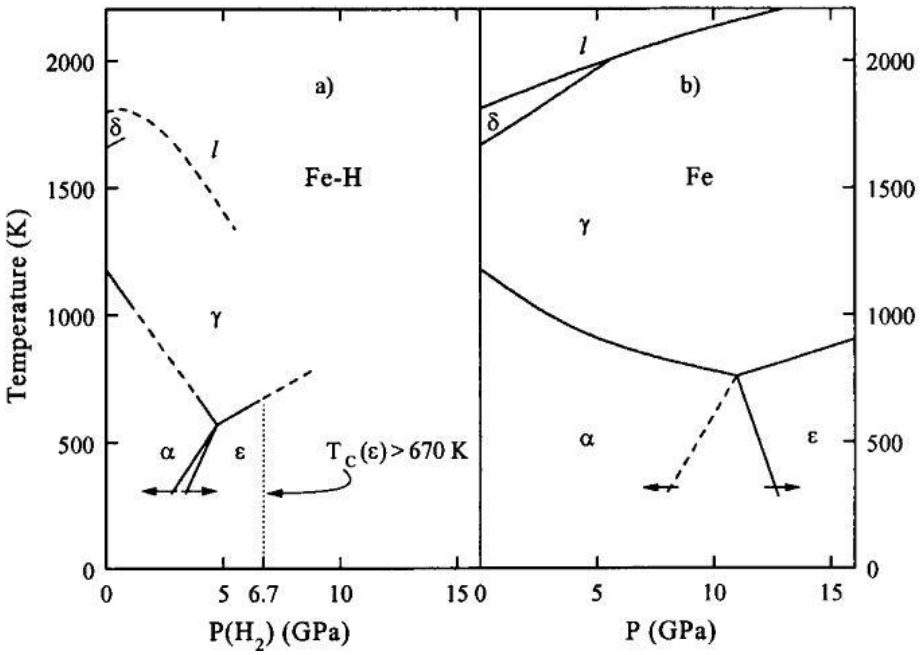

Figure 2.16. a) the $P(H_2)$ – T diagram of Fe-H; b) P-T diagram of iron [9].

Hydrogen permeation measurements (Section 2.1.2) are usually performed with a Devanthan-Stachursky cell utilizing electrochemical hydrogen charging as specified by ASTM Standard G148 [47] or NACE Standard TM0177-2005 [48].

CHAPTER 3 ELECTROMAGNETIC HYDROGEN SENSING

The non-contact electromagnetic sensor developed in this research project utilizes the previously developed concept of low frequency impedance measurements reviewed in Chapter 6. This chapter begins with an explanation of the electromagnetic principles underlying this NDE technique. It is critical to understand the electromagnetic role of hydrogen in steel throughout the development of an electromagnetic technique to assess hydrogen content in steel.

3.1. Low Frequency Impedance Measurements

Low frequency impedance measurements are performed by monitoring the impedance changes of an absolute coil as a low frequency alternating current is passed through. This coil induces a primary magnetic flux that couples with the material being inspected, creating a magnetic circuit. The magnitude of this primary flux is given by:

$$\phi_p(t) = \int B_{coil}(t) \cdot \vec{n} da, \tag{3.1}$$

where $B_{coil}(t)$ is the oscillating magnetic flux density induced by the coil given by:

$$B_{coil}(t) = \mu_{core} N I(t), \tag{3.2}$$

where μ_{core} is the magnetic permeability of the core material of the coil, N is the number of turns of the wire comprising the coil, and $I(t)$ is the amplitude of the applied alternating current. The oscillating nature of the flux induces eddy currents in the sample beneath the coil. The eddy currents produce a secondary flux, which, in accordance with Lenz's law, opposes the primary flux that generated the eddy currents. An equilibrium flux, ϕ_E, is the difference between the primary and secondary fluxes. The coil voltage is a function of this equilibrium flux and is given by:

$$V_{coil}(t) = -N \frac{d\phi_E}{dt} \tag{3.3}$$

The eddy current interaction with the material being inspected will influence the secondary flux, which in turn influences the equilibrium flux and the coil voltage.

Therefore, the coil voltage reflects the total voltage for the entire magnetic circuit. The general form of Ohm's law is given by:

$$V(t) = I(t)Z \tag{3.4}$$

The total impedance *Z*, given by Equation 3.5, is a combination of the coil resistance, *R*, and the frequency-dependent reactance of the coil, *X*.

$$Z = \sqrt{R^2 + X^2} \tag{3.5}$$

At low frequencies, the reactance term is negligible and impedance is approximated by resistance. The resistance of the magnetic circuit is due to the resistance of the conducting wire of the coil and the eddy current interactions with the inspected material. The eddy current density, which determines the strength of the interaction with the inspected material, is determined by the strength of the induced magnetic field in the material. The ratio of the induced magnetic flux density at some depth B_d, with the magnetic flux density induced at the surface of the inspected material, B_0, is given by:

$$\frac{B_d}{B_0} = \exp\left(-\frac{d}{\delta}\right)\sin\left(\omega t - \frac{d}{\delta}\right), \tag{3.6}$$

where the standard depth of penetration, δ, is the scaling factor for this equation. It is equal to the depth at which the induced flux density has decayed to approximately thirty-seven percent of the surface value. The standard depth of penetration (in mm) is given by:

$$\delta_{mm} = \frac{50}{\sqrt{f\mu_r\sigma}}, \tag{3.7}$$

where *f* is the frequency of the applied alternating current in Hertz, and σ and μ_r are the conductivity and relative magnetic permeability of the inspected material. A significant advantage of the low frequency impedance technique is that it can be performed at a coil liftoff distance and through structural coatings.

Variability in low frequency impedance measurements exists because resistivity is a function of the conductivity of the material, the depth of the measurement, and the alloy content. The conductivity, based on the free electron model, is a function of the electronic effective mass, the electron concentration, and the dominating scattering mechanisms, which is altered by such factors as inclusions, microstructure, temperature, and strain. Each of these variables must be separated out to obtain a hydrogen content

measurement using low frequency impedance. All of the controllable parameters are determined to optimally detect the desired material parameter.

Typical eddy current measurements are at much higher frequencies in the kilohertz range and beyond. Khan et al. used an absolute eddy current probe to differentiate between pearlite percentages in low (0.1 wt. pct. C) to high (0.8 wt. pct. C) plain carbon steels [49]. Nestelroth and Davis have devised a rotating permanent magnet source and axial and radial Hall sensors for the eddy current inspection of a linepipe from the inside as shown in Figure 3.1. The eddy currents produced by the rotating magnets differentiate anomalies and wall thickness variations within the linepipe [50].

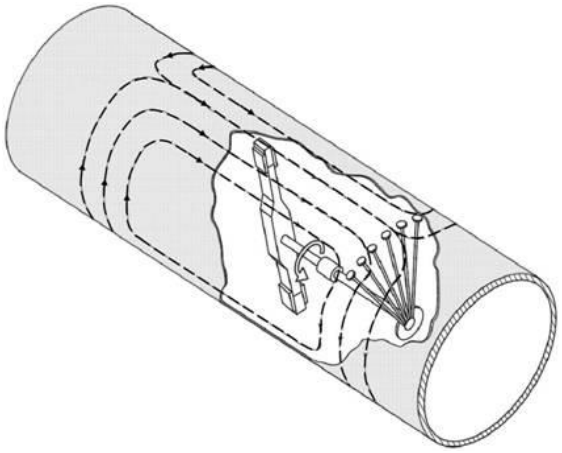

Figure 3.1. Illustration of the rotating permanent magnet and sensor locations [50].

3.2. Ferromagnetic Magnetization

Unlike the electric dipoles that exist between unlike charges, according to the Ampère model, a magnetic dipole is a tiny current loop which produces a magnetic dipole moment, shown in Figure 3.2. Weber first suggested that a ferromagnetic material such as steel has atomic magnetic dipole moments that are randomly oriented in the demagnetized state that become aligned in the presence of an external magnetic field [51].

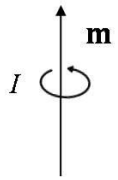

Figure 3.2. Magnetic dipole current loop (*I*) resulting in a magnetic dipole moment (**m**).

Only unpaired electrons from partially filled energy bands can create magnetic moments due to spin imbalances. Ferromagnetic materials retain permanent magnetic dipole moments which contribute to the remanent magnetization in the absence of an applied field.

3.2.1. Magnetic Domains

The direction of magnetization, in the absence of an external field, is affected by lattice strain and crystal structure. In single crystal iron, the easy, medium and hard directions for magnetization are the <100>, <110>, and <111> directions, respectively, as can be seen in Figure 3.3, comparing iron and nickel. Magnetization is easier in the direction of rolling for linepipe steels due to the ease of alignment of magnetic domains in the same direction [52, 53].

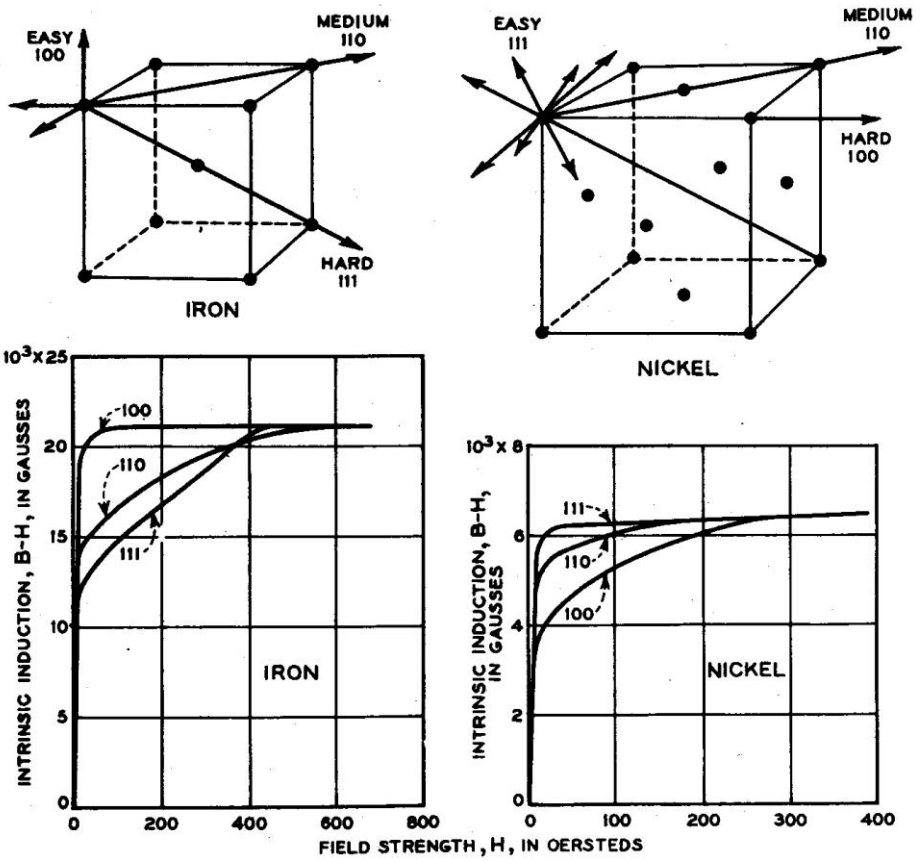

Figure 3.3. Magnetization directions for single crystal iron and nickel [54].

Ferromagnetic magnetization occurs by domain wall displacement. Magnetic domains are one of two classes: 90° walls that separate domains whose magnetizations make a 90° angle and 180° walls that separate oppositely magnetized domains. In the case of iron, with the <100> family of easy magnetization axes, a 180° wall would separate domains with magnetization directions of [100] and $[\bar{1}00]$ while a 90° wall would separate domains with magnetization directions of [010] and [001] [55]. Figure 3.4 illustrates domain motion produced by an applied magnetic field.

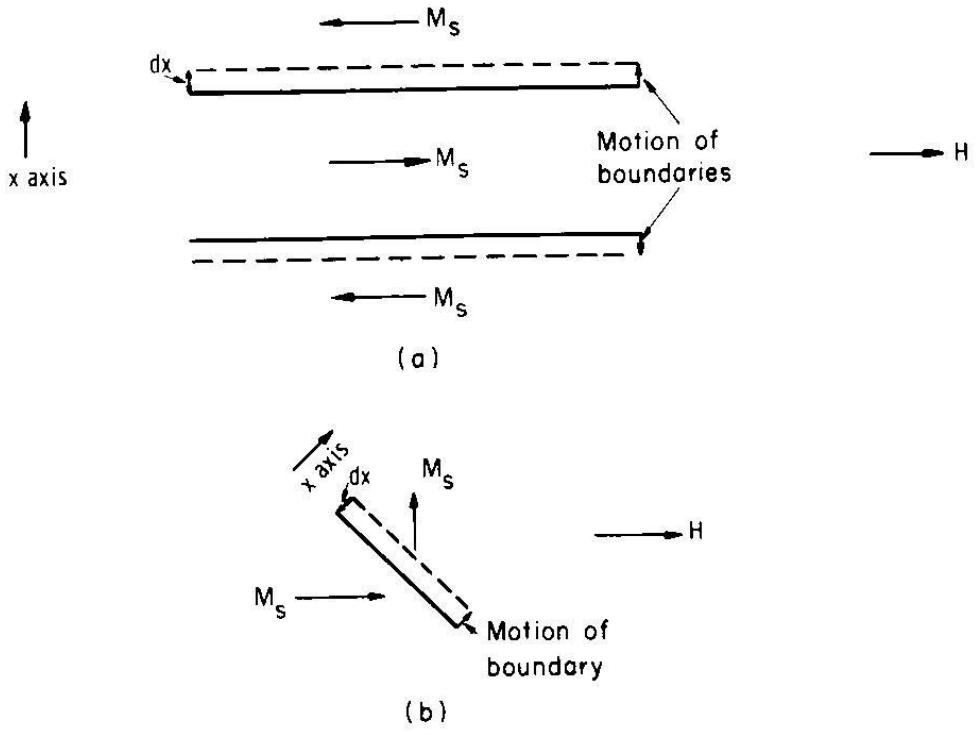

Figure 3.4. Domain wall motion relative to the direction of an external applied field, *H*, for (a) 180° and (b) 90° walls [56].

3.2.2. Exchange Interaction Energy

The dipole-dipole interaction is not greater than $k_B T_C$ and thus cannot overcome thermal disorder to cause magnetic ordering. The answer to the question of how magnetic dipoles align spontaneously is provided through quantum mechanics and the Heisenberg Hamiltonian:

$$\langle H \rangle = -2 J_{ex} \mathbf{s}_1 \cdot \mathbf{s}_2 , \tag{3.8}$$

where

$$J_{ex} = -K \boldsymbol{\mu}_1 \cdot \boldsymbol{\mu}_2 \tag{3.9}$$

is the exchange energy and $\mathbf{s}_1$ and $\mathbf{s}_2$ are the spins and $\boldsymbol{\mu}_1$ and $\boldsymbol{\mu}_2$ are the magnetic moments for two neighboring electrons [51, 57, 58]. Positive exchange energy values result in ferromagnetic exchange interactions. Parallel spins lower the electron-electron spin interaction energy at separation distances beyond strong binding in which the

ubiquitous Pauli exclusion principle is valid. This intermediate distance is defined by the ratio of interatomic spacing to the incomplete electron inner shell. Bethe's formulation of the exchange energy as a function of the interatomic distances r_{ab} and the radius of the incompletely filled *d* subshell is given by:

$$J_{ex} = \iint \psi_a^*(r_1)\psi_b^*(r_2)\left[\frac{1}{r_{ab}} - \frac{1}{r_{a2}} - \frac{1}{r_{b1}} + \frac{1}{r_{12}}\right]\psi_a(r_1)\psi_b(r_2)d\tau \qquad (3.10)$$

where r_{12} is the distance between the two electrons and r_{a2} and r_{b1} are the distances between the respective nuclei and electrons [51]. The Bethe-Slater curve shown in Figure 3.5 correctly predicts ferromagnetic behavior for iron, cobalt, and nickel.

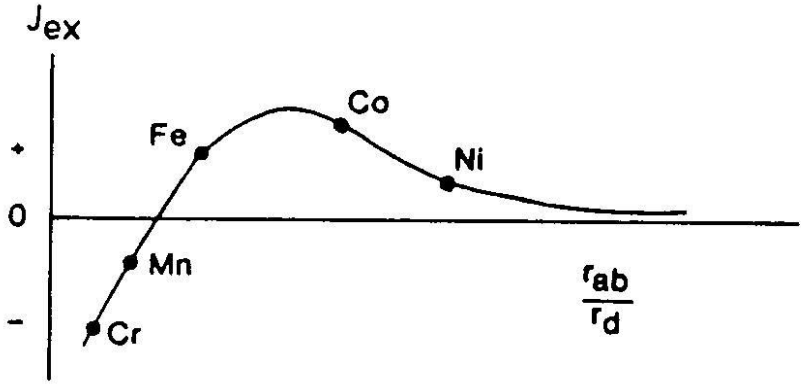

Figure 3.5. Bethe-Slater curve based on Equation 3.10 [51].

Ferromagnetic materials possess the following required electronic structural ingredients for strong exchange interaction energies: a low electron density overlap, a high density of states, and a Fermi energy surface within the *d*-band [32]. Figure 3.6 illustrates the effect of exchange interaction on the bands in nickel, accounting for the magneton number, n_B, listed in Table 3.1. The magneton number is the magnetization per atom at 0K.

Table 3.1. Magnetic data for ferromagnetic elements [32, 54].

Element	Structure	M (A·turns·m^{-1})	n_B	r_{ab}/r_d (from Figure 3.5)	Curie Temperature (K)
Fe	bcc	1.69 x 10^6	2.22	1.63	1043
Co	hcp	1.36 x 10^6	1.72	1.82	1404
Ni	fcc	0.47 x 10^6	0.60	1.97	631

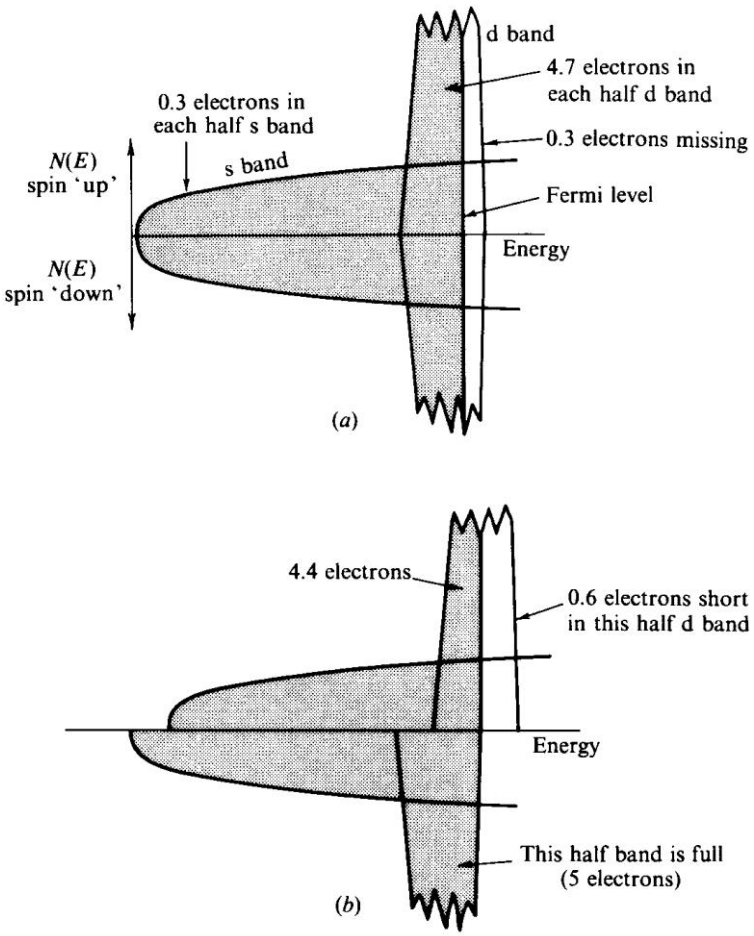

Figure 3.6. Density of states for nickel (a) without and (b) with the effect of the exchange energy interaction [32].

3.2.3. Bloch Wall

Due to the amount of energy required to reverse spin from one domain to another, magnetic domains tend to be quite large [55]. The finite distance between two domains

over which spin reversal takes place is known as the domain or Bloch wall, shown schematically in Figure 3.7. The energy per unit area of the wall is given by:

$$U^*_{wall} = U^*_{ex} + U^*_{an} = \frac{K\mu^2\pi^2}{2Na^2} + K'Na\,, \tag{3.11}$$

where U^*_{ex} and U^*_{an} are the exchange and anisotropy energies per unit area, μ is the magnetic moment, and K and K' are functions of crystalline direction. Figure 3.8 illustrates the thickness of a Bloch wall, d, in terms of number of atoms, N, and the lattice constant for the ferromagnetic material, a.

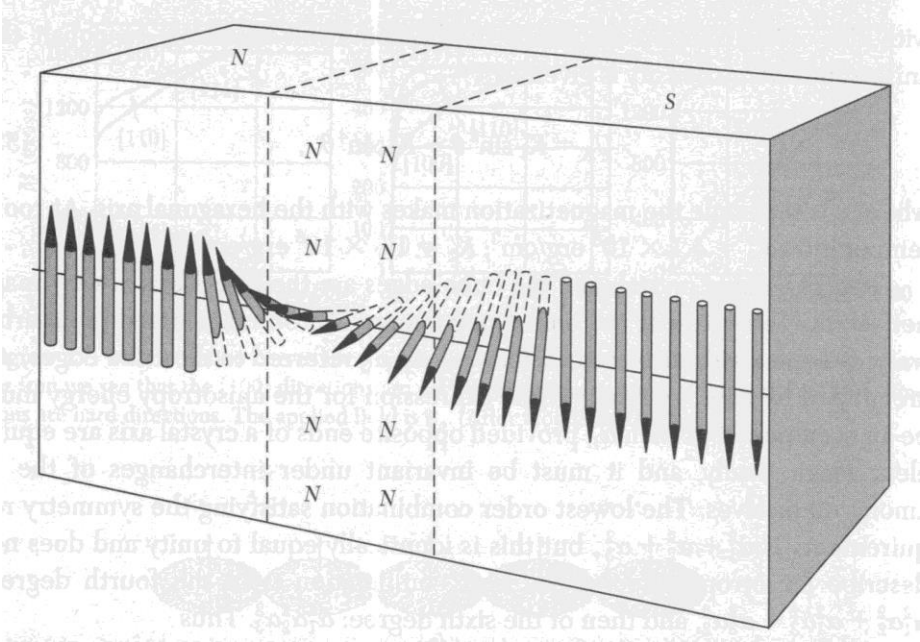

Figure 3.7. Schematic of a Bloch wall [59].

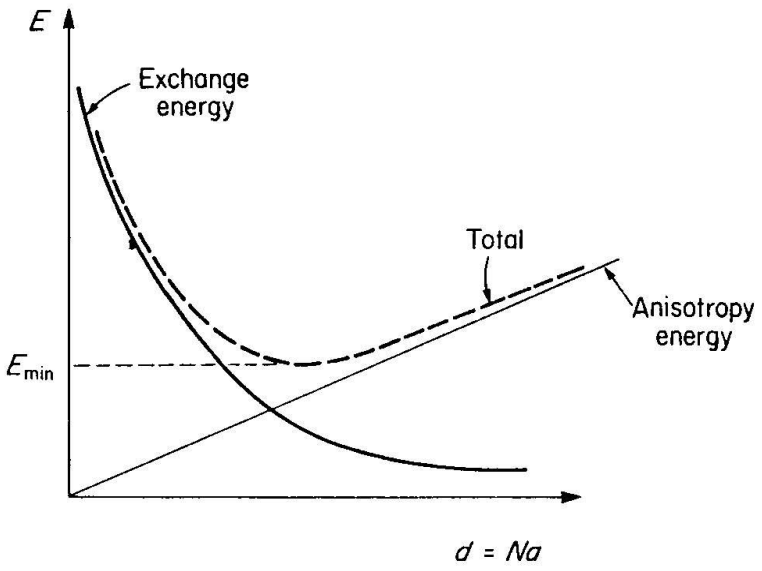

Figure 3.8. Bloch wall thickness corresponding to minimization of total wall energy [57].

3.2.4. Magnetic Hysteresis

The magnetization response of ferromagnetic materials is described by a hysteresis curve, a plot of the magnetic flux density, **B** (in $Wb \cdot m^{-2}$), induced by an external magnetic field, **H** (in $A \cdot m^{-1}$). The magnetic flux density, **B**, is defined by:

$$\mathbf{B} = \mu_0(\mathbf{H} + \mathbf{M}), \tag{3.12}$$

where

$$\mu_0 = 4\pi \text{ x } 10^{-7}\ H \cdot m^{-1} \tag{3.13}$$

is the permeability of free space and **M** (in $A \cdot m^{-1}$) is the magnetization, also known as the magnetic dipole moment density (number of magnetic dipole moments per unit volume). The resulting magnetization (**M**) from a given magnetic field (**H**) depends on the proportionality constant between **M** and **H** known as the magnetic susceptibility, χ_m.

It is common to express the induced field solely in terms of the applied field:

$$\mathbf{B} = \mu\mathbf{H} \tag{3.14}$$

through the relation

$$\mathbf{M} = \chi_m \mathbf{H} \tag{3.15}$$

where

$$\mu = \mu_0 (1 + \chi_m) \tag{3.16}$$

is the magnetic permeability of the material (in $H \cdot m^{-1}$). The magnetic permeability of a material is the instantaneous slope of a hysteresis graph. Bozorth divides the hysteresis curve of a previously unmagnetized material into three distinct sections in Figure 3.9. The three sections are divided by the "instep" at low field strength and the "knee" at higher field strength before saturation [54].

The first section of the curve, from toe to instep, is governed by the Rayleigh relation,

$$\mathbf{B} = \mu_0 \mathbf{H} + \nu \mathbf{H}^2 , \tag{3.17}$$

where

$$\nu = \frac{d\mu}{d\mathbf{H}} . \tag{3.18}$$

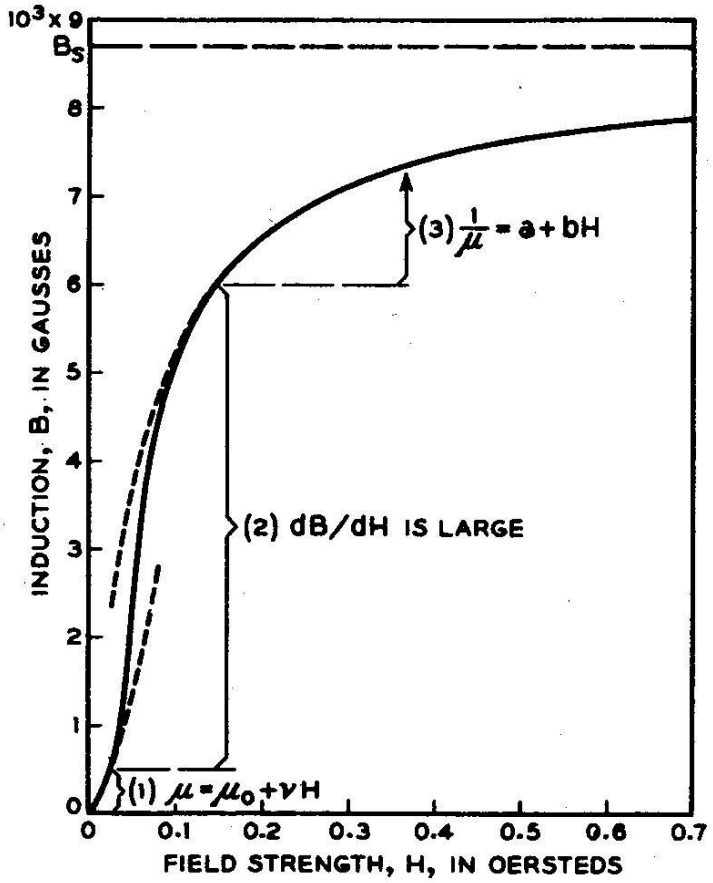

Figure 3.9. Initial magnetization hysteresis curve [54].

This first section is due to nearly reversible 180° wall motion, resulting in no magnetostriction, a dimensional change due to magnetization. It is assumed that in this initial magnetization step, the domain walls are making small displacements within an equilibrium energy well. The greatest slope of the hysteresis graph is the second section of the curve which is due to irreversible wall motion of both wall types. The third section of the curve can be approximated by the Frölich-Kennelly relation [54]:

$$\frac{1}{\mu} = a + b\mathbf{H} \,. \tag{3.19}$$

During this final magnetization step, the aligned domains undergo a reversible rotation to align with the external field. Figure 3.10 is a vector schematic of the magnetization steps outlined in Figure 3.11.

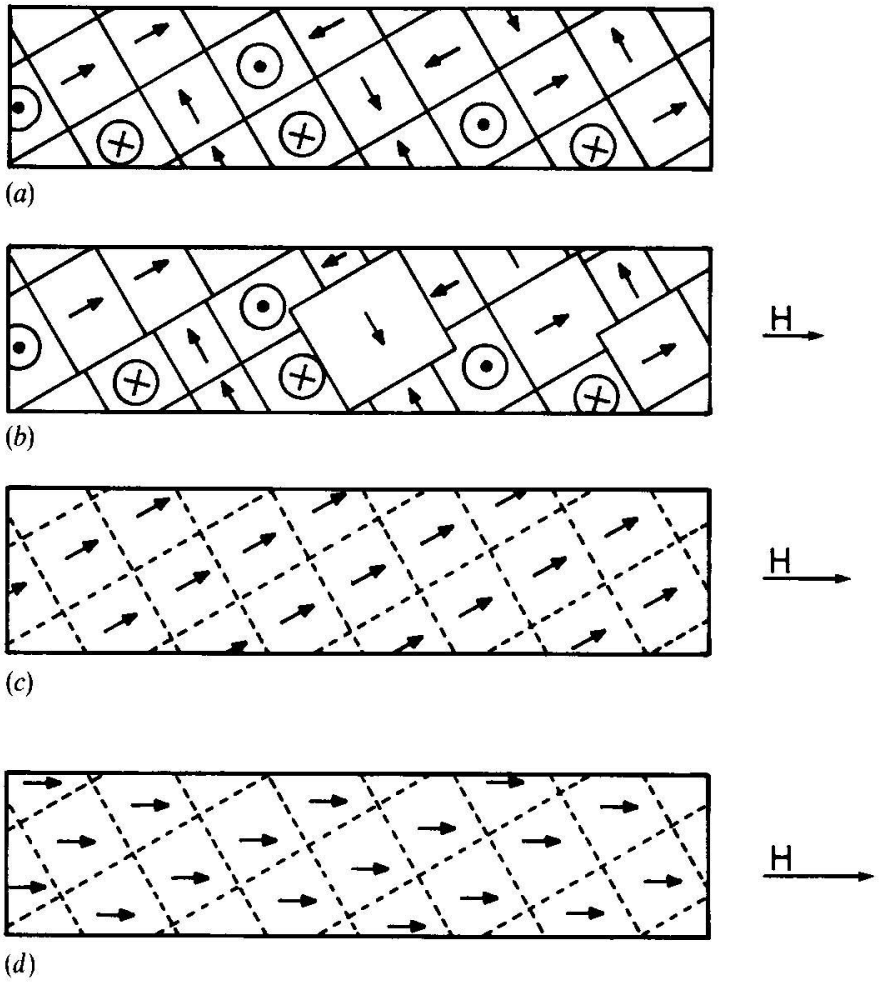

Figure 3.10. Domain movement during magnetization from (a) the unmagnetized state to (b) partial magnetization through reversible boundary displacement to (c) completion of sudden reversals (knee of magnetization curve) to (d) saturation magnetization by reversible domain rotations [51, 54].

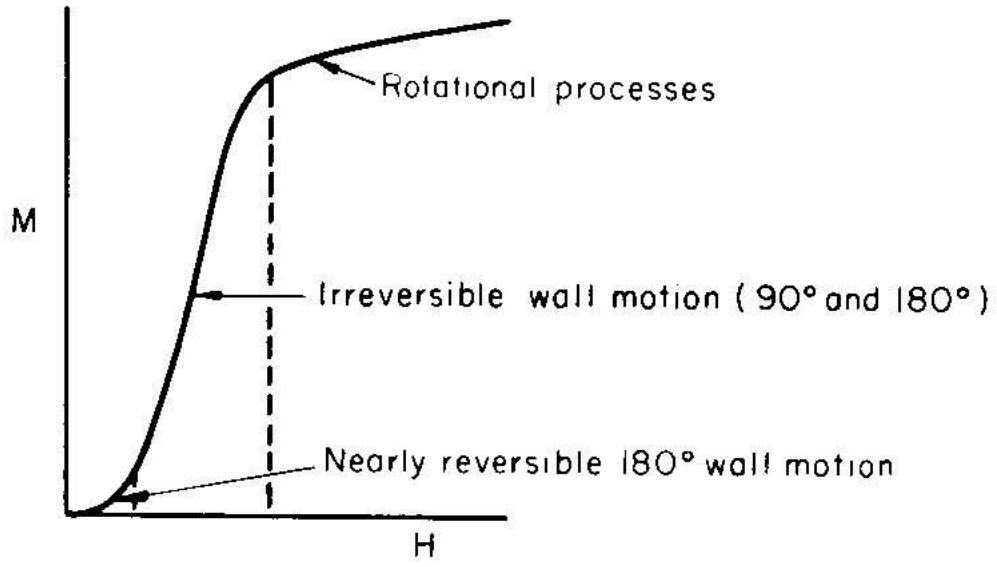

Figure 3.11. Magnetization curve regions [56].

3.2.4.1. Hysteretic Parameters

Common hysteretic parameters used to classify ferromagnetic materials are the magnetic permeability (μ), saturation levels (B_{max} and H_{max}), remanence (B_r), and coercivity (H_c), shown graphically in Figure 2.4. Often, a relative permeability value is given for a material. This quantity is the dimensionless ratio of permeability to permeability of free space.

The magnitude of the coercive force of a material has been traditionally used to distinguish hard and soft magnets. A hard type ferromagnet is characterized by larger coercive force values (generally above 10 $kA \cdot m^{-1}$ or 125 Oe) while a soft magnet will have a lower coercive force (below 1 $kA \cdot m^{-1}$ or 12.5 Oe) [51]. The coercive force is the amount of applied field required to remove the remanent induced flux density from a material. Therefore, a hard magnet will have a higher retentivity than a soft magnet. The energy required to complete one hysteresis cycle is proportional to the area of the hysteresis loop and can be correlated to the amount of energy lost during this process [57].

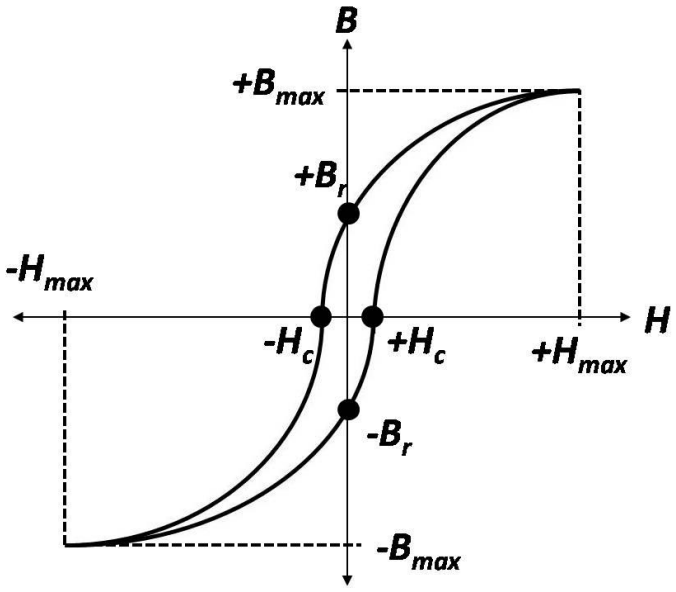

Figure 3.12. Typical ferromagnetic hysteresis curve.

Soft magnetic materials are useful as cores for transformers and power inductors because of their high magnetic permeability and low coercivity. The direct consequence of these attributes translates to a higher induced magnetic field with low hysteresis energy losses and ease of magnetic field reversal for alternating current applications. Figure 3.12 displays values of relative permeability and coercivity for a variety of ferromagnetic materials.

The underlying mechanisms behind the hysteretic response of ferromagnetic materials include the presence of dislocations, or the addition of non-magnetic alloys, and magnetic anisotropy [51]. Therefore, a steel alloy that has been hardened through cold working or by the addition of carbon will have increased coercivity and hysteresis loss over softer iron, as illustrated by Figure 3.13. Magnetic anisotropy accounts for the characteristic hysteretic delayed induced flux density response of a material to an external magnetic field intensity; the magnetic moments will be aligned with the preferred crystallographic directions and will align with the external applied field through a series of steps. These steps require energy and account for the hysteresis energy loss because the magnetic moments are removed from their thermodynamically favorable alignment.

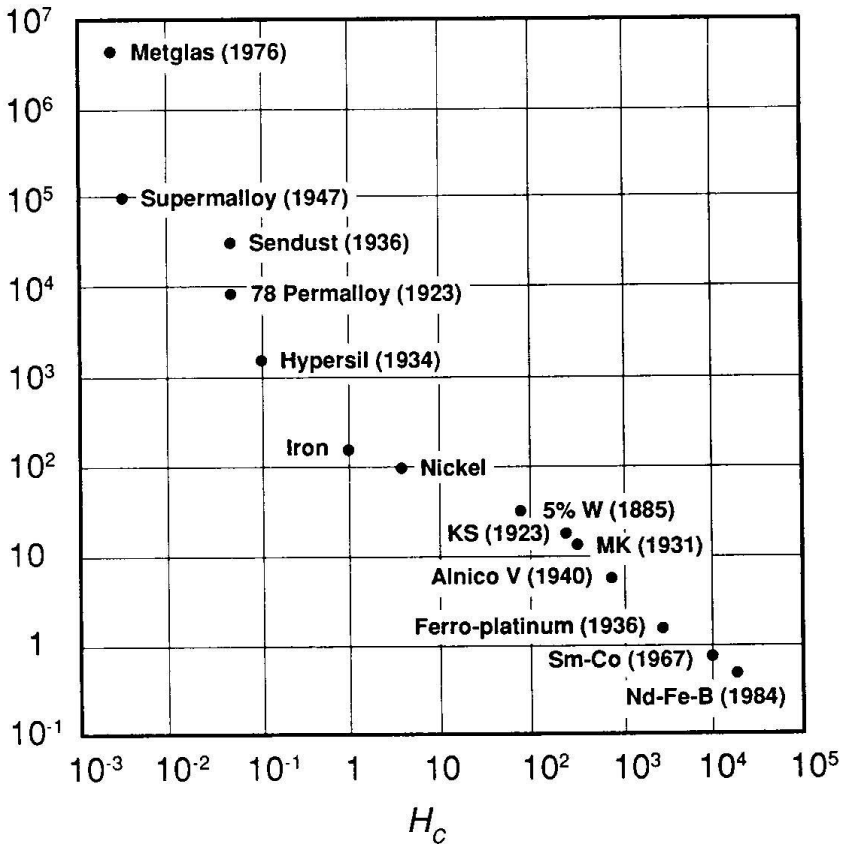

Figure 3.13. Values of relative permeability and coercivity for a range of ferromagnetic materials [51].

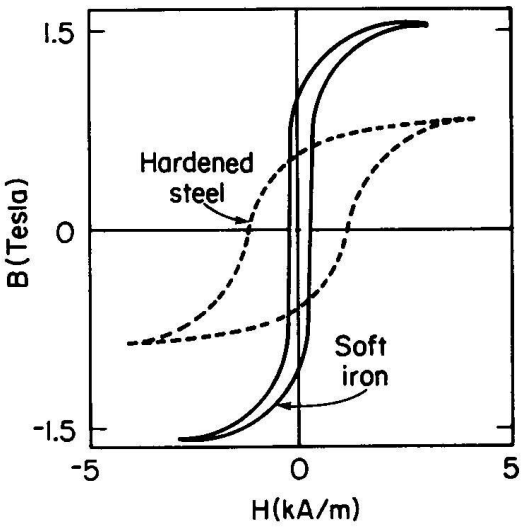

Figure 3.14. Hysteresis loss and coercivity comparison for hardened steel and soft iron [51].

3.2.4.2. Hysteresis Sensitivity

Hysteresis parameters have been correlated to mechanical stress levels, grain size, and dislocation densities in different grades of steel [60, 61, 62]. Atherton and Jiles monitored stress-induced changes in the fringing magnetic fields above a section of buried gas linepipe, shown in Figure 3.14. Figure 3.15 depicts the magnetostrictive behavior of iron which is demonstrated by the isostress hysteresis loops shown in Figure 3.16 for experimentally determined for XC10 French steel [61].

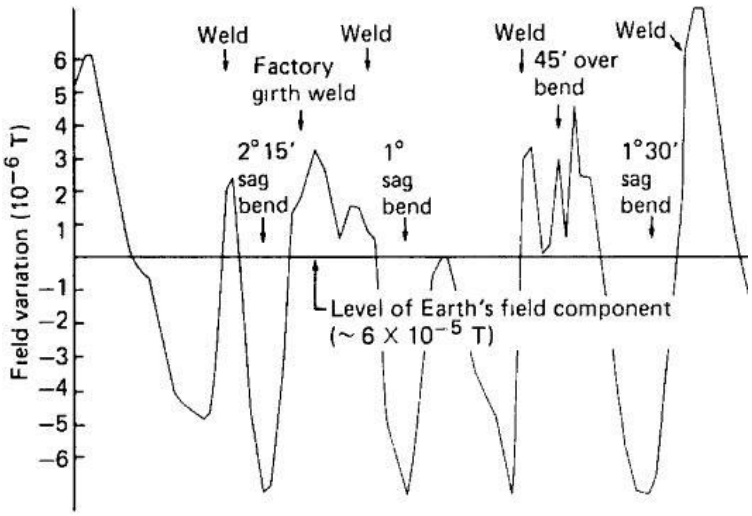

Figure 3.15. Fluxgate magnetometer readings of vertical magnetic flux leakage fields from buried 1.3 m diameter 13 mm wall linepipe [60].

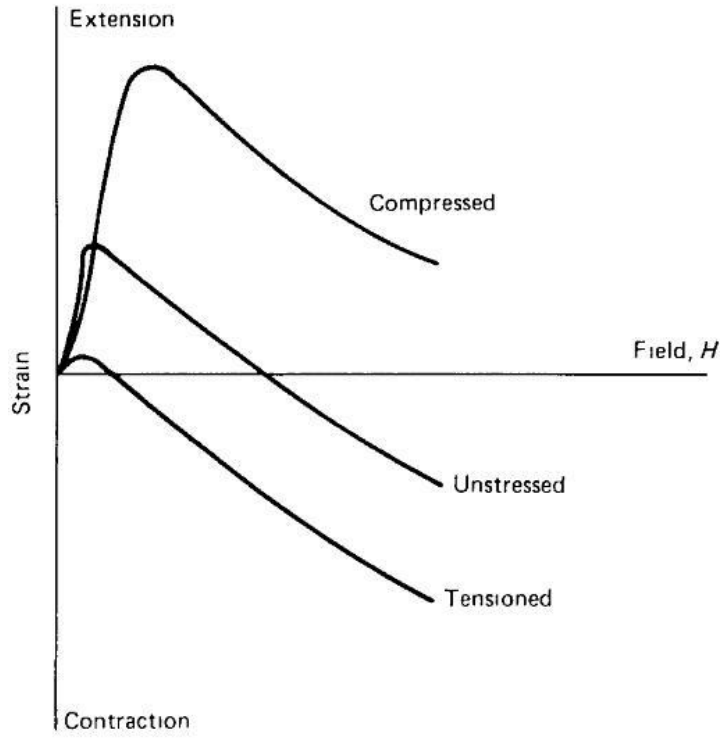

Figure 3.16. The magnetostrictive behavior of iron [60].

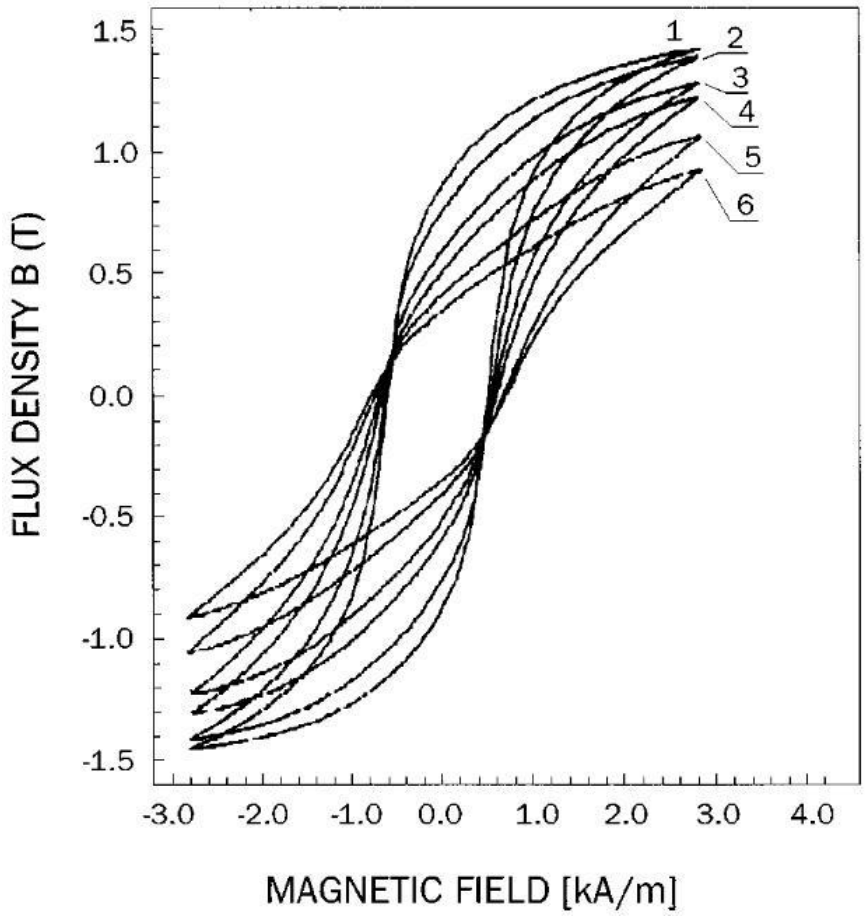

Figure 3.17. Experimental hysteresis loops in XC10 French steel (~0.1 wt pct. C) for the following stress levels (in MPa): (1) +114; (2) +50; (3) 0; (4) -37; (5) -104; (6) -162 [61].

Sablik modeled the changes in hysteresis parameters due to grain size for different magnetization directions and produced the trends reported in Figure 3.17. Embedded in Figure 3.17 are different values for the anisotropy energy density, K_u, which has nonzero values when individual crystal grains have the tendency to align, giving their lattices magnetocrystalline anisotropy.

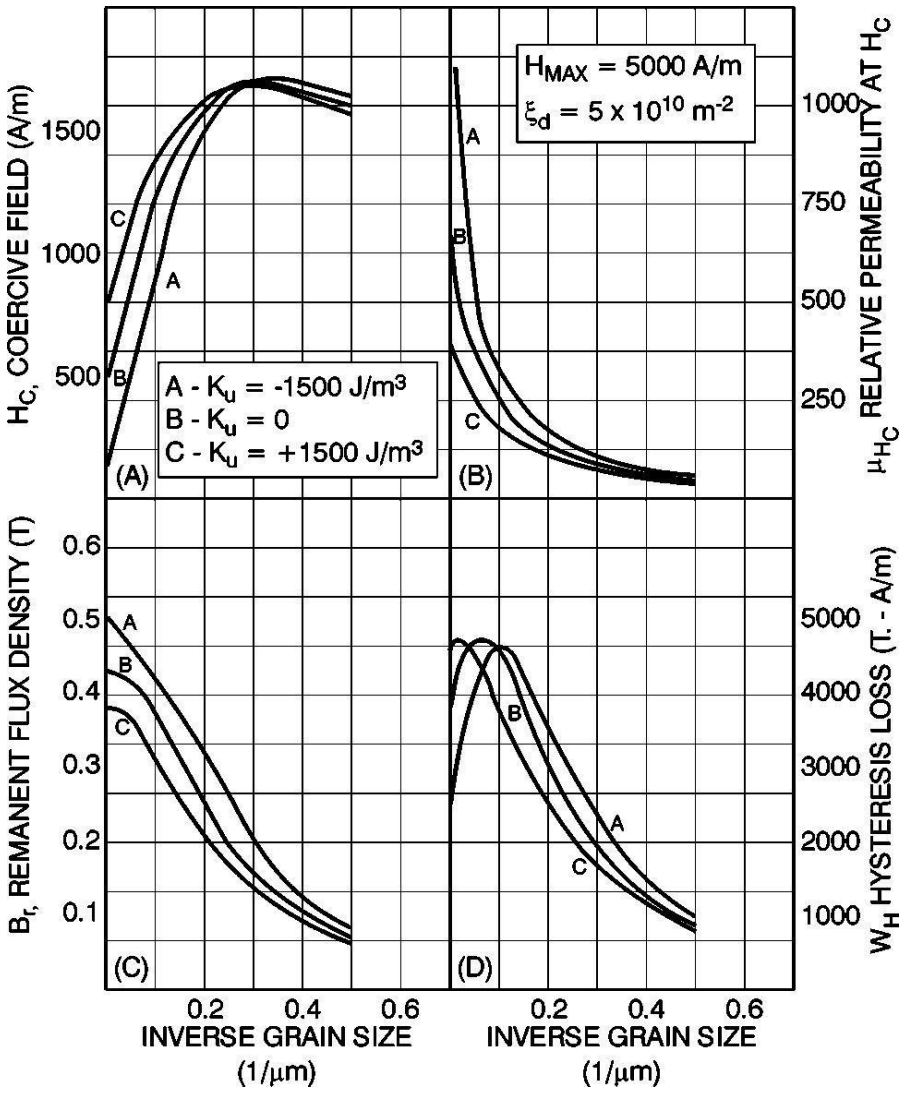

Figure 3.18. Computed variation of the (A) coercive field, (B) relative permeability at the coercive field, (C) remanent flux density, and (D) hysteresis loss as a function of inverse grain size for a dislocation density of 5 x 10^{10} m^{-2} and with $|H_{MAX}| < 5000$ A·m^{-1}. Curves A, B, and C, respectively, are for *H* parallel to the easy axis, no easy axis, and *H* parallel to the hard axis [62].

3.3. Harmonic Analysis of Induced Voltage

Ferromagnetic eddy current inspection is complicated due to the nonlinearity of the eddy current response in these materials [51]. Figure 3.16 has shown the hysteretic distinction of tensile and compressive stresses of different magnitudes. It is advantageous to exploit this nonlinearity through a harmonic analysis of the induced voltage signal. Low frequency impedance measurements are formulated from the peak-

to-peak voltage values of a sensor core, despite the nonsinusoidal nature of the sensing voltage signal. Harmonic analysis of the sensing voltage signal determines the presence and intensity of the higher harmonics of the exciting signal that combine to create the distorted signal response of the material being measured. A discrete Fourier transform is performed on a sensed voltage signal to identify the frequencies components of the voltage signal.

3.3.1. Hysteretic Parameters

For a long solenoid of length l and N turns, the magnetizing current, $i(t)$, and the magnetic field intensity, $H(t)$, are related by

$$i(t) = \frac{l}{N} H(t). \tag{3.20}$$

The application of a sinusoidal AC excitation current in a solenoid will produce a sinusoidal magnetic induction resulting in a nonsinusoidal symmetric magnetizing current as seen in Figure 3.18. The magnetizing current is an odd function of time and can be therefore expressed in the following Fourier series containing only odd terms:

$$i(t) = \sum_{k}^{\infty} (A_k \sin k\omega t + B_k \cos k\omega t), \tag{3.21}$$

where $k = 1, 3, 5, \ldots$ and where $H(t)$ has the same temporal functionality as $i(t)$.

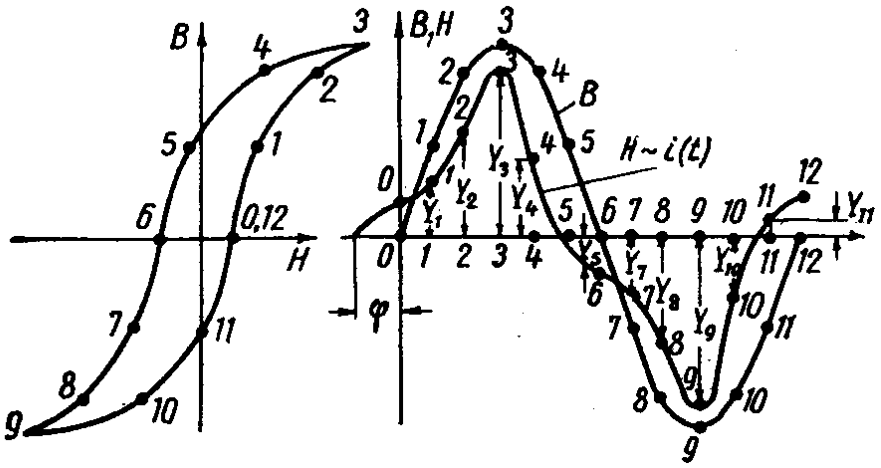

Figure 3.19. Plot of 2π-periodic, nonsinusoidal magnetic field intensity, $H(t)$, resulting from a sinusoidal magnetic flux density, $B(t)$ [63].

Gruska calculated *H(B)* through Chebyshev polynomials to relate hysteresis loop parameters to the Fourier coefficients, A_k and B_k. The following expression:

$$H(B) = 16A_5\left(\frac{B}{B_{\max}}\right)^5 - (4A_3 + 20A_5)\left(\frac{B}{B_{\max}}\right)^3 + (A_1 + 3A_3 + 5A_5)\left(\frac{B}{B_{\max}}\right) + \\ + \sqrt{1-\left(\frac{B}{B_{\max}}\right)^2}\left[16B_5\left(\frac{B}{B_{\max}}\right)^4 - (4B_3 + 12B_5)\left(\frac{B}{B_{\max}}\right)^2 + B_1 + B_3 + B_5\right] \tag{3.22}$$

yields the following relations:

$$H_C = H(B=0) = B_1 + B_3 + B_5 \tag{3.23}$$

and

$$H_{\max} = H(B = B_{\max}) = A_1 - A_3 + A_5, \tag{3.24}$$

for the first five harmonics [63].

The initial permeability, coercive force, and level of magnetic remanence have all been shown to be sensitive to the structural state of the material, in particular, lattice defects are proportional to the coercive force. Variations in chemical composition between materials are indicated by changes in the saturation magnetization and the Curie temperature [63, 64].

3.3.2. Stress Dependence of the Third Harmonic Amplitude

Kwun and Burkhardt studied the effect of grain size, stress, and hardness on SAE 4340 steel and AISI 410 stainless steel specimens and concluded that hysteresis parameters were insensitive to ASTM grain sizes ranging from 2 to 7. The hysteresis loops exhibited distinguishable hardness and stress effects due to stress-induced anisotropy [65]. The stress-induced anisotropy was used to investigate the uniaxial stress dependence of the third harmonic of the sensing coil voltage.

Magnetoelastic coupling causes changes of the hysteresis curve with the mechanical stress state of the material. The results of this study, shown in Figure 3.19, are typical for hysteresis loop stress responses of a material with positive magnetostriction such as iron.

Figure 3.19 confirms the third harmonic dependence on tensile stress reported by Shel [66, 67].

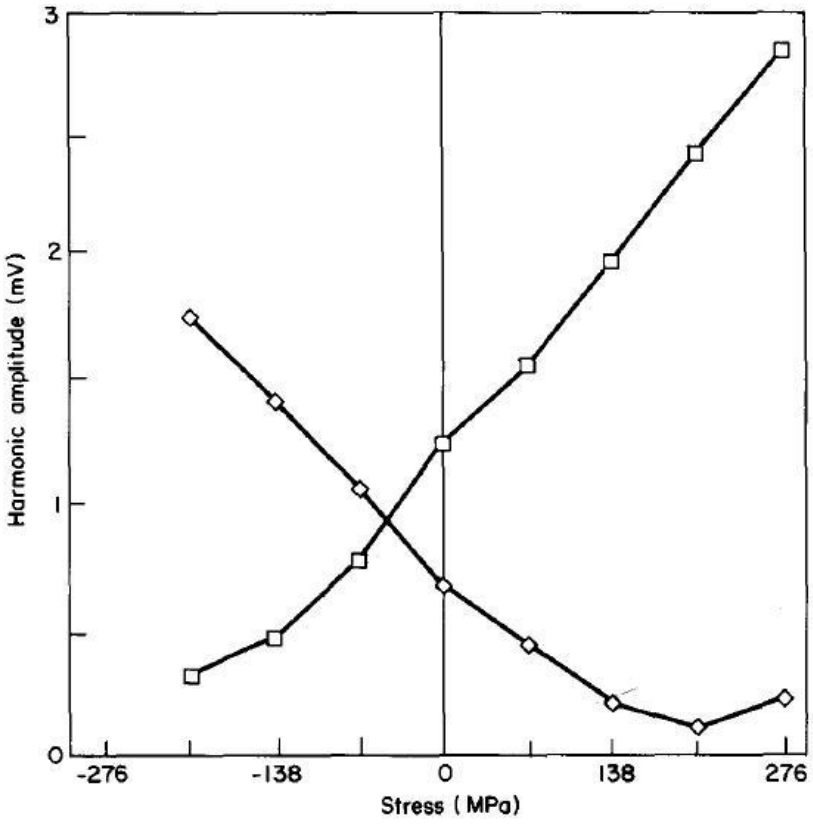

Figure 3.20. Typical stress dependence of the third harmonic amplitude for SAE 4340 steel at a frequency of 10 kHz. Coil alignment parallel (squares) and perpendicular (diamonds) to the stress direction [66].

3.4. Effect of Hydrogen on Magnetic Properties

The effect of hydrogen on transition metal magnetic properties is controversial. Ingress of hydrogen into iron and steel is reported to cause an increase [68, 69] or decrease [70] in the local magnetic moment. Gorkunov et al. reported an increase of coercive force and a decrease in magnetic permeability of 12GB grade tube steel (X42SS strength group) exposed to hydrogen sulfide for periods greater than 96 hours [71]. Hydrogenation of a nanocrystalline $Fe_{85}Zr_{3.5}Nb_{3.5}B_7Cu_1$ alloy resulted in a slight increase in saturation magnetization and a lowering of the magnetic permeability [72]. Kanadasamy et al. concluded that the main magnetic property change due to hydrogen implantation of cobalt-copper multilayers was increased resistivity [73].

Kronmüller reviewed the use of the magnetic relaxation method for studying hydrogen in ferromagnetic alloys and metals. Magnetic relaxation measurements are sensitive to lower hydrogen concentrations and therefore are beneficial for the study of materials with low hydrogen solubility. The interaction energy between hydrogen interstitial atoms and domain walls during the spontaneous magnetization occurring in ferromagnetic materials explains the basic functionality of this method. This interaction energy consists of both long- and short-range interactions. Elastic and magnetic dipolar comprise the long-range interactions. In latter transition metals, hydrogen transfers its electron primarily to the *d*-band and the proton is screened by *d*-band electrons, reducing the local magnetic moment by one Bohr magneton. There are two possible rearrangements hydrogen atoms undergo to lower the interaction energy with domain walls: 1) *orientation* adjustments if hydrogen interstitials are in anisotropic configurations and 2) *diffusion* over the width of the domain wall. Orientation and diffusion after effects result. As a consequence of the tetragonal symmetry of hydrogen atoms in a bcc iron lattice, there should be an orientation after effect. However, it is difficult to detect due to low hydrogen solubility (< 1 ppm) in α-Fe below room temperature. Hydrogen atoms in an fcc iron lattice have cubic symmetry and therefore produce neither diffusion nor orientation after effects [74].

CHAPTER 4 LITERATURE REVIEW OF HYDROGEN MEASUREMENT TECHNIQUES

A survey of diffusible hydrogen measurement techniques for weld specimens was reported by Quintana et al. in 1998 [75]. This survey ranged from the ANSI/AWS standard A4.4-93 covering diffusible hydrogen determination from arc welding for a variety of steel microstructures to other non-standard measurement methods [76]. Non-standard methods presented include electrochemical detection, neodymium dihydride formation and subsequent microscopic inspection, electrochromic reactions with transition metal oxides, and the detection of voltage differences to hydrogen passivation of a silicon-based dosimeter. While the hydrogen detection sensitivity is reported to be quite low (down to 10^{-14} torr), all of these methods required direct contact of the weld bead metal surface. Smith utilized laser ablation/mass spectroscopy to monitor total hydrogen content of welds shown in Figure 4.2 [77]. Smith et al. developed an opto-electronic diffusible hydrogen sensor based on the monitoring of an electrochromic reaction between hydrogen and a transition metal oxide [78].

A destructive experimental method commonly used to identify hydrogen trapping sites is thermal desorption analysis (TDA). Hydrogen is desorbed from a specimen subjected to a constant heating rate, as seen in a desorption profile in Figure 4.1. Characteristic peaks for specific trapping sites are observed at different temperatures [16, 79, 80].

Thermoelectric power measurements, a nondestructive contact method has demonstrated tremendous sensitivity to hydrogen content in steels and hydrogen storage materials [81, 82].

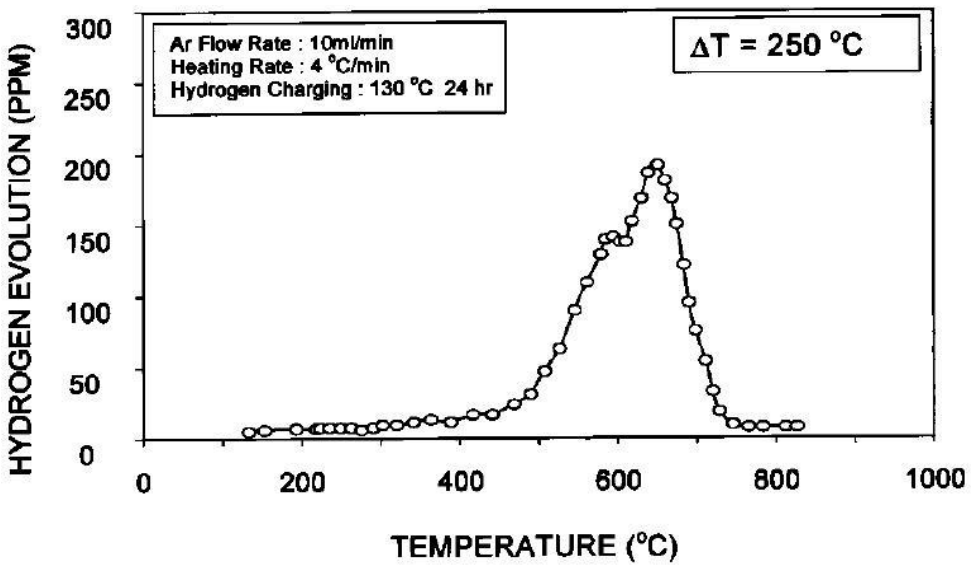

Figure 4.1. Thermal desorption analysis of a hydrogen charged dual-phase steel sample [15].

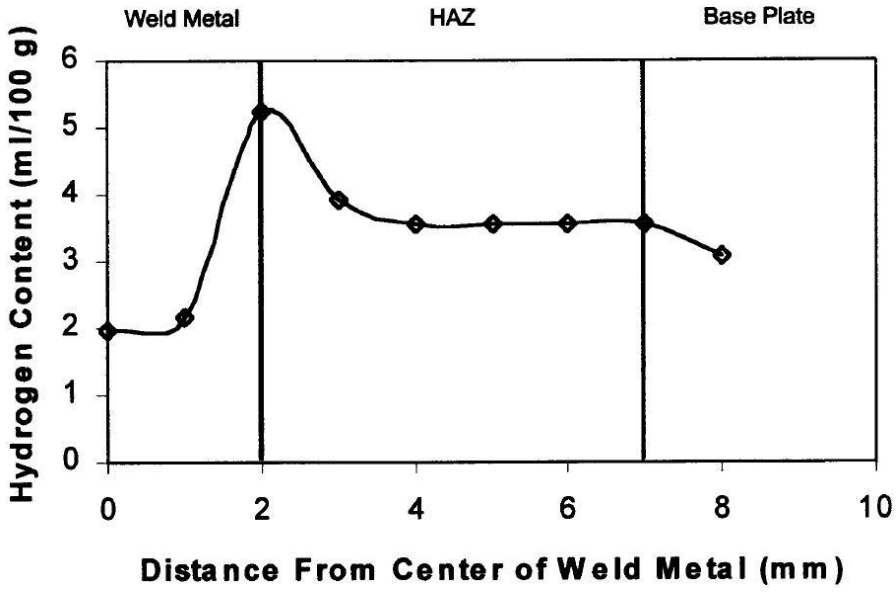

Figure 4.2. Weld metal hydrogen content as determined by laser ablation/mass spectrometry [77].

CHAPTER 5 STATEMENT OF THE EXPERIMENTAL OBJECTIVES TO BE ANALYZED

The development of a nondestructive electromagnetic sensor to assess hydrogen content in coated linepipe steel must meet certain criteria. Portability is essential for field measurements of in-service linepipes. The sensor and experimental procedure must be able to account for the variables associated with hydrogen content assessment in coated linepipe weldments: base metal and weld microstructure, coating thicknesses and type, varying linepipe radii, weld crown variability, temperature changes, and hydrogen content. Systematic accounting of these experimental and environmental variables will result in the successful calibration of the sensor.

This project requires a scale-up and enhancement (Chapter 7) of previous methods (Chapter 6) to make measurements on thick-walled sections of linepipe steel. Procedures and materials should be developed to ensure the sensor induction field will distinguish between experimental parameters and detect hydrogen at low levels (< 5 wt. ppm). Resolution of signal is important for measurement of hydrogen distribution in welds. Sensor design must address variability in weld crown bead profile and linepipe size.

CHAPTER 6 PRIOR RESEARCH UTILIZING LOW FREQUENCY IMPEDANCE FOR HYDROGEN CONTENT DETERMINATION OF HIGH STRENGTH LINEPIPE STEEL

The development of a low frequency impedance hydrogen sensor for coated linepipe steel and weldments began in the laboratory. First it was necessary to prove that low frequency impedance could be correlated to hydrogen content in linepipe steel. The low frequency impedance laboratory results for hydrogen content as a function of frequency for hydrogen charged X80 (80 ksi yield strength) linepipe steel is shown in Figure 6.1. The cylindrical X80 steel linepipe specimens had total hydrogen contents ranging from 0.78 to 28.4 ppm of hydrogen as determined by the LECO RH-404 Hydrogen Determinator. The RH-404 has a precision of the greater of 0.05 ppm or 2% RSD, for a one gram sample. However, there are no calibration standards for levels below 1.0 ppm.

The results are most important at lower frequencies (100 Hz) to guarantee a maximum penetration depth of five mm beneath the steel surface. At frequencies beyond 1000 Hz, only skin effects become important and these measurements cannot be attributed to variations in hydrogen content in the steel.

In Figure 6.1, notice how the impedance at 100 Hz increases with increasing hydrogen content. Not only are there measurable changes in impedance, but the sensitivity of the impedance measurements is exceptional. It cannot only measure hydrogen below 1.0 ppm, but it can also distinguish between 0.76 and 0.90 ppm of hydrogen [82]. As the steel strength increases, the tolerance for hydrogen approaches these small hydrogen contents. These low levels of hydrogen detection are within the uncertainty of chemical methods, but appear to be clearly measurable with physical electromagnetic tools [82]. These results were obtained with an encircling coil wrapped around cylindrical X80 linepipe steel specimens, as shown in Figure 6.2. These laboratory results utilizing induced current impedance measurements demonstrate that it is feasible to develop electromagnetic measurements to assess hydrogen content in steel [82].

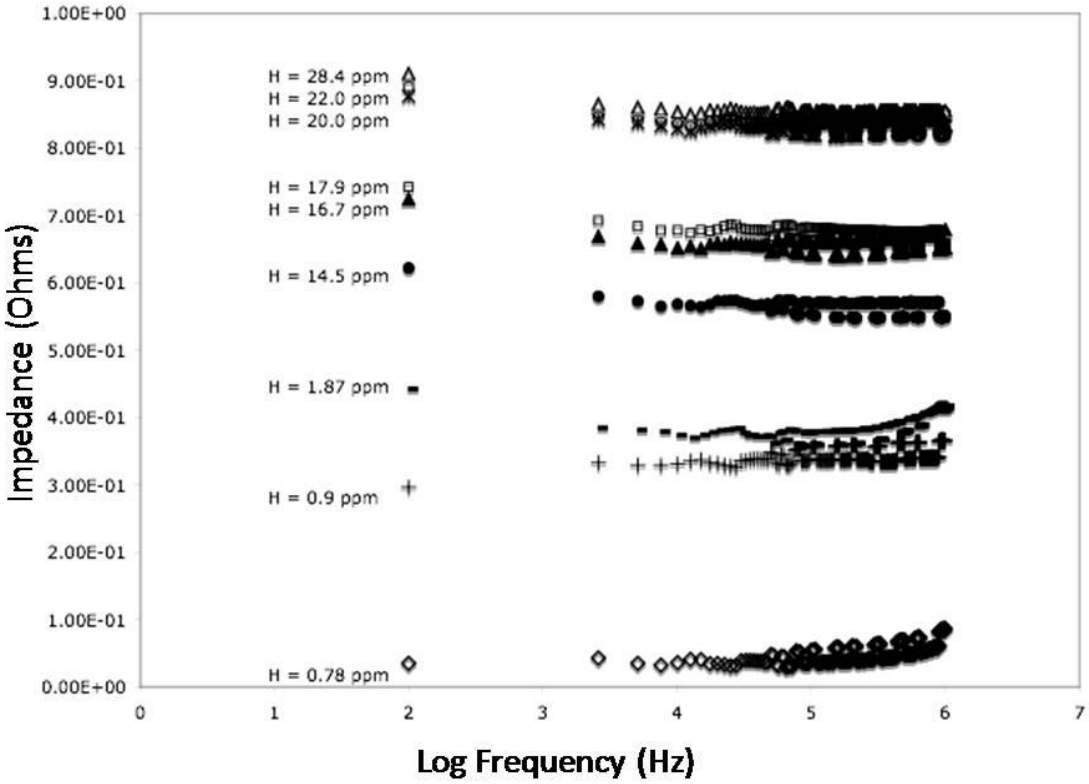

Figure 6.1. Frequency sweep of impedance with change in hydrogen content in tin coated hydrogen charged X80 linepipe steel specimens [82].

Figure 6.2. Coil encircling an X80 linepipe steel laboratory specimen [82].

To be able to utilize the low frequency impedance measurements in the field, a means of separating all of the variables present in a linepipe is necessary. At low frequencies, the measured impedance is approximately resistance (assuming capacitance is negligible), which is proportional to net resistivity of the inspected material and the conductive coil wire. The resistivity of the coil wire is a function of temperature, whereas the net resistivity of the inspected material is a function of independent eddy

current scattering processes. The net resistivity must also be considered when determining the change in resistance due to the addition of hydrogen atoms. According to Matthieson's rule, the resistivities due to independent scattering processes, such as thermal vibrations, lattice imperfections, and the addition of hydrogen atoms, are additive [33]. A general expression for the resistivities in steel is given by Equation 6.1 [82].

$$\rho_{net} = \rho_{thermal} + \rho_{lattice} + \rho_{hydrogen}[H] \tag{6.1}$$

When a hydrogen atom in solution enters the metal lattice, the hydrogen donates it electron to the host iron metal d-band and inhabits the interstitial sites as an unshielded proton. The Coulombic repulsion between the hydrogen ion and the iron atoms strains the local lattice and acts as a source of scattering [33]. The scattering due to the hydrogen atoms is independent of thermal scattering.

When considering the effects of the net resistivity due to the lattice (defects, grain boundaries, etc.), temperature, and hydrogen, notice in Figure 6.3 how the resistivity due to hydrogen content is a function of the slope of the line and therefore the resistivity due to temperature and lattice variables may be accounted for in the y-intercept [82]. Using this information, it may be possible to calibrate specimens with temperature and lattice as variables utilizing the same induced current impedance measurements as used for hydrogen content determination [82].

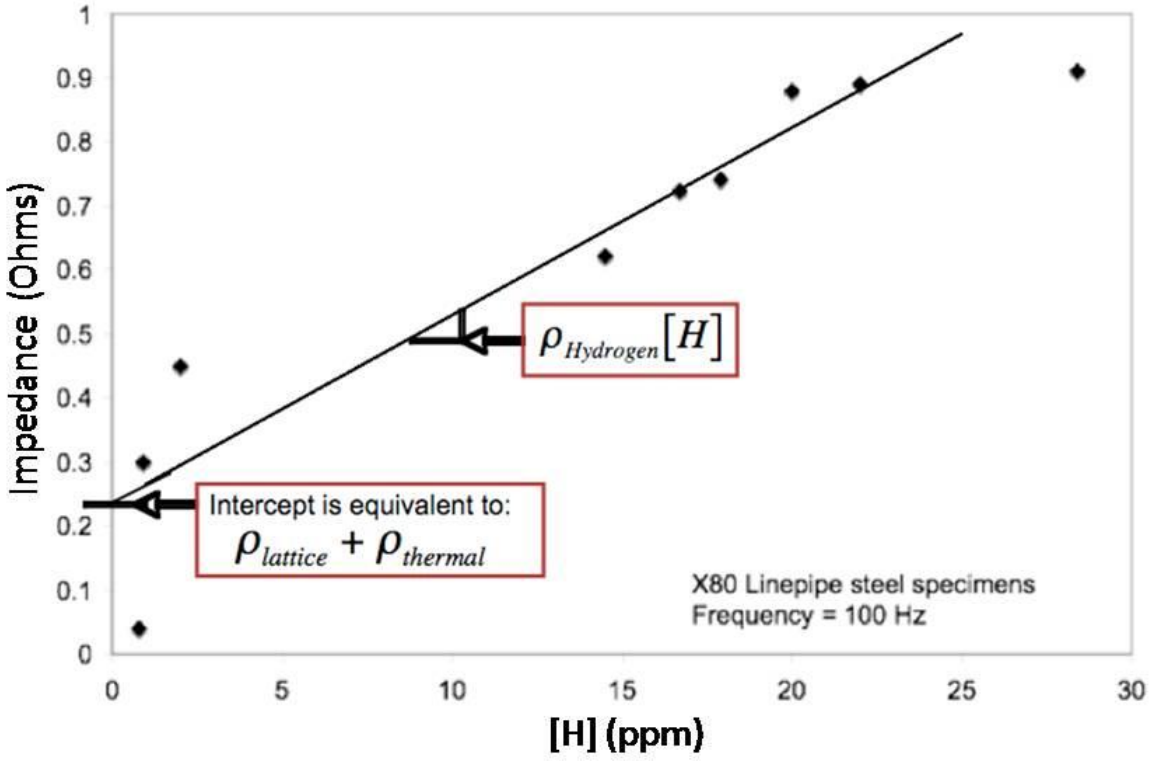

Figure 6.3. Impedance measurements as a function of hydrogen content at a frequency of 100 Hz. The resistivity of hydrogen is given by the slope of the line and the y-intercept is the sum of resistivities due to temperature and the lattice [82].

CHAPTER 7 FIELD SENSOR DEVELOPMENT

This chapter describes the efforts taken to scale up the previous laboratory efforts depicted in Chapter 6 to develop a field-scale sensor capable of making measurementson coated thick-walled high strength steel linepipes.

7.1. Equipment Selection

Numerous manufacturers of LCR meters were contacted for product evaluation and comparison. For equipment selection for hydrogen content determination there are a number of criteria that must be met: (1) operation at very low frequencies (< 100 Hz) because most eddy current units currently used in the field operate at very high frequencies to detect cracks, wastage, surface anomalies, etc, therefore equipment modification is necessary, (2) high precision and accuracy at low frequency to detect hydrogen, (3) high operating current for induction of very high magnetic fields to overcome magnetic remanence in linepipe and coating, and (4) multi-channel equipment to run multiple parameters simultaneously to normalize results.

Initial equipment selection began with receiving loaned equipment from companies to run induced current measurements on linepipes. Three high-precision LCR meters were evaluated: 1) Agilent E4980A, 2) QuadTech 7400, and 3) Hioki 3532-50. The Agilent E4980A LCR Precision LCR meter was chosen based on its excellent performance meeting or exceeding our selection criteria.

Figure 7.1. Agilent E4980A Precision LCR Meter.

Table 7.1. Features of Agilent E4980A LCR Precision Meter.

Frequency	20 Hz to 2 MHz
Impedance Resolution	1 mΩ
Accuracy	0.05 %
Voltage	40V DC Bias
Max Current	100 mAmps
Range Dependent Source	100 Ω
Data Transfer Capability	LAN, USB, GPIB

7.2. Scale-Up of Sensor Coil

The coil design also plays a very large role in equipment selection. The coil can help either maximize or minimize the induced magnetic field. Different coil arrangements have been investigated for each LCR meter. To obtain the most accurate impedance results for hydrogen content determination, the sensitivity of the measurement needs to be optimized such as in minimization of AC resistance, reduction of capacitance, etc. Optimization through minimization of the AC resistance is described. This section further describes the initial coil fabrication and modeling of the induced magnetic field.

7.2.1. AC Resistive Losses

It is desirable to minimize the AC resistance of the coil wire to minimize resistive heating loss and thereby maximize the power output. The AC resistance within the copper wire due to the AC current flowing through the wire is given by:

$$R_{AC} = \frac{\sinh(2d') + \sin(2d')}{\cosh(2d') - \cos(2d')} \tag{7.1}$$

The argument d' in Equation 7.1 is the ratio of the wire diameter to the standard depth of penetration within the copper wire:

$$d' = \frac{d_{wire}}{\delta_{Cu}} \tag{7.2}$$

For a copper wire, the standard depth of penetration is [83]:

$$\delta_{Cu} \cong \frac{6.6}{\sqrt{f}}. \tag{7.3}$$

The initial coil evaluation during the 1st Quarter focused on the minimization of AC resistance. It is desirable to minimize the AC resistance of the coil wire to minimize resistive heating loss and thereby maximize the power output. However, the coils made to minimize AC resistance had too low of an impedance to be detected by the LCR meter. The baseline coil impedance must be greater than 1 mΩ, the resolution of the E4980A LCR meter. Future coil development effort focused on homogenizing the induced magnetic field.

7.2.2. Coil Orientation

Different coil and steel configurations were tested to determine the optimal coil orientation. The magnetic flux density lines of a coil with the solenoid axis vertical or horizontal on a horizontal steel specimen were modeled using a finite element modeling program called Vizimag. The following parameters were assumed: a) the magnetic permeability of the steel is constant at 150, b) the coil current is 98 mA, and c) the coil is a 150-turn AWG 22-gauge coil.

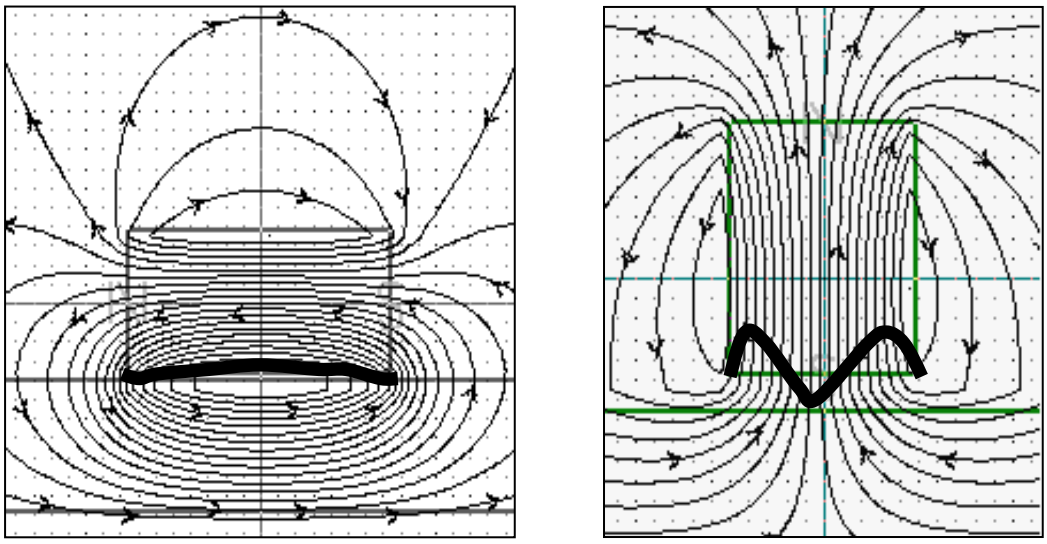

(a) (b)

Figure 7.2. Magnetic flux density field lines (thin lines with arrows) and surface flux density profile (heavy lines) of a coil (small rectangular box) atop steel plate (width of picture below coil) in (a) horizontal orientation with coil axis parallel to plate surface and (b) vertical orientation with coil axis perpendicular to plate surface.

Figure 7.2(a) shows the uniformity of the magnetic flux density when the coil is oriented horizontally. In contrast, Figure 7.2(b) shows that a vertically oriented coil will produce a flux density that varies approximately fifty percent from the edge of the coil decreasing axially. A homogenized flux density profile is advantageous for increasing the resolution of the sensor coil; any deviations from constant flux density could either mask or augment impedance signals from regions of interest in and around the weld.

7.2.3. Permanent Magnetic Yoke

Many non-destructive evaluation sources mention the use of magnetic yokes when eddy current testing ferromagnetic specimens. The permanent applied field from this permanent magnet yoke lowers the magnetic permeability of the steel and thereby increases the depth of penetration of the low frequency impedance sensor. Figure 7.3 shows the permanent yoke setup with the horizontal coil arrangement from Figure 7.2 in place, resulting in a homogenized induced B field.

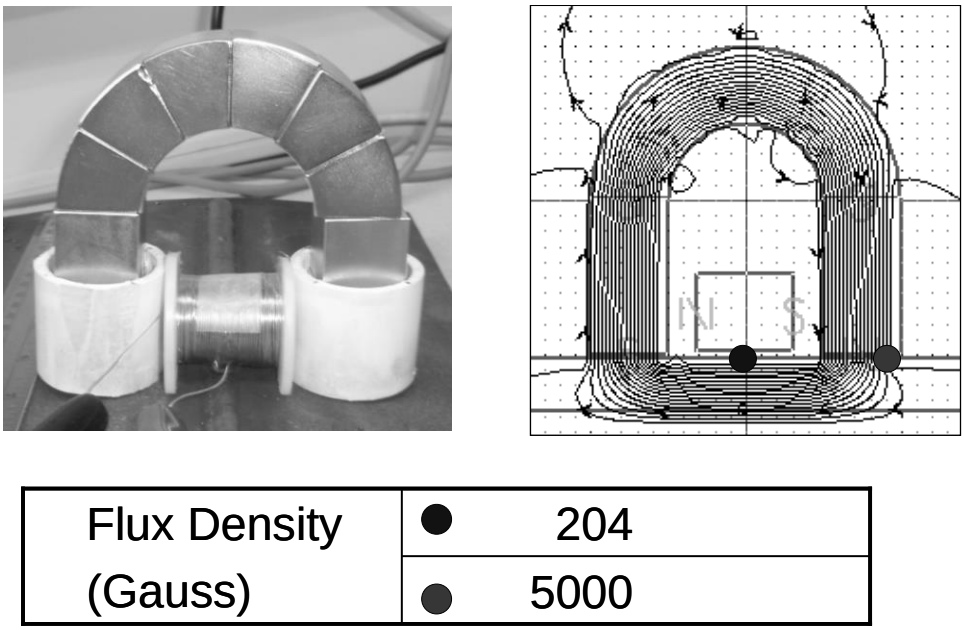

Figure 7.3. Permanent magnetic yoke setup.

The yoke is comprised of six neodymium iron boron magnet segments to form an arch and four 1-in. (25.4 mm) cubes to create a horseshoe. The strength of the magnet is greater than one Tesla, or 10,000 Gauss. A gauss meter measured the magnetic flux densities for the spots in Figure 7.3. The red spot is a gap between the flat magnet base and the curved pipe where the flux density is 5,000 Gauss.

7.2.4. Effect of a Remanent Magnetic Field

In-service linepipes often have remnant magnetic fields as a by-product of MFL pigs. Similar to the effect of the permanent magnetic yoke, this permanent magnetic field will lower the magnetic permeability of the linepipe steel.

7.3. Coil Calibration

A practical interpretation of the low frequency impedance signal requires the separation of several variables from changing hydrogen content. These variables include:

- Microstructure
- Temperature
- Coating

- Aging
- Defects

It is important to note that all of these variables are expected to have signature impedances that are much lower than the impedance of diffusible hydrogen. However, to effectively deconvolute the impedance signal, the coil must be calibrated to address these signature impedance signals. The coil sensitivity to variations in weld microstructure and hydrogen shield gas content of GMA welds has been investigated.

7.3.1. Base Metal Microstructure

Figure 7.4 compares the hydrogen content impedance signal for gaseously charged X80 steel linepipe with uncharged X52, X65, X80, and X100 linepipe steel specimens. It was previously believed that a multiple NDE tool approach (EMAT, MBN) would be needed to deconvolute a combined microstructural and hydrogen content impedance signal. However, as can be seen in Figure 7.4, the impedance signals of the various steel classes are distinguishable but insignificant compared to the much stronger hydrogen content signal.

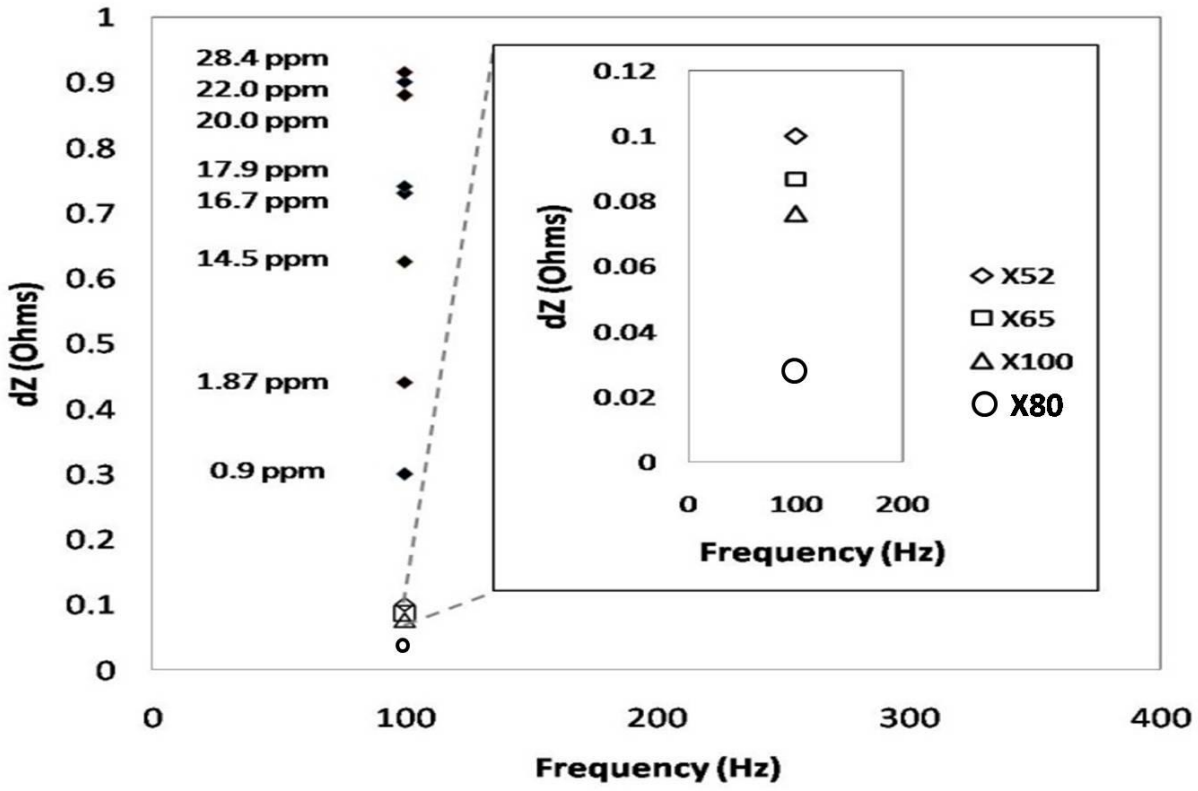

Figure 7.4. Hydrogen content impedance for hydrogen charged X80 linepipe steel specimens at 100 Hz. *Embedded figure is uncharged base metal linepipe steel microstructure impedance (X52, X65, X80, and X100)* [84].

7.3.2. Varying Weld Bead Microstructure

To detect differences in weld microstructure, a GMA weld bead was laid on an X100 steel plate with 100 pct. argon shielding gas. Changes in microstructure were introduced by varying the weld travel speed in three regions from 8.7 to 13.5 to 18.6 IPM. The 12-in. long test weld specimen is shown in Figure 7.5. Micrographs of the weld at the 2-in. (50.8 mm), 7-in. (177.8 mm), and 10-in. (254 mm) spots on the weld were taken as representative sections for the varying weld speed and are shown in Figure 7.6.

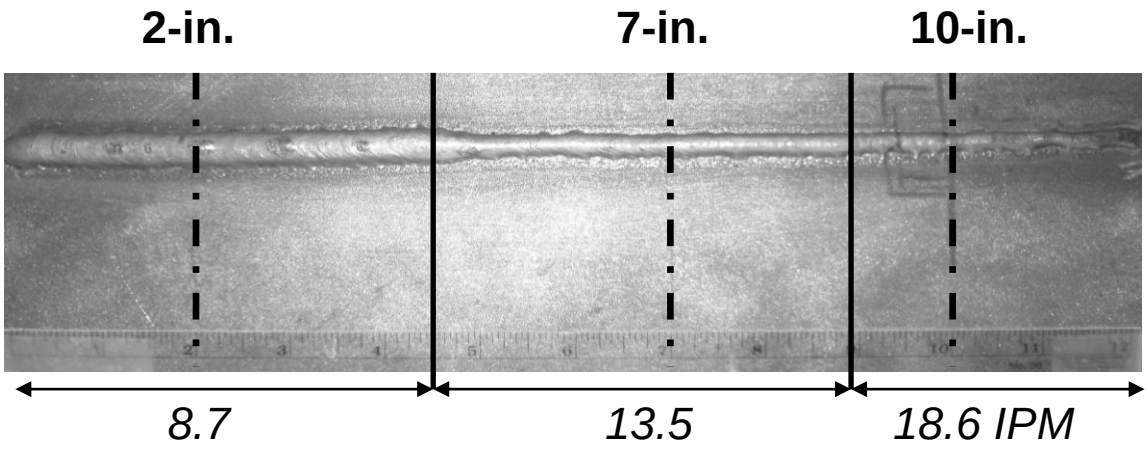

Figure 7.5. GMA weld with varying weld travel speed (8.7, 13.5 and 18.6 IPM).

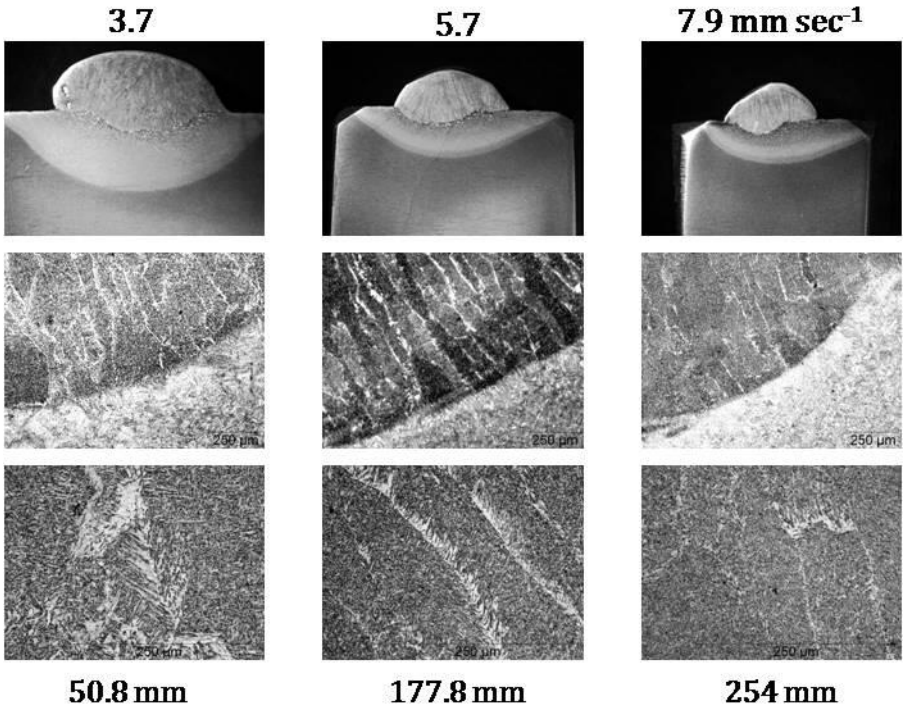

Figure 7.6. (top to bottom) Stereographs (7x) and micrographs depicting the variation in weld bead microstructure at the fusion line (10x) and within the bead (20x) [85].

7.3.3. Varying Shielding Gas Content

By holding all other welding parameters constant, the hydrogen content of a GMA weld bead on an X100 linepipe steel plate can be varied according to the hydrogen content of the shielding gas. The hydrogen content of the shielding gas was varied from 0 pct. with argon to 2 and 5 pct. A low frequency impedance measurement was initiated on the weld within five minutes post-weld. A LabVIEW DAQ program enabled a time evolution study of impedance changes of the weld bead.

The current absolute sensor coil under development is a 250-turn AWG 26 coil wrapped around an AWG 4 solid copper core. The coil is potted in epoxy resin for stability and weld heat resistance. A baseline impedance measurement is taken of the permanent magnet yoke and sensor setup for over an hour. The sensor coil is parallel to the weld, with a lift-off of 0.032 inches (0.8128 mm) provided by the AWG 20 wire ties. Pictures of the yoked sensor coil are shown in Figure 7.7.

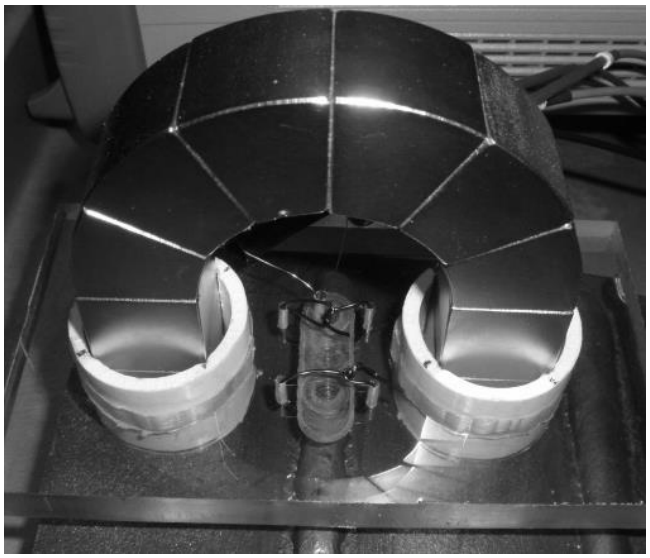

Figure 7.7. The sensor coil and yoke setup for the GMA shield gas experiment

The different welds produced on the same X100 linepipe steel sample are shown in Figure A.8. The heat input for each weld should be nearly the same with an estimated variance of ten percent. The voltage was set at 30.0 V, the wire feed speed was 454 in·min^{-1} (192.2 mm·s^{-1}), the travel speed set to 8.7 in·min^{-1} (192.2 mm·s^{-1}), and the current ranged from 200 to 240 A.

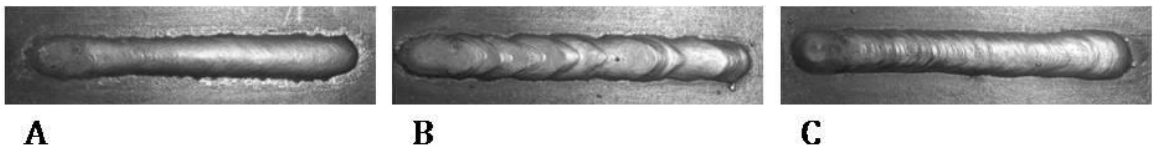

Figure 7.8. GMA welds on X100 linepipe steel with (A) 0 pct. hydrogen, (B) 2 pct. hydrogen / 98 pct. argon, and (C) 5 pct. hydrogen / 95 pct. argon

7.3.4. Weld Microstructure

The laboratory tests were performed on X100 gas-metal-arc welded plate, which was previously created to study the effects of hydrogen additions to argon shielding gas. To determine the effect of microstructure and residual stress on impedance, low frequency impedance measurements were performed at various locations as the sensor moved transverse to the weld. The transverse locations were spaced out every one-eighth of an inch, starting from the spot where the medium sensor was flush with the weld bead, as can be seen in Figure 7.9.

The weld microstructure and residual stress variations relative to hydrogen in base metal/HAZ/GMAW weld metal were assessed in both the laboratory and the field. The resolution of the sensor is limited in this case by the size of the medium u-core. Though the spacing of the transverse spots is 3.18 mm, the width of the medium u-core legs are 12.7 mm, meaning the impedance readings at each spot is an average of the volume that the induced magnetic flux penetrates in the material.

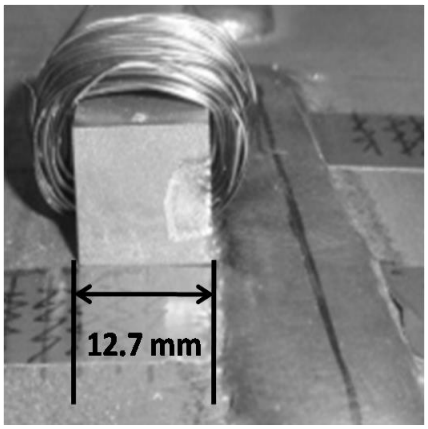

Figure 7.9. Lateral dimension of the medium u-cored sensor

7.3.5. Linepipe Coating Lift-off

Linepipe coatings increase sensor lift-off and therefore decrease the inductive coupling between the sensor and linepipe steel. The minimal thickness specified for FBE

coating is 14 mils (0.36 mm), although common applications range from 17 to 20 mils (0.43 to 0.51 mm).

7.3.6. Flux Leakage Effects

An experimental study was performed to assess the magnetic flux leakage effect of surface anomalies on linepipes. This study is based on results from the August 2008 field trip to Battelle Memorial Institute's Pipeline Simulation Facility in West Jefferson, Ohio, where colleagues from the Colorado School of Mines were measuring the remanent magnetic field on a test linepipe circuit. The field measurements were greatest near welds and valves that caused a leakage of flux. To study the effect of flux leakage on the field hydrogen sensor, a rectangular block was machined out of X100 linepipe steel. A weld stub or rivet was welded by GMAW in short-circuit mode with a 0.045-inch (1.14 mm) ER70S-6 electrode with 100% argon shield gas. The resulting rivet had a diameter of 0.075 inches (1.91 mm) and a height of 0.065 inches (1.65 mm). A complementary hole was drilled with a #47 drill bit resulting in a hole with a diameter of 0.078 inches (1.98 mm) and a depth of 0.065 inches (1.65 mm).

Two comparable sensors were fabricated with 30-gauge copper magnet wire on identical ferrite cores (μ_i = 5000). The impedance of the two sensors (Sensor A and Sensor B) at 200 Hz were identical within 0.153 percent as can be seen from Figure 7.10. Measurements of the rivet, hole, and unblemished steel surface were measured with (Sensor B) and without a permanent magnet yoke (Sensor A) at 20, 100, 200, 500, 1000, and 3000 Hz. The results show that sensors A and B have similar baseline impedances without the yoke. However, the baseline impedance for sensor B is dramatically reduced when coupled with the yoke.

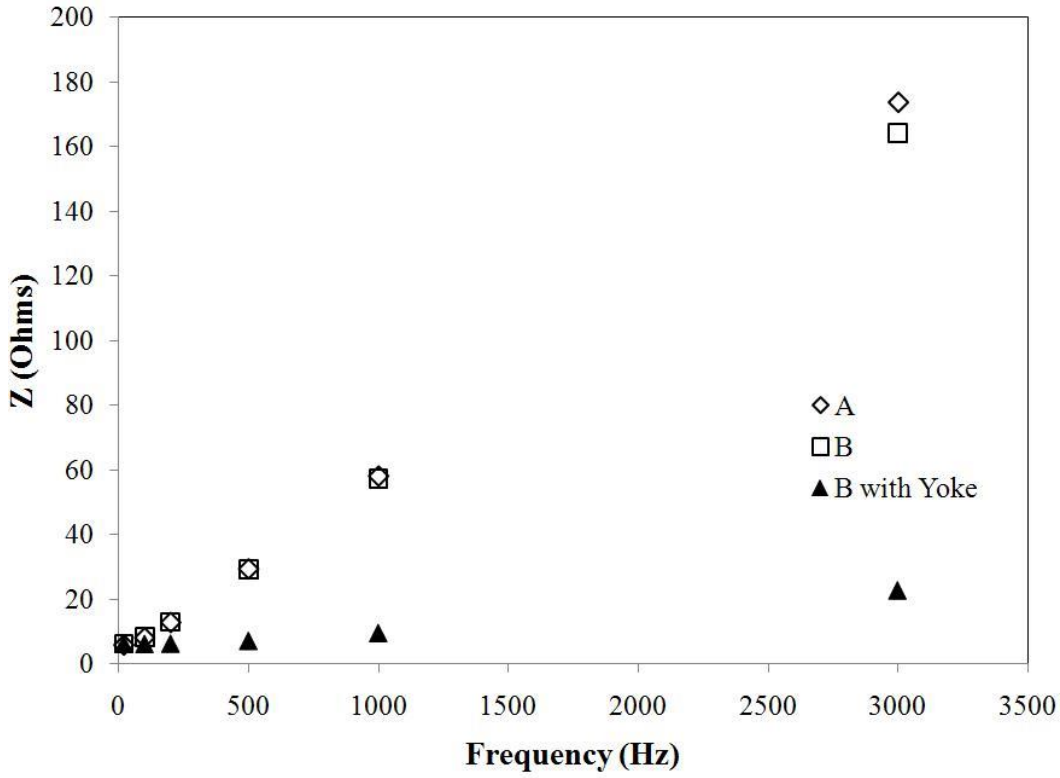

Figure 7.10. Baseline impedance of Sensors A and B as a function of frequency. Measurements made with the medium u-core sensor.

7.4. Coil Refinement

The results shown thus far have been from measurements taken with an air-cored coil. Soft magnet ferrite cores have high initial relative permeabilities (the initial slope of their hysteresis curves) from 1400 to 2300. A high relative permeability core material will result in a higher inductance and therefore a higher induced magnetic field, increasing the effectiveness of the hydrogen sensor coil.

7.4.1. Soft Ferrite Cores

The hydrogen sensor was further developed, resulting in increased sensitivity and decreased signal-to-noise ratio. Incorporation of MnZn ferrite U-shaped sensor cores with initial relative permeabilities higher than the cylindrical ferrite cores used for the Brooks coil described in the first annual report accomplished both of these goals. This new medium u-cored sensor is shown in Figure 7.11. Much of the data presented in this

report was acquired with this sensor. To improve sensor spatial resolution and standardize measurements between linepipes of various diameters, the sensor core geometry was redesigned.

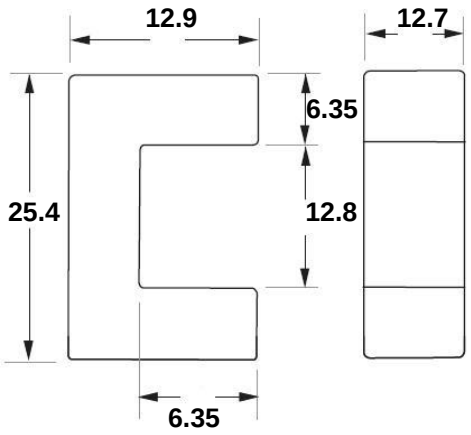

Figure 7.11. The medium ferrite u-core (dimensions in mm).

A sensor coil induces a magnetic field into a bulk volume of the material it senses. Therefore, the material response measured by a sensor coil is an additive response of the material contained within the bulk volume. To increase the spatial resolution of a sensor, it is necessary to narrow the lateral boundary dimension that defines this bulk volume. In addition, the rectangular footprint of the medium u-cored sensor leads to a variance in lift-off distance for varying linepipe radii of curvature. Weld bead crown morphology is another source of variance in lift-off distance between measurements on different linepipes.

As a solution to both issues, a new sensor ferrite core has been designed. It has been machined by Ceramic Magnetics, Inc. from their proprietary MnZn 60 ferrite material. The MnZn 60 material provides a higher magnetic permeability (6500) and Curie temperature (170 ºC) than the current ferrite core material (5000/140 ºC). The new design consists of a u-core with cylindrical legs with conical feet, shown in Figure 7.12. The conical tips of the new sensor result in an enhanced spatial resolution over the current sensor during transverse girth weld measurements. Enhanced spatial resolution is

critical in differentiating weld microstructures for hydrogen content assessment. In addition, the conical core legs will dramatically increase the flux density generated by the sensor on the surface of the linepipe by reducing the footprint area of the core. The pointed core legs provide flexibility in coupling with various linepipe curvatures while maintaining a constant lift-off. This new sensor design performed remarkably well compared to the medium u-core. A 44-in. (1.12 m) diameter X100 linepipe steel specimen was measured by each sensor core oriented both circumferentially and longitudinally. Any resulting impedance change between the two differently oriented measurements is attributed to variation in sensor core lift-off. The impedance change due to orientation (circumferential vs. longitudinal) was over 15 percent for the medium u-core. The conical-tipped core demonstrated a difference of roughly 0.1 percent. This design advantage is illustrated in Figure 7.13.

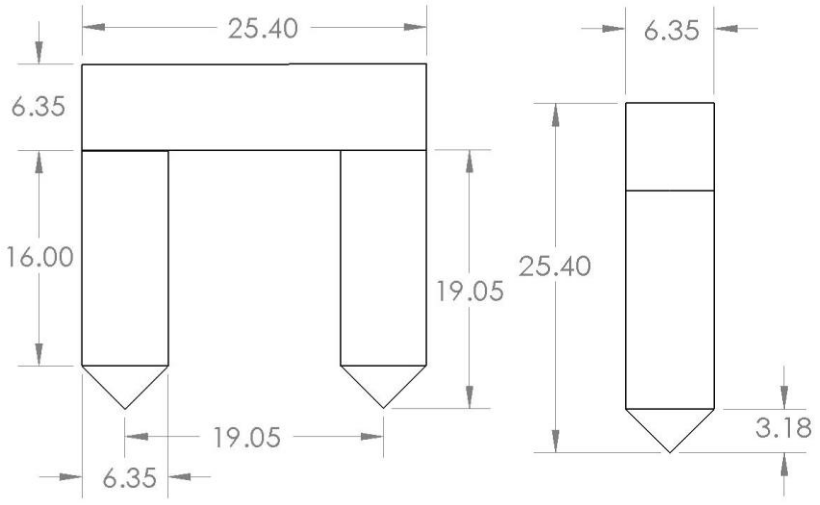

Figure 7.12. Newly designed conical-tipped core sensor (dimensions in mm**).**

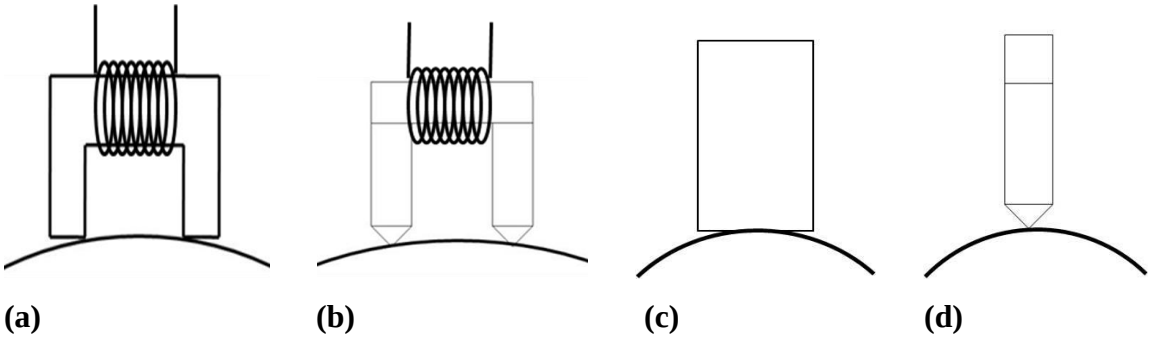

Figure 7.13. Circumferential orientation of (a) medium u-core and (b) conical-tipped core. Longitudinal orientation of (c) medium u-core and (d) conical-tipped core.

The conical-tipped sensor core standardized sensor lift-off for linepipes of various curvatures, however, the induction capacity of these sensor cores were less than the medium u-cores. The amount of magnetic field induced by a sensor core and therefore its overall sensitivity for measurement is determined by the bulk volume of ferrite used. Therefore, a revised core designed to be approximately four times bulkier than the conical-tipped sensor core has been designed. This pyramid-tipped sensor core will have all the benefits of the conical-tipped core with enhanced sensitivity. This newest sensor design is shown in Figure 7.14.

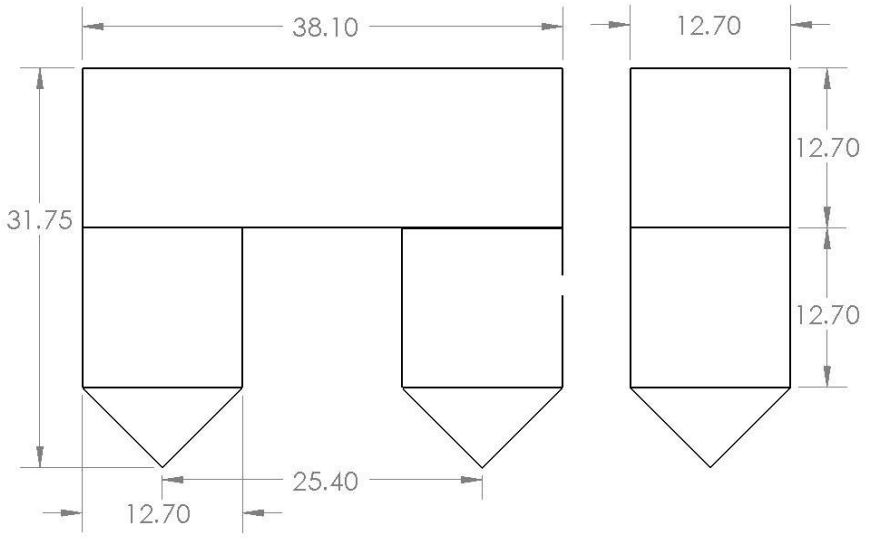

Figure 7.14. Pyramid-tipped core sensor (dimensions in mm**).**

7.5. Sensor Cart

An automated sensor cart was built for controlled, incremental measurements of the linepipe surface. This cart advances the capability of the prototype field sensor to resolve linear regions of the weld microstructure with a resolution of 0.00875 inches (0.22 mm) per step. This accomplishment represents a fourteen-fold increase of scanning resolution over previously reported transverse weld impedance data and a means to standardize lift-off for sensor comparison studies. A picture of the cart is shown in Figure 7.15 (a). The cart is powered by a stepper motor. A LabVIEW module was written to control the stepper motor and monitor the position of the sensor cart. This module was seamlessly integrated into the data acquisition system program currently used for the sensor.

The sensor is mounted below the front axle of the cart, as can be seen in Figure 7.15 (b). Figure 7.16 illustrates the lift-off required for the sensor to clear the crown of a weld bead on the pipe. As the front tires roll over the weld bead, the sensor lifts with the front axle, maintaining constant lift-off. The sensor lift-off with this design was too large, so this design was abandoned.

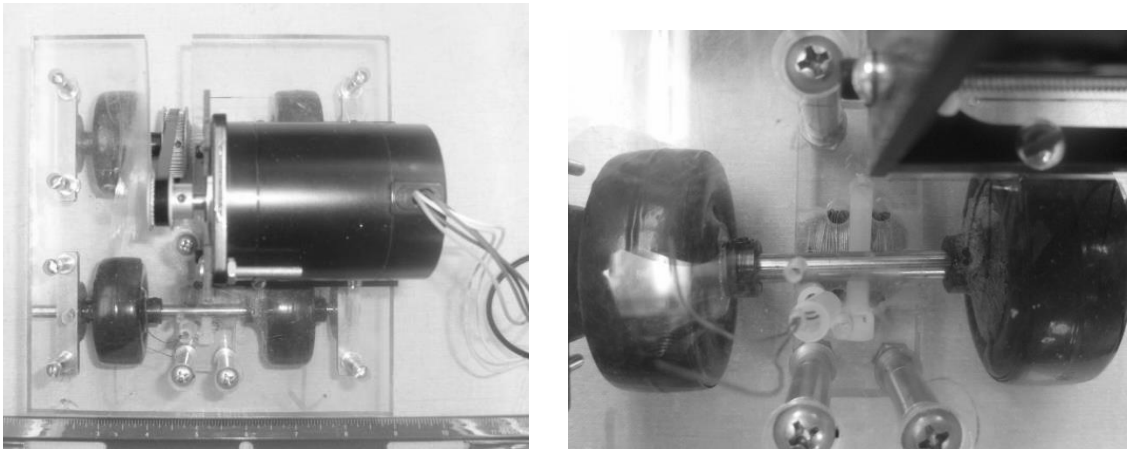

(a) (b)

Figure 7.15. (a) Top view of the sensor cart (b) top view of front axle

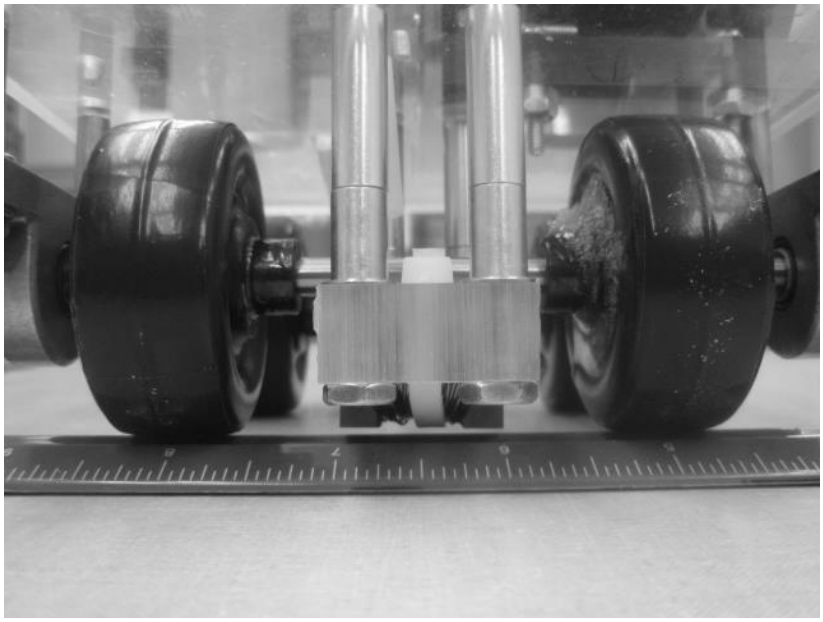

Figure 7.16. Front view of sensor and front axle showing lift-off

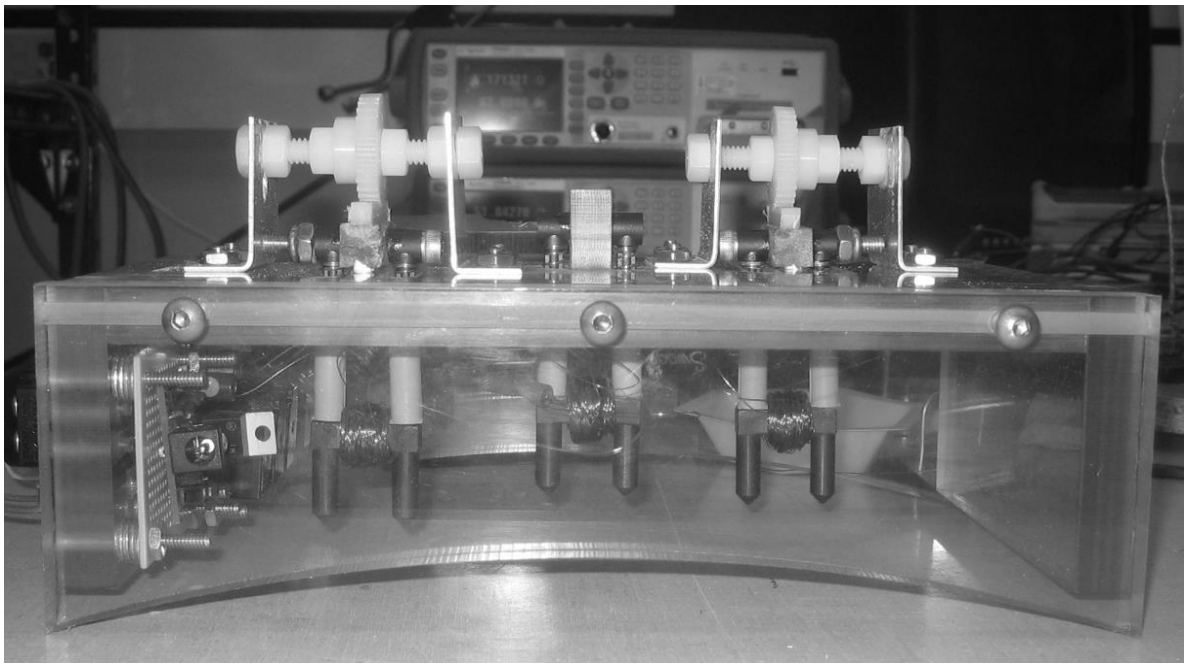

Figure 7.17. Side view of the field sensor array.

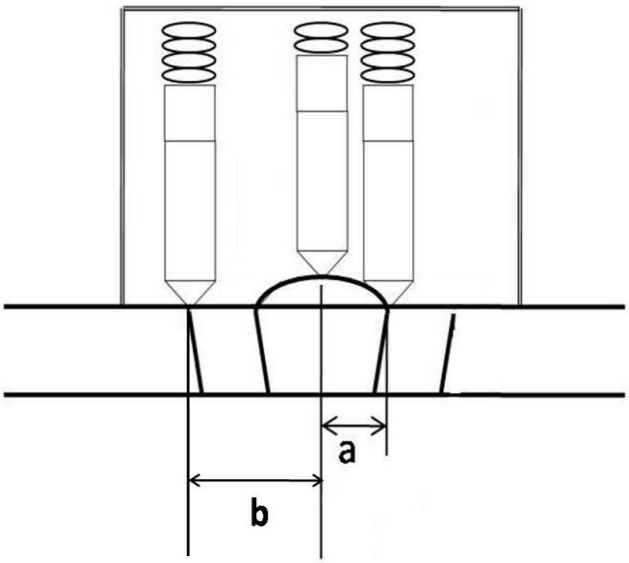

Figure 7.18. A front view of the field sensor array measurement of a girth weld. The sensors will be individually spring-loaded. The weld bead centerline-to-fusion line distance (a) and centerline-to-HAZ/BM boundary distance (b) will be adjustable.

7.6. Field Sensor Array

This design addressed the excessive lift-off of the sensor cart by incorporating spring-loaded sensors that couple directly to the linepipe coating surface. A field sensor array implementing the newly designed sensor cores is being engineered and built. A side view of the array is pictured in Figure 7.17. The array layout will be determined to avoid inductive coupling of the individual sensors. The lateral spacing (dimensions a and b) of the sensors will be field adjustable, based on the microstructural mapping results of the flux leakage signal according to the collaboration scheme shown in Figure 7.18. The center sensor will be centered on the weld bead crown, the left sensor will be near the HAZ/BM line, and the right sensor will be located near the fusion line. The measurements taken with the three individual sensors in the field sensor array will be controlled by the LabVIEW DAQ system. Measurements will be taken from a single sensor at a time. Each sensor has an electromagnetic relay that will make the connection to the LCR meter for measurements. The relay control is provided by the IC driver chip that houses multiple relay drivers. For example, the DAQ program will activate relay driver 1, the LCR data will be acquired from sensor 1, then the DAQ will deactivate driver 1 and activate driver 2. A schematic of the control system for the field sensor array is depicted in Figure 7.19. The removable sides of the box fit the linepipe curvature; the sides shown are for a 30-in. (762 mm) diameter pipe. This design prototype will work for pipes with diameters greater than 12 inches.

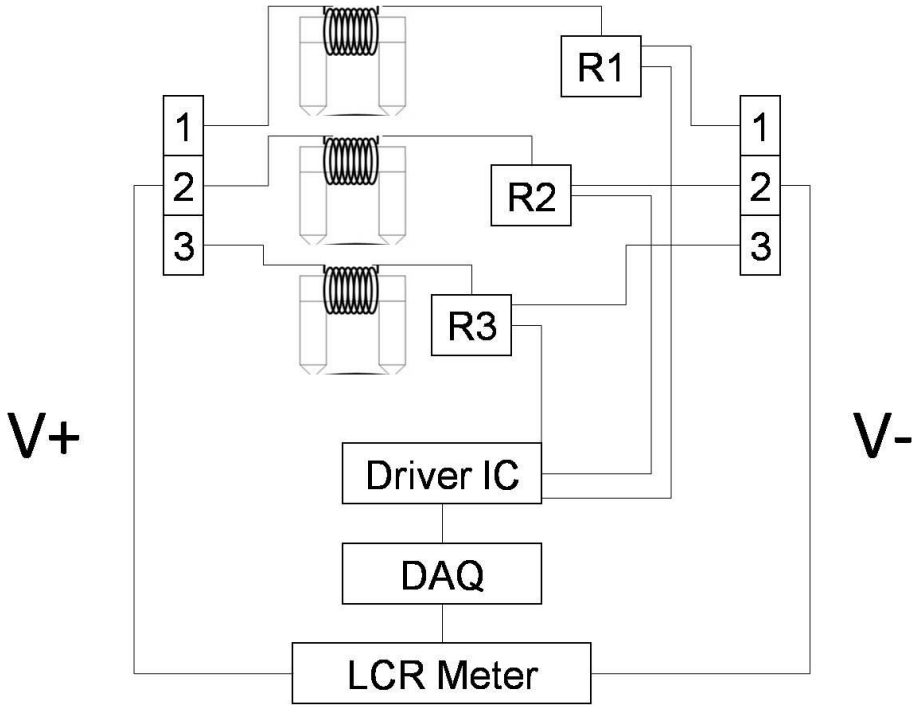

Figure 7.19. Schematic of field sensor array circuit.

CHAPTER 8 EXPERIMENTAL RESULTS AND DISCUSSION

Chapter 7 reviews all of the technical and engineering principles used in the development of the nondestructive, non-contact hydrogen detection in thick-walled coated linepipe steel. This chapter reports the qualitative assessment of hydrogen content in a coated field specimen.

8.1. Varying Weld Bead Microstructure

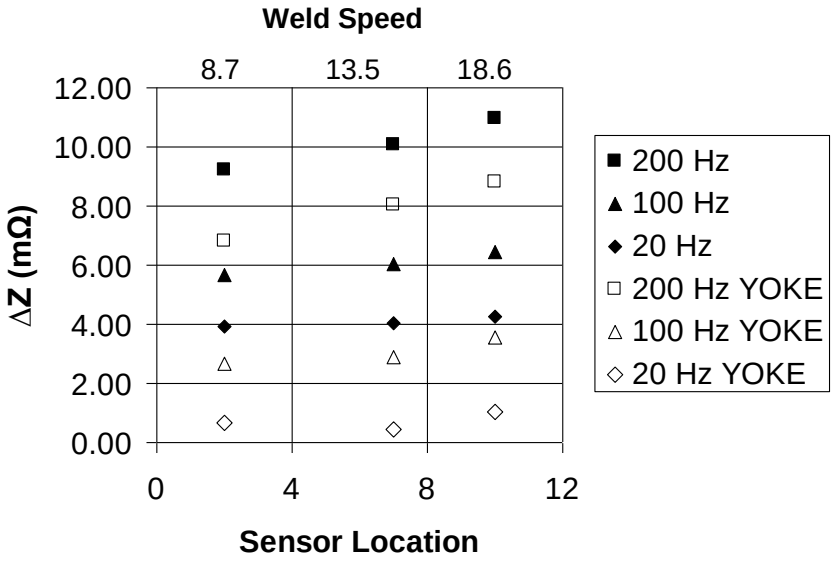

Figure 8.1. Low frequency impedance measurements of different GMA weld microstructures on X100 linepipe steel due to varying weld travel speed and the use of a magnetic yoke.

Low frequency impedance measurements taken for this weld microstructure study are shown in Figure 8.1, for both yoked and unyoked sensor coils. The results reported in Figure 8.1 indicate the attenuation effect of the permanent magnetic yoke on the weld impedance measurements. This arrangement is a desirable tool to aid the detection of low concentrations of hydrogen. From the results depicted in Figure 8.1, it appears that the 200 Hz signal is most sensitive to the weld microstructure differences due to varying the weld travel speed.

8.2. Varying Shielding Gas Content

The comparison of these three welds is shown in Figure 8.2. The data starts approximately four and a half minutes post-weld. A subsequent verification of these results is shown in Figure 8.4.

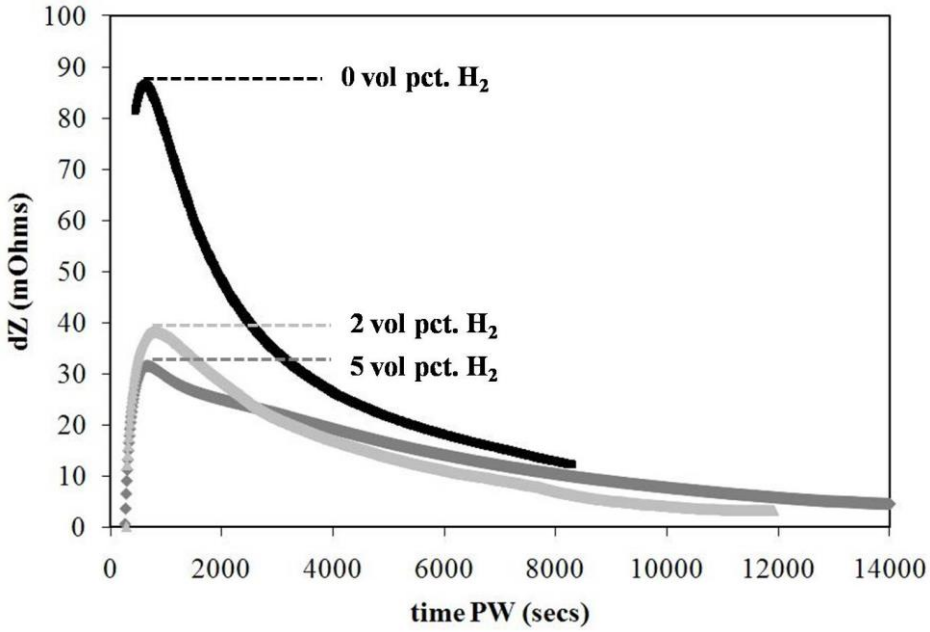

Figure 8.2. Initial X100 steel GMA weld comparison varying shield gas composition at 200 Hz [85].

During the verification of the initial results shown in Figure 7.3, the weld with 5 percent hydrogen and 95 percent argon in the shielding gas was full of gas bubbles. It is likely that the welding contact tip to base metal distance exceeded the 1-inch (25.4 mm) standard used for the previous welds. This increased distance likely resulted in an inadequate shielding of the arc.

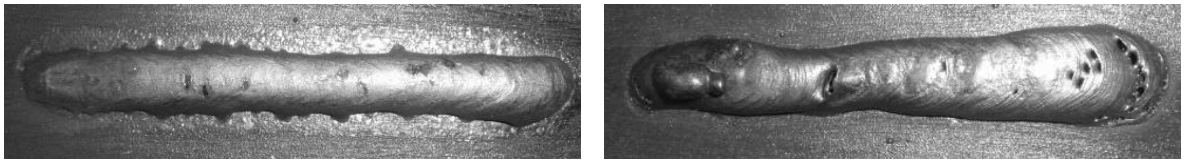

Figure 8.3. Pictures of follow-up GMA weld comparison of X100 steel with (*left*) 0 pct. hydrogen and (*right*) 5 pct. hydrogen / 95 pct. argon.

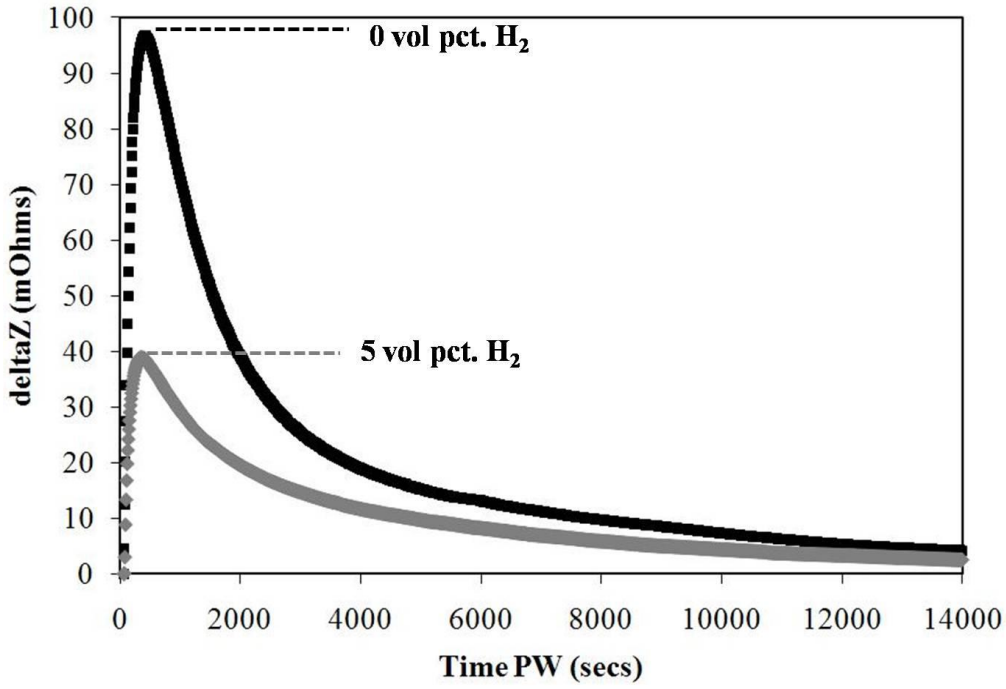

Figure 8.4. Verification of GMA weld comparison on X100 linepipe steel at 200 Hz.

The determination of the magnitude of impedance change due to hydrogen as it diffuses out of the steel weldment is valuable data for calibration. The maximum impedance difference between zero and five percent hydrogen GMA welds was around 55 mOhms. However, the impedance scatter due to varying the weld travel speed and subsequently varying the weld bead microstructure (from Figure 7.1) was around 2 mOhms. A piece of valuable information from this study was the magnitude of impedance change due to varying hydrogen content of the shielding gas. The maximum impedance difference between 0 vol. pct. hydrogen and 5 vol. pct. hydrogen GMA welds was around 55 mΩ. However, the impedance scatter due to varying the weld travel speed

and subsequently varying the weld bead microstructure was at most 2 mΩ. This result underlies the pronounced differences between the signature impedances due to microstructure and hydrogen content.

The signal peak decay with increasing hydrogen shield gas content in Figure 8.2 is an indication of thermionic desorption of hydrogen. In a DCEP GMA welding process, as depicted in Figure 8.5, the electrode is the anode while the weld pool cathode is where the positively charged hydrogen ions from the shield gas accumulate. Therefore, for DCEP GMA welds, the hydrogen content of the weld bead increases with shield gas hydrogen content. The weld bead hydrogen desorbs from the weld bead, extracting the heat of formation required to from diatomic hydrogen gas from the weld metal. The typical weld bead temperature profile is given by the 0 pct. hydrogen data in Figures 8.2 and 8.4. The difference in peak values of the 2 and 5 vol. pct. hydrogen data in Figure 8.2 illustrates the thermionic desorption cooling effect on the peak weld bead temperature. Hydrogen additions to argon shielding gas increase the arc temperature and therefore the weld bead temperature. Therefore, there are two thermal effects measured by the hydrogen sensor and reported in Figure 8.2. The 2 and 5 vol. pct. hydrogen welds have higher weld bead temperatures due to hotter arcs which would result in improved kinetics for hydrogen diffusion and desorption. The 5 vol. pct. hydrogen peak is the lowest because it had the highest hydrogen content in the weld bead.

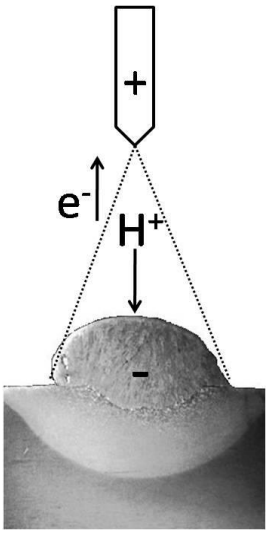

Figure 8.5. Schematic of DCEP GMA welding process.

8.3. Weld Microstructure

Laboratory tests were performed on gas-metal-arc welded beads on X100 linepipe steel plate, with different shield gas compositions. The two shield gases studied were industrial grade argon and 95 vol. pct. argon with 5 vol. pct. hydrogen addition. To determine the effect of microstructure and residual stress on impedance, low frequency impedance measurements were performed at various locations transverse to the weld centerline with a ferrite u-cored sensor. The results shown in Figure 8.6 reflect the variances in residual stress for the different regions encountered transverse to the weld bead: weld metal, HAZ, and base metal. The weld made with hydrogen addition in the shielding gas result in consistently higher impedances than the weld made with pure argon shielding gas.

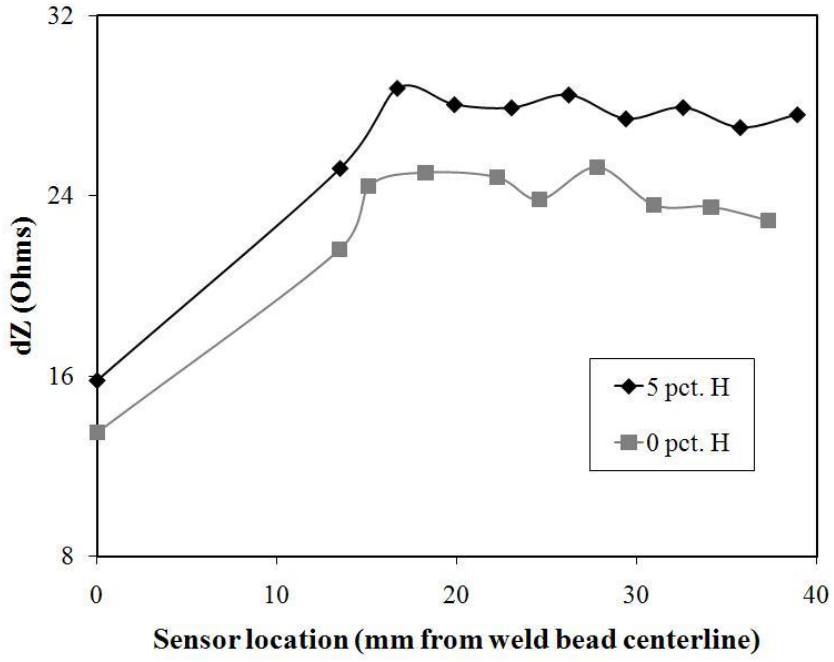

Figure 8.6. Transverse impedance laboratory results on uncoated X100 linepipe steel GMA welding welds [84].

Overall the significance in the results in Figure 8.6 are important to show the sensitivity that can be achieved if necessary, but they are also important for calibration and standardization of the hydrogen sensor for welding residual stress. The data

presented in Figure 8.6 quantifies the impedance change due to weld microstructure variance from weld metal to HAZ as roughly nine to ten Ohms for the uncoated X100 linepipe steel laboratory specimens.

Transverse weld impedance measurements made with the pyramid-tipped core are shown in Figure 8.7. These welds are identical to the welds shown in Figure 7.8. Figure 8.7 shows the pronounced spike in impedance due to differences in both microstructure and trapped hydrogen content at the fusion line for all three welds. The fusion line peak for the 5 vol. pct. H weld is larger than the other two. A noticeable improvement in the results from Figure 8.7 over Figure 8.6 is the weld bead impedance trend. These welds have a marked topological difference in the weld bead crowns, resulting in pronounced lift-off variations with the medium sensor core used to measure the results shown in Figure 8.6. Lift-off variability can therefore be removed from the pyramid-tipped sensor core weld bead data shown in Figure 8.7; the weld bead impedance values reflect microstructure and hydrogen content. The ordering of the weld bead impedance data increasing from 0 pct. H to 5 pct. H to 2 pct. H could reflect differences in absorbed and subsequent trapped hydrogen content distribution for the different shield gas compositions. The 5 pct. H weld would have had a higher disassociated monatomic hydrogen concentration, which has been shown to have a higher incidence of absorption towards the edge of the weld bead [5]. This higher monatomic concentration could lead to a higher fusion line concentration while a higher diatomic concentration in the 2 pct. H weld would lead to a higher weld bead hydrogen concentration, as shown by the data in Figure 8.7. The general trend of transverse weld microstructure is verified by Yamaoka's Vickers hardness data shown in Figure 8.8.

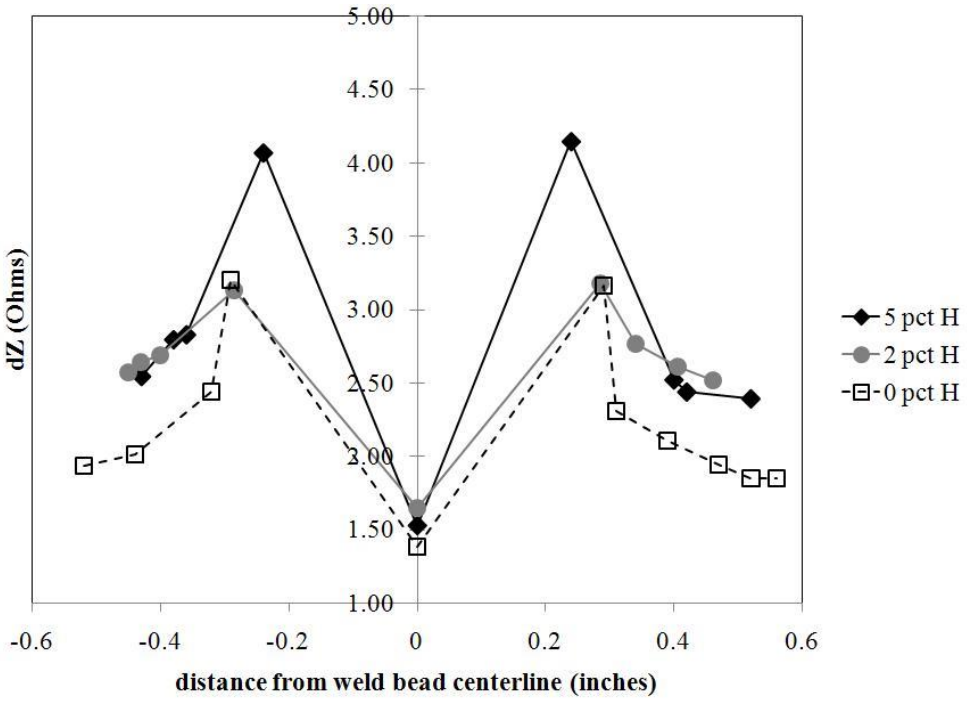

Figure 8.7. Transverse weld impedance measured with pyramid-tipped core on GMA welded bead-on-plate welds with varying shield gas hydrogen content.

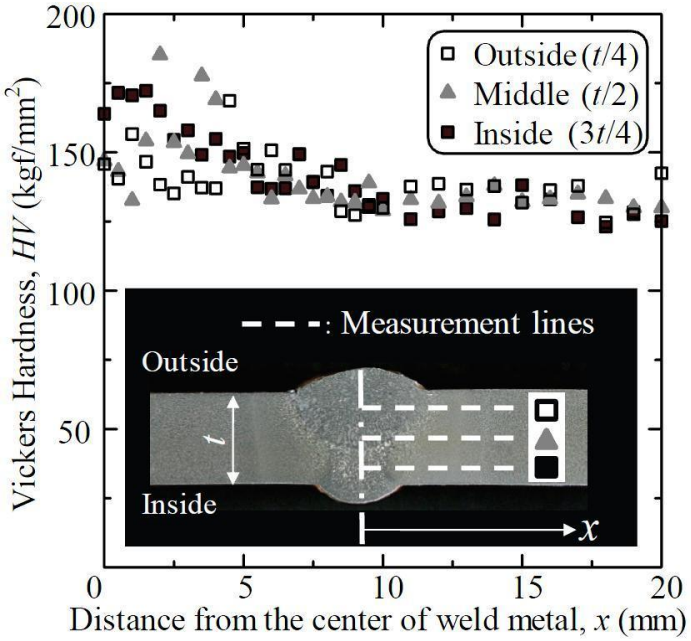

Figure 8.8. Transverse weld Vickers hardness profile [86].

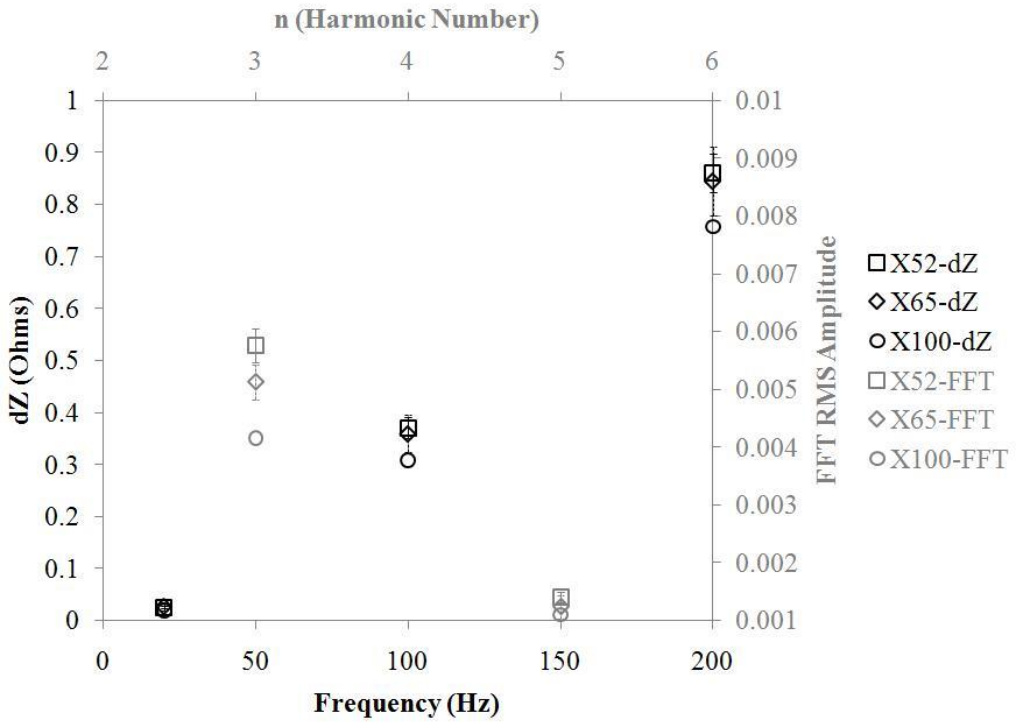

Figure 8.9. Comparison of low frequency impedance (left and bottom axes in black) and FFT harmonic analysis of induced voltage (top and right axes in gray) for X52, X65 and X100 linepipe steels.

Results for pipeline steel classification sorting for both low frequency impedance and FFT harmonic analysis are shown in Figure 8.9. Three different samples of X52 and X65 linepipe steel were sampled, resulting in a standard deviation of classification type (X52 or X65), while only one sample of X100 linepipe steel was measured. All of the samples had identical geometry. Figure 8.9 depicts a scatter in both impedance change (dZ) and FFT harmonic analysis of the sensing coil voltage for these three different pipeline steel classifications. The third harmonic and the 200 Hz impedance signal yielded the most distinct results with the least amount of scatter. This result shows the promise of the sensitivity of harmonic analysis to hydrogen content. FFT analysis of the sensing coil might better distinguish between different hydrogen content levels than low frequency impedance. Hydrogen charging experiments will bear out this hypothesis.

8.4. Linepipe Coating Lift-off

Figure 8.10 shows that coating thicknesses of 20- and 40-mil attenuate the impedance to roughly 40 and 30 percent of the uncoated value. Therefore, readings made through a 20-mil coating can be multiplied by a correction factor of 2.5 to convert to a comparable uncoated reading. A field assessment of the effect of coating lift-off due to a transverse weld microstructure impedance survey was performed on a 20-mil fusion-bonded epoxy coated X65 linepipe steel. Figure 8.11 depicts the comparison of a coated X65 SAW weld to the uncoated X100 GMA welding welds showing similar impedance signature signals due to transverse weld microstructure. The coated four Ohm transverse weld microstructure signal scales directly to the ten Ohm uncoated transverse weld microstructure signal shown in Figure 8.11, verifying the 2.5 20-mil coating correction factor.

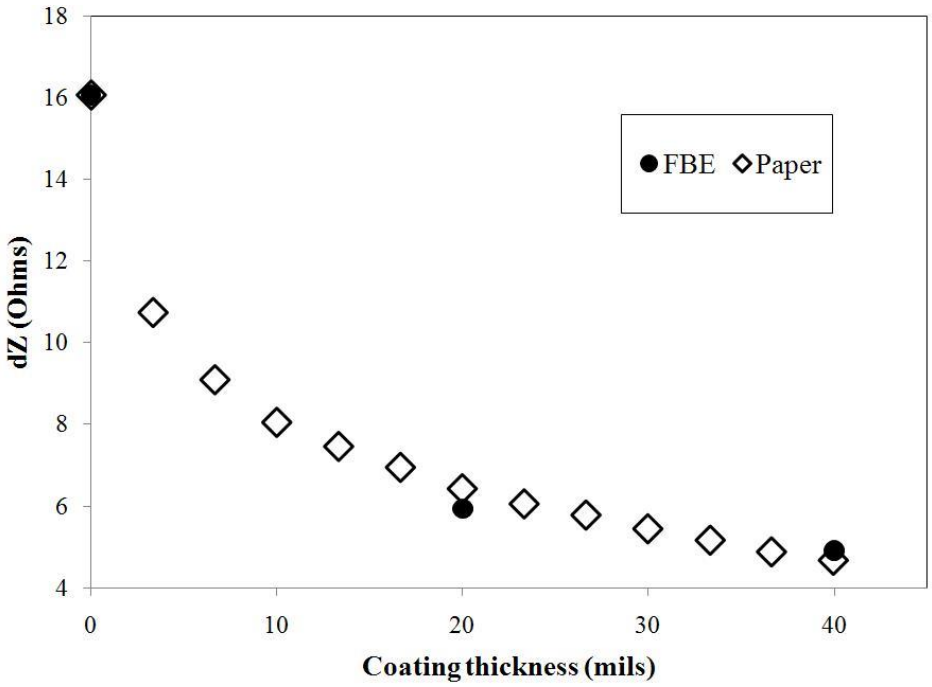

Figure 8.10. Lift-off effect on medium u-core sensor for FBE coated and paper coated X100 linepipe steel base metal [84].

These results show the importance of an in-field coating thickness assessment, made with an eddy current unit, in conjunction with impedance measurements to assess hydrogen content.

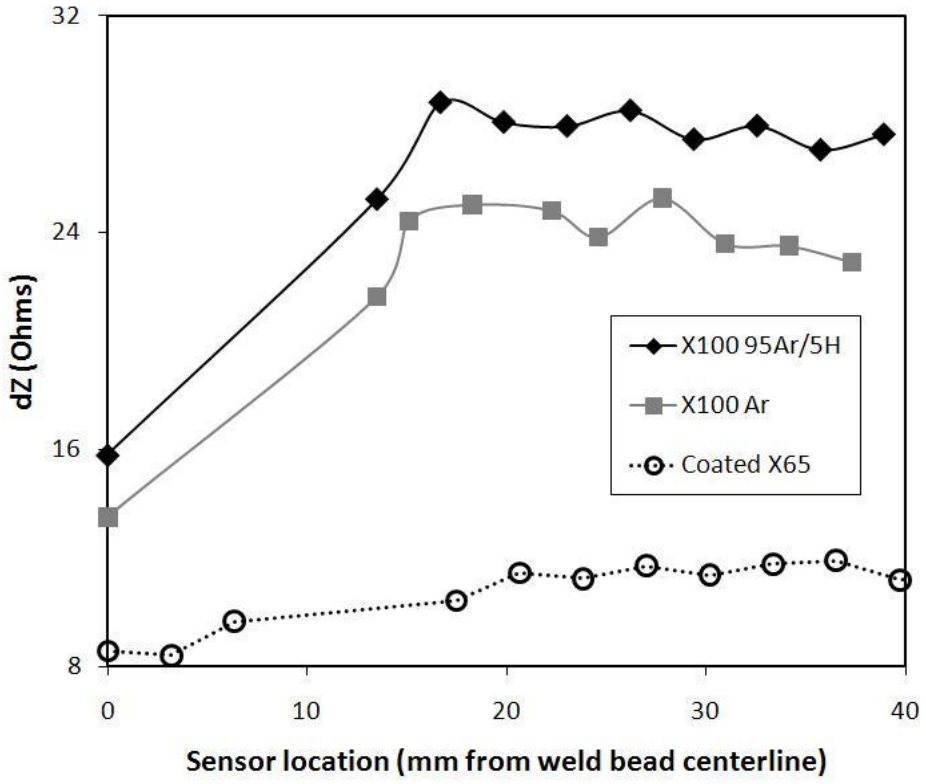

Figure 8.11. Transverse impedance laboratory results on uncoated X100 linepipe steel GMAW welds and field result on a coated X65 linepipe steel SAW weld [84].

8.5. Field Testing

To calibrate the sensor for magnetic remanence in the linepipe due to magnetic flux leakage (MFL) pigging, field measurements were performed at Battelle Memorial Institute's Linepipe Simulation Facility in West Jefferson, Ohio. Low frequency impedance measurements were performed before, during, and after smart pigging of a previously unpigged, extruded and coated X65 linepipe steel. This event was an invaluable opportunity to calibrate the sensor for the simultaneous effects of coating lift-

off and magnetic remanence. There were no welds on this extruded linepipe section to measure transverse weld microstructure. The pipe was pigged in one direction for five runs. The average impedance of five spots is plotted for each pig pull, however the data for pig pull four was corrupted. It can be seen from the data in Figure 8.12 that a remanence level change from 0 to 4500 Gauss resulted in a small change in impedance of roughly 1.5 Ohms. This impedance change is due to the immediate effect of magnetization of the coated linepipe.

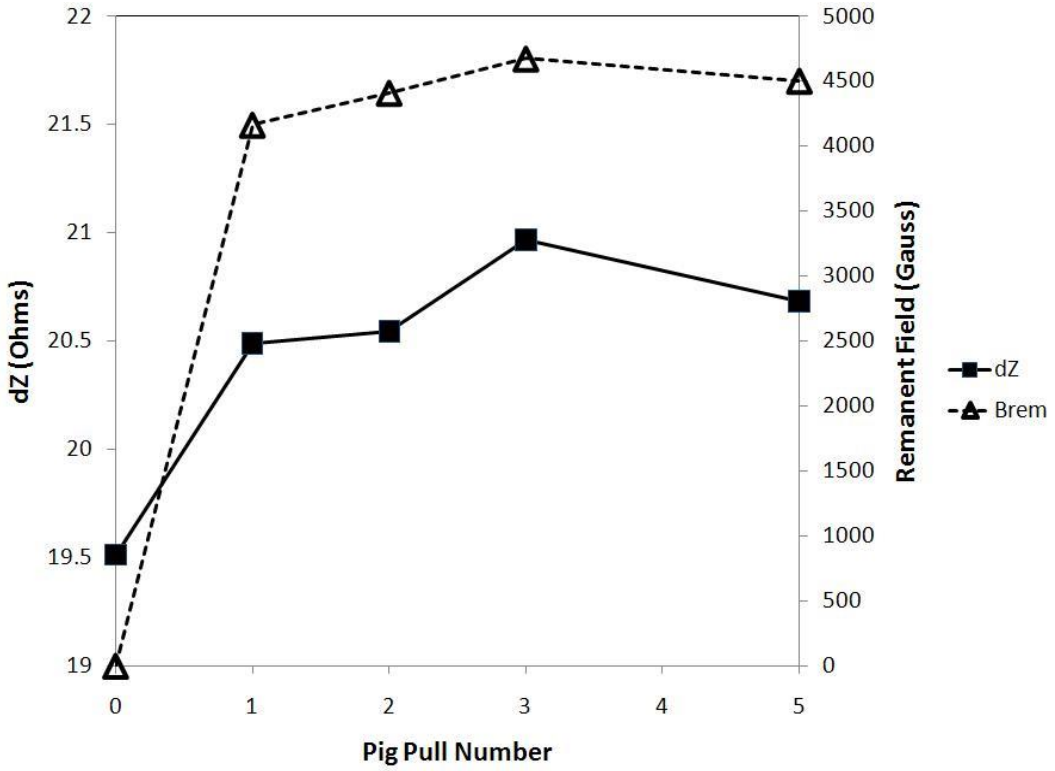

Figure 8.12. Effect of magnetic remanence on X65 linepipe steel. Test performed on previously unpigged extruded linepipe at Battelle Memorial Institute's Linepipe Simulation Facility.

A second field trip was taken to the Battelle Memorial Institute's Linepipe Simulation Facility in West Jefferson, Ohio on March 9, 2009 to reevaluate the modern extruded X65 steel linepipe reported in Figure 8.12. A strong correlation between the

hydrogen sensor impedance signal and leakage flux was observed near a girth weld joining two extruded and coated X65 steel linepipes identical to the pipe reported in Figure 8.12. Therefore, a fabricated flux leakage source is not necessary for hydrogen sensor measurements on a weld. The spike in leakage flux is believed to be attributed to microstructural differences at the boundary between the heat affected zone and the base linepipe metal due to this 0.75 inch (19.1 mm) wide girth weld. In future field tests, flux leakage can be used as a weld microstructure survey tool based on Figure 8.13. The HAZ/BM boundary can be located by flux leakage prior to hydrogen content assessment of the weld with the hydrogen sensor. HAZ/BM boundary flux leakage detection will expedite the hydrogen content assessment process by specifying the region of highest hydrogen concentration (see Figures 2.15 and 4.2) for coated linepipe steel.

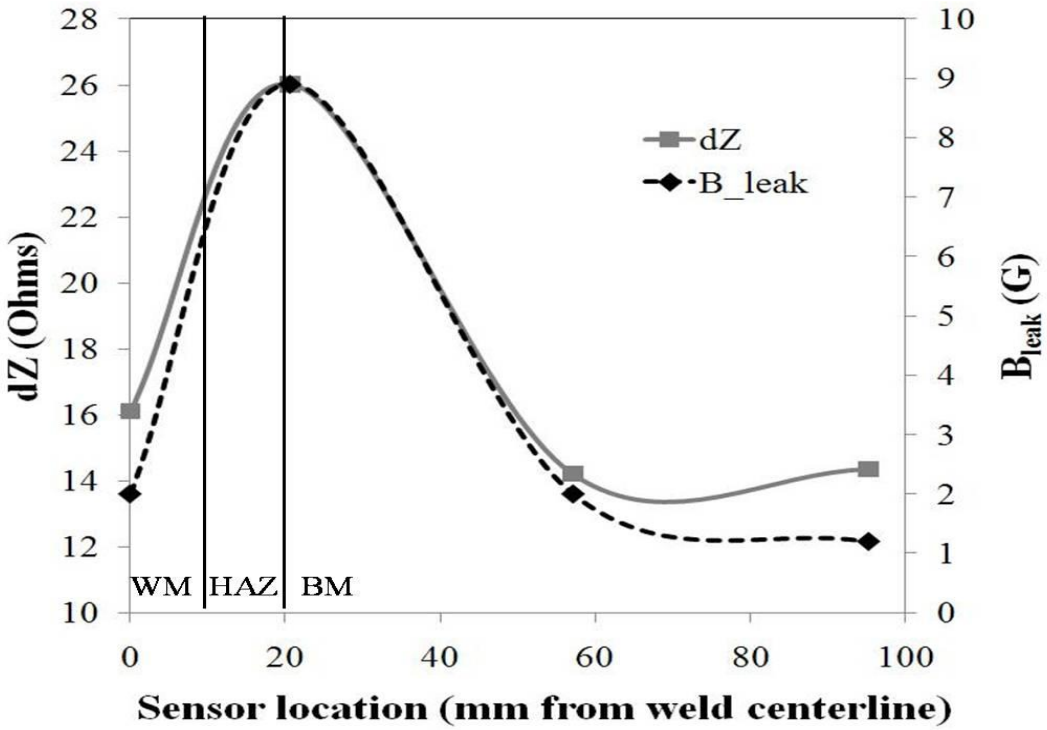

Figure 8.13. Simultaneous plot of normalized impedance change at 200 Hz for an X65 linepipe steel girth weld measured through a coating and detected flux leakage transverse to the pipe as a function of distance from the centerline of the girth weld bead [84].

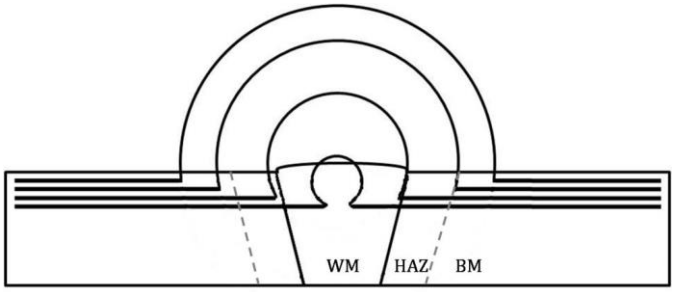

Figure 8.14. Cross-section schematic of flux leakage of a girth weld bead.

Figure 8.14 is a schematic of the flux leakage field detected in Figure 8.13. Figure 8.13 conclusively shows that the microstructure associated with the girth weld can be sensed both by flux leakage and low frequency impedance. The uniformity of weld bead size, welding heat input, and other parameters of welds made in the field make this assessment of weld microstructure valuable and relevant to field measurements. In future field testing on in-service linepipes where hydrogen is present, flux leakage can be used to specify the weld HAZ region to be inspected by the hydrogen impedance sensor.

8.6. Hydrogen Content Assessment

There are four impedance measurement variables to be considered in the signal reported in Figure 8.13: magnetic remanence level, coating thickness, weld microstructure, and hydrogen content. The spike in leakage flux is believed to be attributed to microstructural differences at the boundary between the heat affected zone and the base linepipe metal due to this 0.75 inch (19.1 mm) wide girth weld. The remanent field level in these two welded sections is the same order of magnitude as that of the single section of linepipe shown in Figure 8.12.

The impedance data presented in Figure 8.13 is proportionate to the level of flux leakage and therefore the level of magnetic remanence in the linepipe, also seen in the data from Figure 8.11. There is a striking difference between the two data sets in the magnitude of impedance change due to the change in magnetic remanence. The leakage flux around a girth weld will be tens or hundreds of Gauss greater than the base metal,

much less than the 4500 Gauss effect calibrated against in Figure 8.11. However, the change in remanence from roughly 0 to 4500 Gauss corresponded to only a 1.5 Ohm impedance increase, as reported in Figure 8.12. Therefore, the effect of magnetic remanence does not explain the impedance change of roughly 10 Ohms between weld metal and HAZ (from sensor location 0 mm to 20 mm) as seen in Figure 8.13.

Figure 8.15 is a plot of the impedance data from Figure 8.13 plotted with the longitudinal weld on the coated X65 steel linepipe shown in Figure 8.11. Figure 8.11 shows the impedance data from two 20-mil coated welds measured in the field. The X65 steel linepipe transverse weld microstructure impedance signal shown is for a known hydrogen content range from 1 to 2 ppm. Based on the magnitude of the signature impedance signals from the measurement variables presented in Table 8.1, the peak signal in the Battelle Memorial Institute's Linepipe Simulation Facility data plotted in Figure 8.15 could possibly be due to hydrogen content in excess of 1 to 2 ppm. This hydrogen content level can be explained by the effect of a remnant magnetic field on hydrogen ingress in addition to the rusting linepipe (the coating spalled) acting as a source of hydrogen through the iron-water reaction.

The correlation of impedance to leakage field in Figure 8.9 is explained by this effect. The location where the leakage field is highest corresponds to the area where hydrogen ingress is greatest. The peak impedance signal shown in Figures 8.11 and 8.13 is most likely due to accumulated hydrogen pickup into a steel linepipe with a high remanence field over a period of several years.

The results presented in this chapter and Chapter 7 constitute the successful proof of concept and initial calibration efforts for a nondestructive non-contact hydrogen sensor.

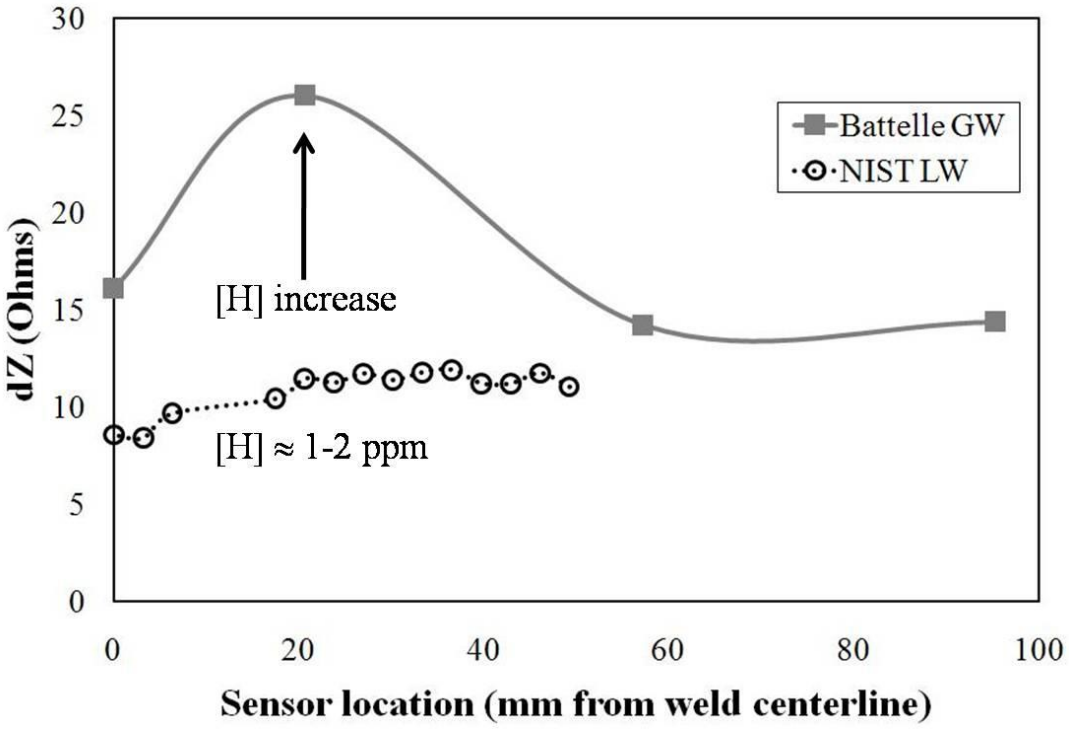

Figure 8.15. Comparison of 20-mil FBE coated X65 steel linepipe transverse weld impedance studies made in the field. Results shown for a girth weld at Battelle Memorial Institute's Linepipe Simulation Facility and a longitudinal weld at NIST-Boulder [84].

Table 8.1. Impedance signatures for hydrogen sensor variables.

Parameter	**Change in Parameter**	**Signature Impedance Change**
Magnetic Remanence	4500 Gauss	~ 1.5 Ohms
Coating Thickness	20 mil (0.51 mm)	~ 60% decrease
	40 mil (1.0 mm)	~ 70% decrease
20-mil Coated Linepipe Transverse Weld Microstructure	WM to HAZ	~ 4 Ohms
Uncoated Linepipe Transverse Weld Microstructure	WM to HAZ	~ 10 Ohms

CHAPTER 9 IN-SITU HYDROGEN FATIGUE TESTING

Building a nondestructive hydrogen sensor to be used during in-situ mechanical testing creates many more variables than a static situation, so it is necessary to determine all of the variables and to separate them. Many of the variables will be dependent on the final chamber and specimen design for fatigue testing. A literature review has been performed on the effects of hydrogen on fatigue crack growth rate behavior. The data found was used to determine optimum fatigue testing conditions to best understand the role of hydrogen under fatigue in pipeline steel.

9.1. Fatigue Crack Growth Rate Testing

There are basically two approaches for determining the role of hydrogen on fatigue crack growth rate (FCGR) behavior. The first approach measures the susceptibility to hydrogen embrittlement by measuring the difference in the FCGR in hydrogen charged and uncharged steel specimens at a defined stress intensity factor range, ΔK. The second approach measures the change in the slope of fatigue crack growth rate as a function of stress intensity range near the threshold region. The second approach will be used in this investigation.

The fatigue crack growth rate (i.e., da/dN) of materials depends of the maximum stress intensity factor (K_{max}), minimum stress intensity factor (K_{min}), stress intensity factor range ($\Delta K = K_{max} - K_{min}$), stress ratio ($R = K_{min} / K_{max}$), and cyclic frequency. The most common way to estimate fatigue crack growth is to employ a linear-elastic fatigue-crack-growth model based on the "Paris Law" relationship:

$$\frac{da}{dN} = C(\Delta K)^m \tag{9.1}$$

where da/dN (mm/cycle) is the increment of crack growth per cycle, C (mm/cycle; MPa·mm$^{1/2}$) and m (no units) are the material properties, and ΔK (MPa·mm$^{1/2}$) is the stress intensity factor range. A vast amount of FCGR data exists in the open literature [87, 88, 89].

The influence of hydrogen on fatigue crack growth rate in steels has mostly been studied using low cycle fatigue loading [90, 91, 92]. It is has been commonly assumed that hydrogen is not detrimental in the fast cycle alternate stress testing in the elastic range [93]. The rationale for this assumption is based on the observation that characteristic times for hydrogen to accumulate at a crack tip under a favorable stress gradient are large compared to typical fatigue machine cycle periods. Thus, in a typical loading cycle sufficient hydrogen cannot accumulate at the crack tip quickly enough to allow for material damage hence the need for in-situ hydrogen fatigue testing. The role of hydrogen in the specimen during in-situ hydrogen fatigue testing is not yet understood either. The mechanical metallurgist truly needs a quantified map of hydrogen content in the steel fatigue specimen. The low frequency impedance hydrogen sensor will be used to monitor the hydrogen content in the fatigue specimen during fatigue testing.

To monitor hydrogen content during fatigue via low frequency impedance requires strict variable separation. Prior to the completion of the new in-situ hydrogen testing facility at NIST-Boulder, preliminary hydrogen fatigue experiments proceeded to gain valuable information before in-situ testing. Preliminary fatigue experiments are performed in air on hydrogen charged samples. In the future, fatigue tests will be conducted in a hydrogen environment so that there will be no hydrogen losses at the crack-tip. So for preliminary fatigue testing, specimens are pre-charged with high-pressure gaseous hydrogen for 1200 hours (50 days) at 100^{o}C and a pressure of 1000 psig (6.83 MPa). The total achieved saturated hydrogen content (measured using a gas chromatograph) in the steel specimen was approximately 38 ppm. Immediately after hydrogen charging, the specimens are coated with tin to maintain the hydrogen in the specimen as hydrogen diffuses out of pipeline steel within seconds. (Aside: There are multiple coating or poisoning techniques that can be used to trap hydrogen within the specimen. For these experiments, different commonly used barrier coatings (cadmium, nickel, etc.) were compared for hydrogen charged specimens as a function of time to determine minimum hydrogen loss. Tin proved to be the most effective barrier as a function of time.) During the specimen's transportation, from the hydrogen charging facilities to the fatigue test facilities, the tinned specimens were also submerged in liquid

nitrogen (LN_2) for extra protection from hydrogen diffusion (in the case that the coating has holidays (imperfections)).

The first step in building the hydrogen sensor is to understand the role hydrogen plays in preliminary fatigue experiments. For example, how long will hydrogen remain at the crack tip? Knowing the time it takes for hydrogen to diffuse out of the specimen will allow separation of the actual residual stress in the specimen due to fatigue versus hydrogen. It is important to know which effect is which.

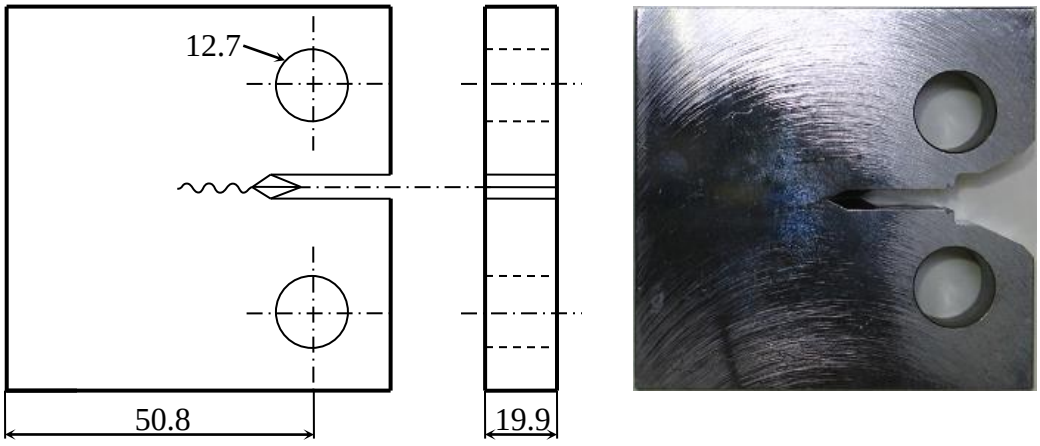

Figure 9.1. C(T) specimen dimensions (in mm).

Preliminary fatigue crack growth rate experiments were performed to understand the role of hydrogen during testing in air (prior to completion of in-situ facility). The frequency of fatigue crack growth testing under hydrogen influence was set at a frequency of one Hertz, while the fatigue crack growth, before hydrogen charging, was set at a frequency of ten Hertz in order to have a faster test running time (only the last millimeter of the pre-cracking was performed at a frequency of one Hertz in order to have a continuing fatigue process). FCGR tests were conducted on compact tension specimens (C(T), as defined in ASTM E647-05 [5]) machined from the longitudinal orientation, with the crack parallel to the pipe axis. Experiments were performed in a closed-loop servo-hydraulic machine of 100 kN capacity. The steel specimens were 19.9 mm thick (96 percent of the original pipeline thickness) with no flattening. Specimen geometry, as defined in the ASTM E647-05, and dimensions are depicted in Figure 9.1. A through-thickness notch of 3.2 mm with a V-notch tip was introduced by a sharpened circular

cutting blade. A CMOD (Crack Mouth Opening Displacement) gauge was mounted directly across the notch opening, in the loading line alignment, for monitoring the crack length. The test set-up is shown in the Figure 9.2.

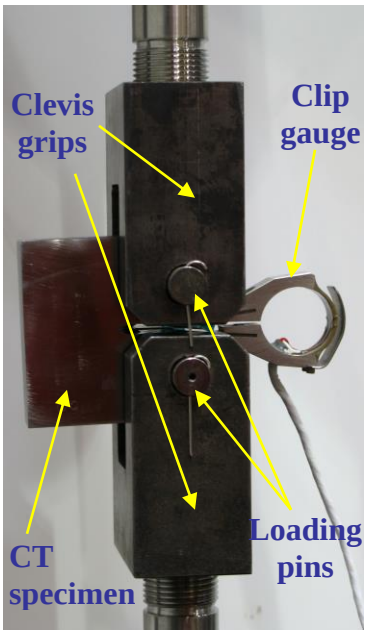

Figure 9.2. Fatigue crack growth rate experimental set-up.

A stepwise increasing ΔK test was used with a normalized K gradient (C) equal to 0.05 or 0.1 (1/mm). The initial ΔK was selected to be 90 MPa·mm$^{1/2}$. To minimize fatigue crack tip damage (due to overload or underload), the initial pre-cracking procedure was performed at a value of ΔK close to the actual testing value. The end test criterion was set to be either a crack growth rate of $5 \cdot 10^{-2}$ mm/cycle or a half crack length of 42 mm (80% of the C(T) specimen width). The specimens were pre-fatigued in air until the last third of the stage II of the fatigue crack growth (corresponding to the end of the stable crack growth) in order to see the effect of hydrogen during the largest crack propagation region. In order to keep the hydrogen from diffusing out of the sample, the C(T) specimens were tinned prior to fatigue testing. Once testing began and new surface is created, hydrogen immediately diffuses out of the specimen at the newly opened crack-tip. In-situ hydrogen fatigue experiments performed under high-pressure gaseous

hydrogen eliminate the effect of hydrogen diffusing out of the specimen with creation of a new crack. The testing parameters are listed in Table 9.1.

Table 9.1. Parameters for the FCGR Test Specimens

Specimen	**Loading ratio, *R***	**ΔK slope (1/mm)**	**Hydrogen charging**	**Tinning**
X100-1	0.1	0.05	No	No
X100-2	0.1	0.05	Yes	Yes
X100-3	0.1	0.1	No	No
X100-4	0.1	0.1	Yes	No
X100-5	0.1	0.1	Yes	Yes
X100-6	0.4	0.1	No	No
X100-7	0.4	0.1	Yes	Yes
X100-8	0.4	0.1	No*	No*
X100-9	0.4	0.1	Yes	Yes

* just submerge in liquid nitrogen (LN_2) before testing.

The fatigue testing has been described, so the next step is designing of the hydrogen sensor coils. The hydrogen sensor coils used for field testing of pipelines will truly aid in the development of the fatigue sensor. The scale of the specimens are similar, however if the hydrogen probe for fatigue testing must be located outside of a hydrogen chamber, then the lift-off would be incredible. The limit of lift-off will be determined. Ideally, the hydrogen sensor probe will be located in the chamber near the specimen. The effects of high pressure hydrogen also need to be characterized because 10,000 to 20,000 psi may have a significant impact on the probes. The low frequency impedance measurements will prospectively be able to provide a three-dimensional hydrogen map.

The fatigue crack growth rate curves for the tests X100-1 and X100-2 are presented in Figure 9.3. The results clearly show an effect of hydrogen on the fatigue crack growth rate. The results also indicate that the hydrogen diffused out of the specimen very quickly because the drastic increase in crack growth rate decreases after the hydrogen diffuses out of the specimen.

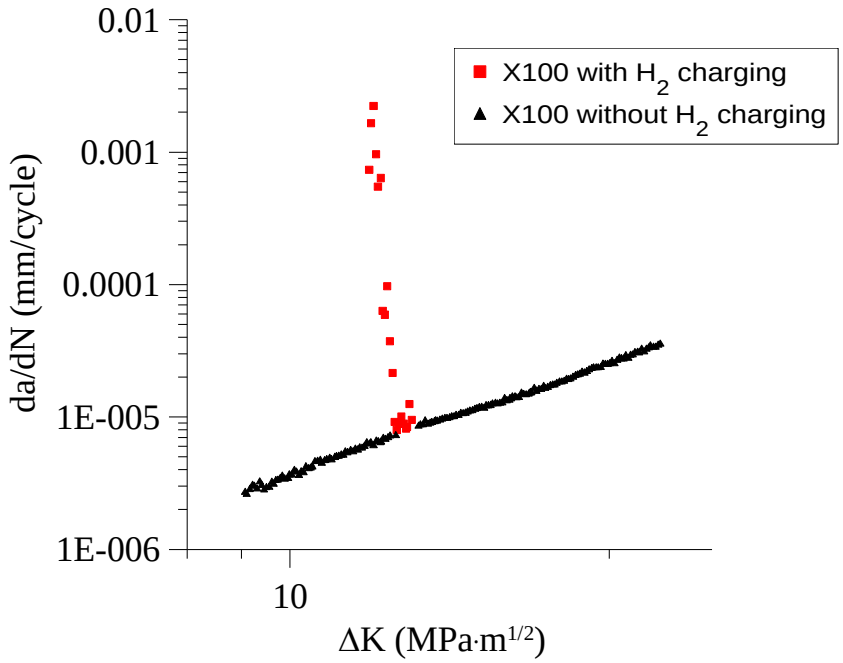

Figure 9.3. Experimental results without hydrogen charging (X100-1) and with hydrogen charging and tinning (X100-2).

The results in Figure 9.3 are important for the development of a low frequency hydrogen sensor during fatigue testing for several reasons. First of all, gaseous hydrogen pre-charging versus in-situ testing will have a much different effect on data because of the amount of hydrogen in the specimen over time. To calibrate the hydrogen sensor using gaseous pre-charged conditions will only be viable to in-situ conditions for the first few seconds of measurements. A secondary calibration of hydrogen as a function of time (from saturation to equilibrium) will be necessary to distinguish between the hydrogen and the fatigue.

In reality, in-situ gaseous hydrogen measurements will be more simplistic because the hydrogen will not continuously be diffusing out of the steel specimen. In-situ gaseous hydrogen measurements will be more stable, however, understanding a pre-charged system will aid in the understanding of any additional or unknown variables. Luckily for pre-charged or in-situ measurements, the coil will remain the same because it is dependent on the size and shape of the specimen. The next step is to attach the new probes near the steel specimen during the fatigue cycles to watch the change in

impedance as a function of time and residual stress. Then once the effect of fatigue on impedance is understood, hydrogen will then be introduced into the specimen.

9.2. Smooth Tensile Specimen Testing

Following completion of the hydrogen test facility, testing will commence on six smooth tensile specimens of X100 pipeline steel for the pipeline working group (PWG) round-robin test program. The round-robin includes Sandia National Laboratories, Oak Ridge National Laboratories, and both NIST in Gaithersburg and Boulder. The test specimens used are 4 mm diameter specimens, tested at room temperature in 2000 psi helium and in 2000 psi hydrogen. The strain rate for all tests is 1×10^{-4} mm/mm/s. All specimens are to be ultrasonically cleaned in isopropanol for 60 seconds, then handled only with gloved hands for transfer to the test chamber. The parameters to be determined from the tests are yield strength, ultimate tensile strength, percent elongation, and reduction of area. Additionally, the gas composition after each test in hydrogen will be measured.

The next set of tests will be on 6 mm diameter smooth tensile specimens, also X100, to determine loading parameters for fatigue testing. These tests will be in air and in pressurized hydrogen gas. Gas pressures of 1000 psi, 3000 psi, and 5000 psi will be used. A similar series of tests will be conducted on X52 smooth tensile specimens. This set will be followed by fatigue testing of X100, using reduced-size C(T) specimens, 44 mm from edge to center of pull, instead of 50 mm. The fatigue crack growth rate will be acquired as a function of ΔK data for these fatigue tests. These will be similarly followed by fatigue tests on X52 steel. Once again, tests will be done in air and in pressurized hydrogen gas at 1000 psi, 3000 psi, and 5000 psi. These measurements are primarily in support of a CRADA with Colorado School of Mines.

The experimental fatigue data generated for X100 will be used in a model to be developed by Professor Rick Gangloff, who will be visiting NIST from the University of Virginia.

CHAPTER 10 THEORETICAL EXPLANATION OF LOW FREQUENCY IMPEDANCE MEASUREMENTS OF HYDROGEN IN LINEPIPE STEEL

This chapter addresses the following theoretical question: Are higher inspection frequencies (and therefore smaller wavelengths) needed for localized hydrogen-induced lattice strain detection in steel?

10.1. Wave propagation regimes

There are three different wave propagation regimes: coherent, diffusive, and near field. Ultrasonic waves retain their coherency over a distance greater than their typical 0.1 to 1.0 mm wavelength. Therefore, ultrasonic waves propagate in the coherent regime where spatial resolution depends on the wavelength. Optical waves lose their coherence during scattering off heterogeneities. The mean free path defines the observation depth and therefore the spatial resolution. These regimes are defined for human tissue wave propagation, however, further treatment will illustrate the role of constitutive material parameters in determining the mode of wave propagation in materials [94].

10.2. Near field regime

Low frequency impedance measurements have been previously explained within a classical electromagnetic induction-based framework [82, 84, 85, 95, 96, 97]. Magnetic induction consists of non-classical evanescent waves are propagated in the near field regime resulting in a bulk measurement resolution is independent of the wavelength of the electromagnetic source. The propagation of these evanescent electromagnetic magnetic waves through an inspected material is analogous to the quantum mechanical tunneling of electrons through a finite potential barrier. The evanescent wave propagation can be thought of as magnetic tunneling.

In low frequency impedance measurements, the sensor acts as an antenna, generating electromagnetic waves that emanate into the surrounding air and inspected material. The boundary between the near and far field regions is determined by the measurement criteria used in addition to the choice between two- and three-region models [98]. In general terms, the near field is the limit in which the observation depth is much smaller

than the wavelength of EM radiation. The wavelength of transverse electromagnetic (TEM) radiation within a good conducting material is given by Equation 10.1 [99].

$$\lambda \approx 2\pi\sqrt{\frac{2}{\omega\mu\sigma}} \tag{10.1}$$

The TEM wavelength in a conductor is therefore approximately a factor of 2π greater than the standard depth of penetration given by Equation 10.2, where α is the attenuation coefficient to be defined later [99]. The standard depth of penetration is the reciprocal of the attenuation coefficient:

$$\delta = \frac{1}{\alpha} \approx \sqrt{\frac{2}{\omega\mu\sigma}}\,. \tag{10.2}$$

Evanescent waves are real exponentially decaying waves with the standard depth of penetration as a scaling factor. For low frequency impedance measurements, this scaling factor is the eddy current standard depth of penetration. The depth resolution of near field low frequency impedance measurements are on the order of the observation depth, which is scaled by the eddy current standard depth of penetration [96, 100]. The pronounced lift-off effect on LFIM is explained by the disruption of near field magnetic induction.

10.3. Eddy Current Phenomenon

The low frequency impedance sensor acts as an antenna, generating transverse electromagnetic waves that are then attenuated in the steel [99]. Traditional eddy current descriptions have the larger picture correct, assuming a sourced magnetic flux induced into the material resulting in a magnetic flux material response due to eddy current formation. The vector addition of the primary (sensor) and secondary (eddy current) magnetic flux densities result in a measured equilibrium flux. However, this macroscopic description does not adequately address the phenomenological and fundamental (both classical and quantum mechanical) divide separating traditional eddy current crack and flaw detection and low frequency impedance assessment of hydrogen content in steel. Lesselier and Razek state that the phenomenon of eddy currents is a byproduct of the interaction of electromagnetic waves with materials. The generated eddy currents, affected by material defects (defined as structural anomalies arising from the manufacture

or wearing of materials), are used to appraise electromagnetic interaction effects due to variation of impedance of the sensing coil. Eddy current phenomena are not often thought of as classical wave scattering phenomena [101]. According to Wilkes and Kittel, the conduction electrons, moving at the Fermi velocity,

$$v_F = \sqrt{\frac{2\varepsilon_F}{m}} = \frac{\hbar}{m}\left(3\pi^2 \frac{N}{V}\right)^{1/3}, \tag{10.3}$$

scatter from "local charge density variations" with a mean free path,

$$\ell = v_F \tau \tag{10.4}$$

defined by Equation 10.4 of approximately 450 Angstroms, where ε_F is the Fermi energy and $\frac{N}{V}$ is the electron concentration [33, 59].

If eddy currents are similar to conduction currents, then their drift velocity defines the net vector average velocity. The Fermi velocity defines the timescale of probability of collisions and therefore defines the spatial resolution of the eddy current phenomenon. The net effect of multitudes of collisions is carried by the vector average defined electrical conductivity of material. The information of all the conduction electron collision events is carried by this slower drift velocity term. Drift and Fermi velocities are analogous to the group and phase velocities of a wave packet. A fundamental explanation of low frequency impedance hydrogen content assessment of pipeline steel follows.

10.4. Maxwell's Equations in Materials

Electromagnetism includes both theoretical and experimental theories from experiments conducted in the 19th century by Ampere, Coulomb, Faraday, Gauss, Lenz, and Volta. Maxwell, a Scottish mathematician and physicist consolidated the separate equations into a consistent group of vector equations known as Maxwell's equations in which the electric and magnetic fields were defined. The differential form of these equations is useful for solving boundary value problems that require boundary conditions and the following assumptions: a) single-valued, b) bounded, c) continuous functions of space and time, and d) continuous spatial and temporal derivatives [99]. The air or pipeline coating gap steel interface define the boundary conditions of LFIM non-contact

hydrogen detection; the integral form of Maxwell's Equations are most convenient for material property discontinuities at the interface.

10.5. Helmholtz Wave Equation and Constitutive Parameters

The Helmholtz wave equation is the scalar wave equation reduction of vector wave equations. For time-harmonic (variations of the form $e^{i\omega t}$), wave Equations 10.5 and 10.6 are defined for complex fields **E** and **H** [99]:

$$\nabla^2\mathbf{E} = i\omega\mu\sigma\mathbf{E} - \omega^2\mu\varepsilon\mathbf{E} = \gamma^2\mathbf{E} \tag{10.5}$$

$$\nabla^2\mathbf{H} = i\omega\mu\sigma\mathbf{H} - \omega^2\mu\varepsilon\mathbf{H} = \gamma^2\mathbf{H}. \tag{10.6}$$

Lossy media is defined as possessing complex constitutive parameters that interact with the time-harmonic oscillations of a transverse electromagnetic mode. The complex parameters turn the wave functions describing the oscillatory TEM nature, creating a real exponentially decaying evanescent wave (the combination of two complex numbers resulting in a negative real exponent). The complex evanescent wave propagation constant, γ, defined by Equations 10.7 and 10.8, consists of a real attenuation constant (α) and an imaginary lossy phase constant, β.

$$\gamma^2 = i\omega\mu\sigma - \omega^2\mu\varepsilon = i\omega\mu(\sigma + i\omega\varepsilon) \tag{10.7}$$

$$\gamma = \alpha + i\beta \tag{10.8}$$

The constitutive relations for time-harmonic electromagnetic fields within a material are given by Equations 10.9, 10.10 and 10.11, where the constitutive parameters act as Green's functions that transform the vector fields **E** and **H** into the electric conduction current density, $\mathbf{J_c}$, the electric flux density, **D**, and the magnetic flux density, **B** [102].

$$\mathbf{J}_c = \sigma\mathbf{E} \tag{10.9}$$

$$\mathbf{D} = \varepsilon\mathbf{E} \tag{10.10}$$

$$\mathbf{B} = \mu\mathbf{H} \tag{10.11}$$

10.6. Magnetic Interactions

Magnetic dipole moments are simply modeled as small current loops with the tangential velocity given by the Fermi velocity. The size of these small current loops in the local magnetic dipole moment model, not the frequency of electromagnetic induction, determines the probing ability of small periodic potential perturbations such as interstitial hydrogen in linepipe steel. The eddy current phenomenon is the material response to evanescent magnetic inductive tunneling. In a metal, the dielectric-determined electric field response is balanced by the funneling and focusing factor known as the magnetic permeability, a constitutive parameter. The magnetic permeability is inversely proportional to the magnetizing inertia. If you view the magnetic dipole moment as being parallel to the face of a domino, then the magnetic permeability is inversely proportional to the time it takes to topple these theoretical dominos resulting in magnetic alignment in the saturation condition. Equation 10.12,

$$\mathbf{m} = -\left(\frac{e}{2m}\right)\mathbf{J}, \tag{10.12}$$

where

$$\left|\mathbf{J}\right| = m\left|\mathbf{r}\times\mathbf{v}\right| = m\omega r^2, \tag{10.13}$$

relates the magnetic dipole moment to the angular momentum (**J**) of the conduction electron creating the magnetic dipole moment. The angular momentum (**J)** is quantized in units of $\hbar$. The generalized expression for Equation 10.12 is given by Equation 10.14,

$$\mathbf{m} = \gamma\mathbf{J} \tag{10.14}$$

where γ is called the magnetomechanical ratio. The magneto mechanical ratio is defined differently for pure electron orbital motion (Equation 10.15) and pure spin (Equation 10.16) [103].

$$\gamma_{orbital} = -\left(\frac{e}{2m}\right) \tag{10.15}$$

$$\gamma_{spin} = -\left(\frac{e}{m}\right) \tag{10.16}$$

The magnetic moment, a vector sum of orbital and spin moments, processes about the angular momentum vector, **J**. The orbital and spin magnetic moment vectors are given by Equations 10.17 and 10.18,

$$\mathbf{m}_{orbital} = \mu_B \{L(L+1)\}^{1/2} \tag{10.17}$$

$$\mathbf{m}_{spin} = 2\mu_B \{S(S+1)\}^{1/2}, \tag{10.18}$$

where μ_B is the Bohr magneton and L and S are the orbital and spin quantum numbers, respectively [96]. The magnetic moment has a time-independent component along the resultant J-vector direction, where $\boldsymbol{J} = \boldsymbol{S} + \boldsymbol{L}$, the resultant vectors for electron spin and orbital moment, respectively. There is also a high frequency, time-dependent component of the magnetic moment that is perpendicular to $\boldsymbol{J}$. The question remains how strong the electron spin-orbital interaction is when an external magnetic field is applied.

10.7. Heisenberg Exchange Interaction Energy

Spontaneous ferromagnetic magnetization proceeds through the alignment of local magnetic moments through exchange interactions between neighbors with the applied magnetic field [51, 99,103].

The dipole-dipole interaction is not greater than $k_B T_C$ and thus cannot overcome thermal disorder to cause magnetic ordering. The answer to the question of how magnetic dipoles align spontaneously is provided through quantum mechanics and the Heisenberg Hamiltonian:

$$\langle H \rangle = -2J_{ex}\mathbf{s}_1 \cdot \mathbf{s}_2, \tag{10.19}$$

where

$$J_{ex} = -K\mathbf{m}_1 \cdot \mathbf{m}_2 \tag{10.20}$$

is the exchange energy and $\mathbf{s}_1$ and $\mathbf{s}_2$ are the spins and $\boldsymbol{\mu}_1$ and $\boldsymbol{\mu}_2$ are the magnetic moments for two neighboring electrons [51, 57, 58]. Positive exchange energy values result in ferromagnetic exchange interactions. Parallel spins lower the electron-electron spin interaction energy at separation distances beyond strong binding in which the Pauli exclusion principle is valid. This intermediate distance is defined by the ratio of interatomic spacing to the incomplete electron inner shell. Bethe's formulation of the exchange energy as a function of the interatomic distances r_{ab} and the radius of the incompletely filled d subshell is given by:

$$J_{ex} = \iint \psi_a^*(r_1)\psi_b^*(r_2)\left[\frac{1}{r_{ab}} - \frac{1}{r_{a2}} - \frac{1}{r_{b1}} + \frac{1}{r_{12}}\right]\psi_a(r_1)\psi_b(r_2)d\tau \qquad (10.21)$$

where r_{12} is the distance between the two electrons and r_{a2} and r_{b1} are the distances between the respective nuclei and electrons [51]. The Bethe-Slater curve shown in Figure 10.1 correctly predicts ferromagnetic behavior for iron, cobalt, and nickel.

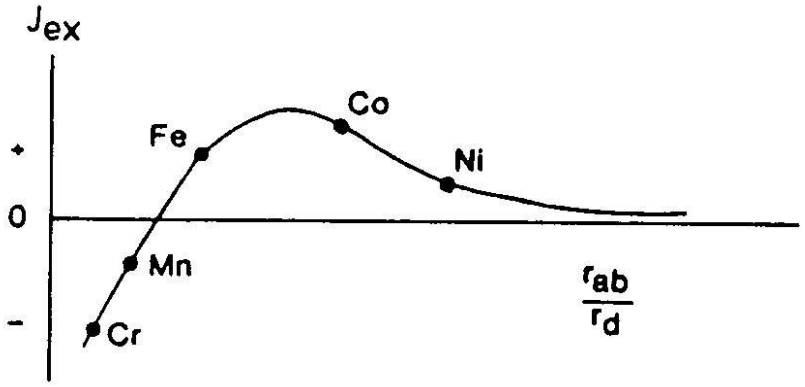

Figure 10.1. Bethe-Slater curve based on Equation 10.21 [51].

Ferromagnetic materials possess the following required electronic structural ingredients for strong exchange interaction energies: a low electron density overlap, a high density of states, and a Fermi energy surface within the *d*-band [33]. Heisenberg applied the exchange coupling between electron spins to ferromagnetism in 1928 [103]. The exchange interaction was postulated to be an essentially electrostatic effect; quantum mechanics and Coulombic electrostatic energy imply that changes in coupled spin states result in changes in their spatial charge distributions.

If different lobes of charge density correspond to different electron states in a free atom, then the Pauli exclusion principle applies to the regions of lobe overlap. Either the electron orbital wave function or the electron spin wave function must be anti-symmetric; if one is anti-symmetric, the other must be symmetric. Therefore, changes in the spin orientation causes changes in the spatial charge distribution via the orbital wave function. The interaction energy, proportional to the scalar dot product of neighboring electron spin vectors, is ascribed to the correlation of electron spins. According to Crangle, a positive

interaction energy parameter leads to a triplet state and magnetic quantum numbers *M* of -1, 0, and +1, resulting in "embryonic molecular ferromagnetism." However, no theory has yet predicted the correct magnitude and sign of the interaction energy parameter to account for ferromagnetism in nickel, cobalt, or iron. It is unclear why *J* should be positive in iron when it has clearly been proven to be negative in the simpler case of the hydrogen molecule [103].

10.8. Exchange Interaction within Electron Bands

The band theory of electrons in metals presents a theoretical wrinkle to interaction energy modeled for local magnetic dipole moments. It is known that partially filled 3d electrons in the conduction band participate in itinerant ferromagnetism [104, 105]. However, attempts to ascribe correlation energy effects for 3d-band electrons provide little insight into the interaction mechanism. One view follows Hund's rules for electron configuration and arrangement and allows for unpaired electrons to have parallel spins resulting in a lowered energy state [103]. There is a small increase in the Fermi energy to setup a magnetic moment; for ferromagnetism Equation 10.22 must hold true:

$$\left(\frac{2}{n}\right)\cdot\Delta E\cdot\nu(E_m)\cdot V>1 \qquad (10.22)$$

where *n* is the excess number of spins in the direction of the magnetization vector ***M***, ΔE is the energy required to reverse the spin of an electron without modifying its wave number at absolute zero, $\nu(E_m)$ is the density of states at the Fermi energy, and *V* is the atomic volume [103]. Interstitial hydrogen in steel affects all of these terms; Fukai's calculation of atomic volume, hydrogen lattice strain affect on the electron effective mass and therefore the density of states, disputed effects of hydrogen on the local magnetic dipole moment affects *n*, and, lastly, the hydrogen interstitial affects the spin orbital wave function and therefore affects ΔE.

10.9. RKKY Theory

Ruderman and Kittel examined nuclear magnetic moments "immersed" in a conduction electron distribution in 1954. Later, Kasuya and Yosida further developed the theory to s-f and s-d electron bad interactions. Collectively, their work is known as the RKKY theory. The RKKY theory is a result of examination of the interaction between

conduction electrons with local magnetic moments associated with periodic Bravais lattice positions. The theory assumes oscillatory, long-range spin polarization of conduction electrons that are not individually localized at local magnetic moment lattice positions. The local magnetic moment, surrounded by conduction electrons, defines a region favorable for conduction electrons with a parallel spin state [103, 106]. Multiple in-phase conduction electron wave functions constructively interfere at the lattice sites, shown in Figure 10.2(a) and (b).

The spin density oscillation period is set by the conduction electrons at the Fermi level. The RKKY theory was worked out for free electrons and an idealized spherical Fermi energy surface. RKKY theory predicts the magnetic coupling, H_{couple}, between atoms a relatively large distance R apart in Equation 10.23 [103]:

$$H_{couple} \propto \left(\frac{1}{R^3}\right) \cdot \cos(2k_F R), \tag{10.23}$$

where k_F is the Fermi momentum.

10.10. Itinerant Magnetism: Conduction Electron Scattering

Most ferromagnetic materials have high value of relative permeability and good electrical conductivity, so there is a minimal interaction with the propagating EM wave. Though the interaction is believed to be heavily magnetic in nature, in ferromagnetism, the conduction electrons are the same spinning electrons that create the local magnetic dipole moments, resulting in what is known as itinerant magnetism [104, 105].

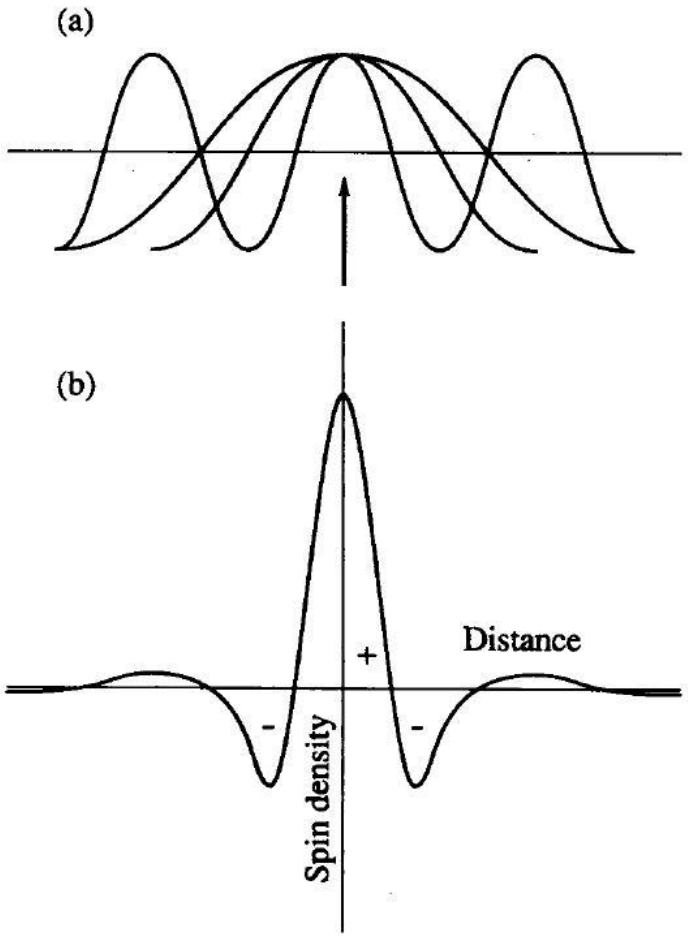

Figure 10.2. Spin density distribution proposed by RKKY theory [103].

CHAPTER 11 SUMMARY OF RESULTS

LFIM are based on the near field regime of wave propagation that reproduces magnetic induction. The observation depth of the near field regime is independent of wavelength. LFIM provide bulk assessment of the inspected material and microstructural defects and lattice strain. To resolve regions of impurities, a sensor array is necessary. However, bulk hydrogen content assessment can be performed with low frequency impedance measurements because the observation depth is independent of wavelength. LFIM are non-contact near field resistivity measurements in which the degree of magnetic inductive coupling is a function of sensor lift-off. Eddy currents generated in the inspected material are the end result of this magnetic near field coupling effect that is monitored by the voltage drop across the sensor. The impedance data collected by Lasseigne, shown in Figure 6.3, exhibits the same linear dependence of Watanabe and Fukai's resistivity measurement data shown in Figure 2.10. Therefore, Lasseigne's hypothesis of the resistivity functionality of hydrogen is validated, confirming the plausibility of previous and current LFIM hydrogen content assessment based on her method of separation of variables that relies on Matthiesson's rule.

The results presented in Chapters 7 and 8 constitute the successful proof of concept and initial calibration efforts for a nondestructive non-contact hydrogen sensor based on low frequency impedance measurements.

CHAPTER 12 CONCLUSIONS

- The experimental results presented constitute a successful proof of concept and initial calibration efforts for a nondestructive, non-contact hydrogen sensor based on low frequency impedance measurements.
- Low frequency impedance measurements monitor changes in the effective mass of the conduction electrons.
- Interstitial hydrogen locally strains the lattice, resulting in Bloch function perturbations that alter the effective mass of the conduction electrons.
- The effective masses of the conduction electrons are sensitive to local magnetic dipole moment fluctuations caused by interstitial hydrogen.
- Itinerant ferromagnetism theory (RKKY) describes localized conduction electron spin density alignment with Bravais lattice positioned local magnetic moments of the iron atoms.
- Near field EM material interactions are independent of wavelength.

REFERENCES CITED

[1] P. F. Timmins, *Solutions to Hydrogen Attack in Steels*. Materials Park, OH: ASM International, 1997, pp. 52, 61.

[2] S. Dey, S. K. Mandhyan, S. K. Sondhi, and I. Chattoraj, "Hydrogen entry into linepipe steel under freely corroding conditions in two corroding media," *Corrosion Science*, vol. 48, pp. 2676-2688, Sep. 2006.

[3] D. Warren, "Hydrogen effects on steel," *Materials Performance*, vol. 26, pp. 38-48, Jan. 1987.

[4] Y. Fukai, *The Metal-Hydrogen System*. Berlin, Germany: Springer-Verlag, 2005, pp. 21-27, 31, 63-68, 105, 108, 112, 118.

[5] Y. Fukai, "Site preference of interstitial hydrogen in metals," *Journal of the Less Common Metals*, vol. 101, pp. 1-16, 1984.

[6] R. B. McLellan and C. G. Harkins, "Hydrogen interactions with metals," *Materials Science and Engineering*, vol. 18, pp. 5-35, 1975.

[7] J. P. Hirth, "Effects of hydrogen on the properties of iron and steel," *Metallurgical Transactions A*, vol. 11A, pp. 861-890, Nov. 1980.

[8] I. Maroef, D. L. Olson, M. Eberhart, and G. R. Edwards, "Hydrogen trapping in ferritic steel weld metal," *International Materials Review*, vol. 47, pp. 191-223, Apr. 2002.

[9] G. M. Pressouyre, "Trap theory of hydrogen embrittlement," *Acta Metallurgica*, vol. 28, pp. 895-911, 1980.

[10] W. Pepperhoff and M. Acet, *Constitution and Magnetism of Iron and Its Alloys*. Berlin, Germany: Springer, 2001, pp. 172-181.

[11] A. I. Shirley and C. K. Hall, "Trapping of hydrogen by substitutional and interstitial impurities in α-iron," *Scripta Metallurgica*, vol. 17, pp. 1003-1008, 1983.

[12] R. A. Oriani, "The diffusion and trapping of hydrogen in steel," *Acta Metall.*, vol. 18, pp. 147-157, 1970.

[13] S. L. I. Chan, "Hydrogen trapping ability of steels with different microstructures," *Journal of the Chinese Institute of Engineers*, vol. 22, pp. 43-53, Jan. 1999.

[14] G. T. Park, S. U. Koh, H. G. Jung, K. Y. Kim, "Effect of microstructure on the hydrogen trapping efficiency and hydrogen induced cracking of linepipe steel," *Corrosion Science*, vol. 50, pp. 1865-1871, 2008.

[15] Y. D. Park, I. S. Maroef, A. Landau, D. L. Olson, "Retained austenite as a hydrogen trap in steel welds," *Welding Journal*, vol. 81, pp. 27s-35s, 2002.

[16] T. Boellinghaus, H. Hoffmeister, and C. Schubert, "Finite element analysis of hydrogen distribution in butt joints," in *Proc 4th Int. Conf. on Trends in Welding Research*, 1995, p. 25.

[17] K. Mundra, J. M. Blackburn, T. DebRoy, "Absorption and transport of hydrogen during gas-metal-arc welding of low alloy steel," *Sci. Tech. Welding Joining*, vol. 2, pp. 174-184, Apr. 1997.

[18] H. H. Johnson, "Hydrogen in iron," *Metallurgical Transactions A*, vol. 19A, pp. 2371-2387, 1988.

[19] O. D. Gonzalez, *Trans. Met. Soc. AIME*, vol. 245, pp. 607-12, 1969.

[20] A. J. Kumnick and H. H. Johnson, "Steady state hydrogen transport through zone refined irons," *Metallurgical Transactions A*, vol. 6A, p.1087, May 1975.

[21] A. J. Kumnick and H. H. Johnson, "Hydrogen and deuterium in iron, 9–73°C," *Acta Metall.*, vol. 25, p.891, Aug. 1977.

[22] N. R. Quick and H. H. Johnson, "Hydrogen and deuterium in iron, 49–506°C," *Acta Metall*., vol. 26, p. 903, June 1978.

[23] H. G. Nelson and J. E. Stein, NASA Ames Research Center, Moffett Field, CA, NASA Report TND-7265, 1973.

[24] K. Ichitani and M. Kanno "Visualization of hydrogen diffusion in steels by high sensitivity hydrogen microprint technique," *Science and Technology of Advanced Materials*, vol. 4, pp. 545-551, 2003.

[25] W.C. Luu, J.K. Wu, "The influence of microstructure on hydrogen transport in carbon steels," *Corrosion Science*, vol. 38, pp. 239–245, 1996.

[26] F. J. Sánchez, B. Mishra and D. L. Olson, "Magnetization effect on hydrogen absorption in high-strength steels and its implications," *Scripta Materialia*, vol. 53, pp. 1443-1448, 2005.

[27] J. E. Jackson, "Magnetic field effects on magnetocorrosion in linepipe steel," M.S. Thesis, Colorado School of Mines, Golden, CO, 2009.

[28] A. S. Tetelman, C. N. J. Wagner, and W. D. Roberston, “An x-ray investigation of the effects of hydrogen in iron,” *Acta Metallurgica*, vol. 9, pp. 205-215, 1961.

[29] W. Hume-Rothery, *The Structure of Alloys of Iron: An Elementary Introduction*. London, England: Pergamon, 1966, p. 163.

[30] A. Głowacka and W. A. Świątnicki, “Effect of hydrogen charging on the microstructure of duplex stainless steel,” *Journal of Alloys and Compounds*, vol. 356–357, pp. 701–704, 2003.

[31] H. Peisl, “Lattice strains due to hydrogen in metals,” in *Hydrogen in Metals I*, vol. 28, J. Völkl and G. Alefeld, Eds., New York: Springer-Verlag, 1978, pp. 53-74.

[32] V. G. Gavriljuk, V. N. Shivanyuk, and B. D. Shanina, “Change in the electronic structure caused by C, N, and H atoms in iron and its effect on their interaction with dislocations,” *Acta Materialia*, vol. 53, pp. 5017-5024, 2005.

[33] P. Wilkes, *Solid State Theory in Metallurgy*. Cambridge: Cambridge University Press, 1973, pp. 118-132.

[34] A. C. Switendick, “The change in electronic properties on hydrogen alloying and hydride formation,” in *Hydrogen in Metals I*, vol. 28, J. Völkl and G. Alefeld, Eds., New York: Springer-Verlag, 1978, pp. 101-129.

[35] C. D. Gelatt, “The metal-hydrogen bond,” in *Theory of Alloy Phase Formation*, Warrendale, PA: TMS/AIME, 1980, p. 455.

[36] S. Moriya, S. Takaki, and H. Kimura, “Resistivity recovery at low temperatures in iron charged with hydrogen,” *Scripta Metallurgica*, vol. 8, pp. 937-939, 1974.

[37] K. Watanabe and Y. Fukai, “Electrical resistivity due to interstitial hydrogen and deuterium in V, Nb, Ta and Pd,” *J. Phys. F: Metal Phys.*, vol. 10, pp. 1795-1801, 1980.

[38] K. Yamakawa, M. Tada, and F. E. Fujita, “Recovery of pure iron quenched in the liquid hydrogen,” *Scripta Metallurgica*, vol. 9, pp. 1-4, 1975.

[39] S. A. Gedeon and T. W. Eagar, “Thermochemical analysis of hydrogen absorption in welding,” *Welding Journal*, vol. 69, pp. 264s-271s, 1990.

[40] T. Terasaki, T. Akiyama, S. Hamashima, and K. Kishikawa, “An analysis on specimen size for determination of diffusible hydrogen content in weld metal,” *Trans. Japan Welding Society*, vol. 17, pp. 93-101, 1986.

[41] R. D. Smith, II, “Methods for the determination of hydrogen distribution in high strength steel,” Ph.D. Thesis, Colorado School of Mines, Golden, CO, 1999.

[42] B. A. B. Andersson, “Diffusion and trapping of hydrogen in a bead-on-plate weld,” *Journal of Engineering Materials and Technology*, vol. 102, pp. 64-72, 1980.

[43] N. Yurioka and H. Suzuki, “Hydrogen assisted cracking in C-Mn and low alloy steel weldments,” *International Materials Review*, vol. 35, p. 226, Apr. 1990.

[44] V. D. Tarlinski, et al., “Distribution of hydrogen during the manual arc welding of increased strength tube steels,” *Avtom. Svarka*, vol. 27, pp. 16-20, 1974.

[45] L. Tomlinson and N. J. Cory, “Hydrogen emission during the steam oxidation of ferritic steels: Kinetics and mechanism,” *Corrosion Science*, vol. 29, pp. 939-965, 1989.

[46] H. Barlag, L. Opara, and H. Züchne, “Hydrogen diffusion in palladium based f.c.c. alloys,” *Journal of Alloys and Compounds*, vol. 330-332, pp. 434-437, Jan. 2002.

[47] ASTM International, “Standard practice for evaluation of hydrogen uptake, permeation, and transport in metals by an electrochemical technique,” ASTM Standard G148 - 97(2003), 2003.

[48] NACE International, “Laboratory testing of metals for resistance to sulfide stress cracking and stress corrosion cracking in H_2S environments,” NACE STD TM0177-2005, 2005.

[49] S. H. Khan, F. Ali, F., A. N. Khan, M. A. Iqbal, “Pearlite determination in plain carbon steel by eddy current method,” *Journal of Materials Processing Technology*, vol. 200, pp. 316-318, 2008.

[50] J. B. Nestleroth, and R. J. Davis, “Application of eddy currents induced by permanent magnets for linepipe inspection,” *NDT&E International*, vol. 40, pp. 77-84, 2007.

[51] D. Jiles, *Introduction to Magnetism and Magnetic Materials*. London: Chapman & Hall, 1991, pp. 69-120, 252-255, 262-265.

[52] D. Lihong, X. Binshi, D. Shiyun, C. Qunzhi, and W. Dan, “Variation of stress-induced magnetic signals during tensile testing of ferromagnetic steels,” *NDT&E International*, vol. 41, pp. 184-189, 2008.

[53] T. Yamasaki, S. Yamamoto, and M. Hirao, “Effect of applied stresses on magnetostriction of low carbon steel,” *NDT&E International*, vol. 29, pp. 263-268, 1996.

[54] R. M. Bozorth, *Ferromagnetism*. New York, NY: Van Nostrand, 1951, pp. 1-15, 476-482.

[55] S. Chikazumi, *Physics of Ferromagnetism*. Oxford, England: Clarendon Press, 1997, p. 417.

[56] W. J. Carr, Jr., "Principles of Ferromagnetic Behavior," in *Magnetism and Metallurgy*, vol. 1, A. E. Berkowitz and E. Kneller, Eds. New York: Academic Press, 1969, pp. 45-92.

[57] R. H. Bube, *Electrons in Solids: An Introductory Survey*. 3rd ed., San Diego, CA: Academic Press, 1992, pp. 249, 251, 259.

[58] B. K. Tanner, *Introduction to the Physics of Electrons in Solids*. Cambridge: Cambridge University Press, 1995, pp. 181-212.

[59] C. Kittel, *Introduction to Solid State Physics*. Hoboken, NJ: John Wiley & Sons, Inc, 2005, p.350.

[60] D. L. Atherton and D. C. Jiles, "Effects of stress on magnetization," *NDT International*, vol. 19, pp. 15-19, 1986.

[61] M. J. Sablik and B. Augustyniak, "The effect of mechanical stress on a Barkhausen noise signal integrated across a cycle of ramped magnetic field," *J. Appl. Phys.*, vol. 79, pp. 963-972, 1996.

[62] M. J. Sablik, "Modeling the effect of grain size and dislocation density on hysteretic magnetic properties in steels," *J. Appl. Phys.*, vol. 89, pp. 5610-5613, 2001.

[63] K. Gruska, "Use of harmonic analysis for inspection of ferromagnetic materials," *Soviet Journal NDT,* vol. 19, pp. 399-409, 1983.

[64] M. N. Mikheev and E. S. Gorkunov, "Relationship of magnetic properties to the structural condition of a substance-The physical basis of magnetic structure analysis (Review)," *Soviet Journal NDT*, vol. 17, pp. 579-592, 1981.

[65] H. Kwun and G. L. Burkhardt, "Effects of grain size, hardness, and stress on the magnetic hysteresis loops of ferromagnetic steels," *J. Appl. Phys.*, vol. 61, pp. 1576-1579, 1987.

[66] H. Kwun, and G. L. Burkhardt, "Nondestructive measurement of stress in ferromagnetic steels using harmonic analysis of induced voltage," *NDT International,* vol. 20, pp. 167-171, 1987.

[67] M. M. Shel, “Measurement of stress in hard-magnetic steels by means of the magnetoelastic method,” *Industrial Lab*, vol. 33 p. 361, 1967.

[68] N. Dube, M. Fiset, and A. Galibois, “Magnetic effect on the hydrogen entry in iron detected by Rayleigh wave attenuation,” *Scripta Metallurgica*, vol. 20, pp. 1669-1670, 1986.

[69] V. S. Agarwala, and J. J. DeLuccia, “Effects of a magnetic field on hydrogen evolution reaction and its diffusion in iron and steel,” Naval Air Development Center Report: NADC-81029-60, 1981.

[70] M. E. Elzain and A. A. Yousif, “Local magnetic moment and hyperfine field in hydrogenated iron and iron-vanadium alloy,” *Hyperfine Interactions*, vol. 94, pp. 1879-1884, 1994.

[71] E. S. Gorkunov, S. M. Zadvorkin, I. N. Veselov, D. I. Vichuzhanin, and S. Y. Mitropolskaya, “The effect of hydrogen sulphide on the magnetic behaviour of tube steel X42SS in uniaxial tension,” presented at the 17th World Conference on Nondestructive Testing, Shanghai, China, 2008.

[72] K. Peng, A. Hu, D. Wang, J. Tang, and Y. Du, “Influence of hydrogen on the magnetic properties of Fe85Zr3.5Nb3.5B7Cu1 nanocrystalline alloy,” *Materials Chemistry and Physics*, vol. 91, pp. 289-292, 2005.

[73] K. Kandasamy, M. Masuda, and Y. Hayashi, “Hydrogen-induced changes of the magnetic properties of copper-cobalt multilayers,” *Journal of Alloys and Compounds*, vol. 282, pp. 23-31, 1983.

[74] H. Kronmüller, “Magnetic aftereffects of hydrogen isotopes in ferromagnetic metals and alloys,” *Hydrogen in Metals I*, vol. 28, J. Völkl and G. Alefeld, Eds., New York: Springer-Verlag, 1978, pp. 289-320.

[75] M. A. Quintana, P. Cote, and L. G. Kvidahl, “Hydrogen measurement techniques,” in *Hydrogen Management for Welding Applications*, J. E. M. Braid, C. V. Hyatt, D. L. Olson, and G. N. Vigilante, Eds., Ottawa, Canada: CANMET, 1999, pp. 155-169.

[76] American Welding Society, “Standard methods for determination of diffusible hydrogen content of martensitic, bainitic, and ferritic steel weld metal produced by arc welding,” AWS STD A4.3-93, 1993.

[77] R. D. Smith II, G. P. Landis, I. Maroef, D. L. Olson, and T. R. Wildeman, “The determination of hydrogen distribution in high strength steel weldments part 1: Laser ablation methods,” *Welding Journal*, vol. 80, pp. 115s-121s, May 2001.

[78] R. D. Smith, D. K. Benson, I. Maroef, D. L. Olson, and T. R. Wildeman, "The determination of hydrogen distribution in high-strength steel weldments part 2: Opto-electronic diffusible hydrogen sensor," *Welding Journal*, vol. 80, pp. 122s-126s, July 2001.

[79] K. Ebihara, T. Suzudo, H. Kaburaki, K. Takai, and S. Takebayashi, "Modeling of hydrogen thermal desorption profile of pure iron and eutectoid steel," *ISIJ International*, vol. 47, pp. 1131-1140, 2007.

[80] M. Enomoto, D. Hirakami, and T. Tarui, "Modeling thermal desorption analysis of hydrogen in steel," *ISIJ International*, vol. 46, pp. 1381-1387, 2006.

[81] Y. D. Park, A. N. Lasseigne, V. I. Kaydanov, and D. L. Olson, "Thermoelectric diagnostics for non-destructive evaluation of materials," in *10th CF/DRDC Meeting on Naval Applications of Materials Technology*, 2003, pp. 648-666.

[82] A.N. Lasseigne, "Development of thermoelectric power and electromagnetic techniques for determination of interstitials in advanced materials," Ph.D. Thesis, Colorado School of Mines, Golden, CO, 2006.

[83] M. P. Perry, *Low Frequency Electromagnetic Design*, New York: Marcel Dekker, 1985.

[84] K. Koenig, J. W. Cisler, A. N. Lasseigne, R. H. King, B. Mishra, and D. L. Olson, "Nondestructive, Non-contact Hydrogen Content Assessment of Coated Steel Linepipe Welds", in *Review of Progress in QNDE*, **29**, edited by D. O. Thompson and D. E. Chimenti, AIP Conference Proceedings, American Institute of Physics, Melville, NY, pp. 1167-1174, 2010.

[85] K. Koenig, A.N. Lasseigne, J.W. Cisler, B. Mishra, and D.L. Olson, "Non-Contact Non-Destructive Hydrogen and Microstructural Assessment of Steel Welds," in *International Conference WELDS 2009*, Ft. Myers, Florida, EPRI, Charlotte, NC (In press).

[86] T. Yamaoka, S. M. Stepanyuk, S. Matsuoka, "The effect of residual hydrogen on high-cycle fatigue property of welded joints for gas linepipe steel," in *Effects of Hydrogen on Materials: Proceedings of the 2008 International Hydrogen Conference*, Jackson Lake Lodge, Wyoming, Materials Park: ASM International, pp. 373-380, 2009.

[87] H. J. Cialone and J. H. Holbrook, "Sensitivity of Steels to Degradation in Gaseous Hydrogen," in *Hydrogen Embrittlement: Prevention and Control*, ASTM STP 962, ed. L. Raymond, American Society for Testing and Materials, Philadelphia, pp. 134-152, 1988.

[88] R. Zawierucha and K. Xu, "Hydrogen Pipeline Steels," in *Materials for Hydrogen*

Economy Symposium, Materials Science and Technology 2005 Conference and Exhibition, pp. 79-90, 2005.

[89] R. J. Walter and W. T. Chandler, "Cyclic-load Crack Growth in ASME SA-105 Grade II Steel in High Pressure Hydrogen at Ambient Temperature," in *Effect of Hydrogen on Behavior of Materials*, ed. A. W. Thompson and I. M. Bernstein, The Metallurgical Society of American Institute of Mining, Metallurgical, and Petroleum Engineers (AIME), Inc., New York, NY, pp. 273-286, 1976.

[90] P. J. Cotterill and J. E. King, "Hydrogen embrittlement contributions to fatigue crack growth in a structural steel," *International Journal of Fatigue*, vol. 13, no. 6, pp. 447-452, 1991.

[91] P. J. Cotterill and J. E. King, "The influence of a coal gasifier atmosphere on fatigue crack growth rates in BS 4360 steel," *International Journal of Fatigue*, vol. 15, no. 1, pp. 27-30, 1993.

[92] J. D. Frandsen and H. L. Marcus, "Environmentally assisted fatigue crack propagation in steel," *Metallurgical Transactions A: Physical Metallurgy and Materials Science*, vol. 8A, no. 2, pp. 265-272, 1977.

[93] S. C. Mittal, R. C. Prasad, and M. B. Deshmukh, "Effect of hydrogen on fatigue crack growth in austenitic Fe-Mn-Al steel," *Transactions of The Indian Institute of Metals*, vol. 49, no. 3, pp. 185-196, June 1996.

[94] M. Fink and M. Tanter, "Multiwave imaging and super resolution," *Physics Today*, pp. 28-33, 2010.

[95] A. N. Lasseigne, K. Koenig, J. D. McColskey, J. E. Jackson, D. L. Olson, B. Mishra, and R. H. King, "Advanced Non-Contact Diffusible Hydrogen Sensors for Steel Weldments," in *Trends in Welding Research: Proceedings of the 8th International Conference*, edited by S. A. David, T. DebRoy, J. N. DuPont, T. Koseki, H. B. Smartt, Pine Mountain, Georgia, ASM International, Materials Park, OH (2009), pp. 424-429.

[96] A.N. Lasseigne, K. Koenig, D.L. Olson, J.E. Jackson and B. Mishra, " Real-Time Low Frequency Impedance Measurements for Determination of Hydrogen content in Linepipe Steel," in *Review of Progress in QNDE*, **28B**, edited by D. O. Thompson and D. E. Chimenti, AIP Conference Proceedings vol. 1092, American Institute of Physics, Melville, NY (2009), pp. 1283-1290.

[97] A.N. Lasseigne, K. Koenig, J.D. McColskey, T.A. Siewert, J.E. Jackson, D.L. Olson, B. Mishra, "Non-Destructive Determination of the Diffusion Coefficient of Hydrogen in Steel," in *Effects of Hydrogen on Materials: Proceedings of the 2008 International Hydrogen Conference*, Jackson Lake Lodge, Wyoming, ASM International, Materials Park, OH (2009), pp. 524-531.

[98] C. Capps, “Near field or far field?” *EDN*, pp. 95-102, 2001.

[99] C. A. Balanis, *Advanced Engineering Electromagnetics*, New York: John Wiley & Sons, 1989.

[100] D. E. Bray and R. K. Stanley, *Nondestructive Evaluation: A Tool in Design, Manufacturing, and Service*, Boca Raton, FL: CRC Press, 1997.

[101] D. Lesselier and A. Razek, “Eddy-current scattering: Green’s integral and variational formulations,” *Scattering : scattering and inverse scattering in pure and applied science, R. Pike and P. Sabatier, eds., vol. 1*, pp. 486-507, 2002.

[102] Interview with Dr. Gary Olhoeft, Colorado School of Mines, Golden, CO, March 2010.

[103] J. Crangle, *Solid State Magnetism*, New York: Van Nostrand Reinhold, 1991.

[104] W. Zwerger, “Itinerant ferromagnetism with ultracold atoms,” *Science*, vol. 325, no. 5947, pp. 1507-1509, 2009.

[105] G-B Jo, Y-R Lee, J-H Choi, C. A. Christensen, T. H. Kim, J. H. Thywissen, D. E. Pritchard, and W. Ketterle, “Itinerant ferromagnetism in a Fermi gas of ultracold atoms,” *Science*, vol. 325, no. 5947, pp. 1521-1524, 2009.

[106] P. Bruno and C. Chappert, “Interlayer Exchange Coupling: RKKY Theory and Beyond,” in *Magnetism and Structure in Systems of Reduced Dimension*, R. F. C. Farrow, B. Dieny, M. Donath, A. Fert, B.D. Hermsmeier, Eds., pp. 389-399, 1993.